Asymmetric Splitting of Bose-Einstein Condensate

A Dissertation

Presented to

the faculty of the School of Engineering and Applied Science

University of Virginia

---

in partial fulfillment

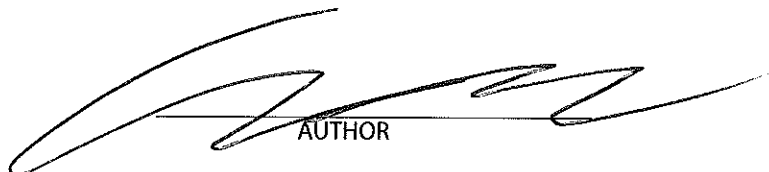of the requirements for the degree

Doctor of Philosophy

by

Eun Oh

December

2014

APPROVAL SHEET

The dissertation

is submitted in partial fulfillment of the requirements

for the degree of

Doctor of Philosophy

AUTHOR

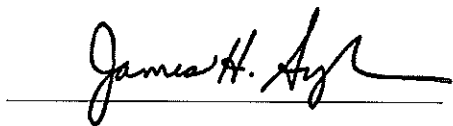The dissertation has been read and approved by the examining committee:

Charles Sackett

_____
Advisor

William Soffa, Chair

_____

Thomas Gallagher

_____

Petra Reinke

_____

Mool Gupta

_____

_____

Accepted for the School of Engineering and Applied Science:

_____
Dean, School of Engineering and Applied Science

December
2014

Acknowledgements

Abstract

We describe a novel atom interferometry technique for manipulating Bose-Einstein Condensate. The technique requires a Bose-Einstein condensate, which will be manipulated using pulsed, off-resonant laser beams. The new technique permits a larger interferometer arm separation and longer separation times compared to previous experiments, thus providing greater sensitivity to gravity. To achieve such feat we need the pulsed beams' phase stabilized via an electro-optical active feedback system. Such apparatus is built and demonstrated to manipulate ultra cold atoms with precision. We present interferometry measurements to accurately ascertain the recoil velocity of the ^{87}Rb atoms to less than 1% of the theoretical value. This work lays the foundation for the next generation gravity measurement improving the sensitivity over the current existing instruments.

Contents

1

Introduction

Introduction and Motivation Behind Atom Interferometry

Many devices have been available throughout history to measure quantities such as time, distance, weight, acceleration, temperature, speed of light, and gravity. Whether it is a very accurate meter stick, a precise weight scale, or a reliable atomic clock, the pursuit of perfection drives scientists to measure these quantities more accurately than their predecessors. The greater purpose behind measuring these quantities accurately is to understand of the workings of the universe; many of the fundamental constants, the laws of physics, and even the origin of the universe owes its understanding to measuring these quantities accurately. In the modern era, one of the best techniques for making such measurement accurately is an interferometer. An optical interferometer is a device

which makes use of the principle of superposition in electromagnetic waves such that the wave is split, traveling two different paths, and then recombined to show constructive or destructive interference output determined by the path and/or refractive index difference relative to each other. Laser based optical interferometers have been in existence for many decades and is used in fields such as astronomy, geology, oceanography, spectroscopy, radar, gyroscopes, and rotational sensors.

With the recent advancement in ultra-cold atom science with Bose-Einstein condensates (BEC), we are now exploring interferometers based on atoms as a coherent source. The ultra-cold atoms also possess wave functions which behave much like that of the electromagnetic waves exhibiting the principles of superposition for building an atom based interferometer. We can also split, reflect, and recombine atom waves just like laser beams in a similar "style and fashion" but with an alternative methodology. The resulting output is also a combination of constructive and destructive interference output. Hence we can build an interferometer based on ultra-cold atoms as a source and be able to measure external quantities that may have been difficult to measure with laser interferometer such as gravity. As we shall see in the next few sections, such devices promise a greater sensitivity over the laser interferometers. In this introduction we explore both types of interferometers - laser and atom based interferometers, and describe how an atom interferometer can be built to measure gravity with more precision than the current existing gravimeters.

This thesis is divided into following chapters: 1) Introduction, 2) Theoretical Considerations, 3) Instrumentation, 4) Bose-Einstein Condensate, 5) Asymmetric Splitting, 6) Asymmetric Interferometer, and 7) Conclusion. Our aim here is to

demonstrate a feasibility of our newly proposed way to measure gravity through an asymmetric splitting of Bose-Einstein condensate. Such device, if successful, allows BEC trajectories of increasing vertical separation, which improves the sensitivity of gravity measurement with greater accuracy which is not possible to achieve with a conventional symmetric atom interferometer. We approach such endeavor theoretically and experimentally and present our preliminary results.

1.1 History of Interferometer – Laser vs. Atoms

In 1665, an Italian Jesuit priest, Francesco Grimaldi, observed diffraction fringes produced by a narrow slit and concluded that light is consisted of a very fine fluid in a state of constant vibration. Although the pre-mature assumption was inaccurate, it started the beginning of understanding of light. In 1678, the Dutch scientist Christiaan Huygens formulated the wave propagation theory, suggesting that the spherical waves propagate along the wave front. A booked published by Sir Isaac Newton in 1704 called *Optiks*, encompassed understanding of behavior of light with the concepts of refraction, dispersion, diffraction, and discovery of spectrum. It was not until 1802 that Thomas Young performed his double slit experiment and found that light propagates in a wave form and be able to interfere with itself. Young contributed two of the most fundamental principles in the field of interferometry: the Principles of Coherence and Principle of Superposition. From the white light double split experiment to the invention of lasers in 1960 by Charles Townes, a tremendous amount of progress in the field of optics allowed scientists build a scientific instrument such as an optical interferometer.

A simple concept of an optical interferometer is shown in Fig. 1.1. A coherent electromagnetic wave such as laser beam enters from the left and is split, travel two different paths, deflected by mirrors to change direction, and then re-combined. In the case when one path of the interferometer experiences a length change or an index of refraction change compared to the other path, the wave traveling through that region will experience a phase shift. This effect in one path will change the relative phase between the two waves when recombined, changing the interference output. Like that of Young's double slit experiment, interference output is result of constructive and destructive effects of superposition of electromagnetic wave [1].
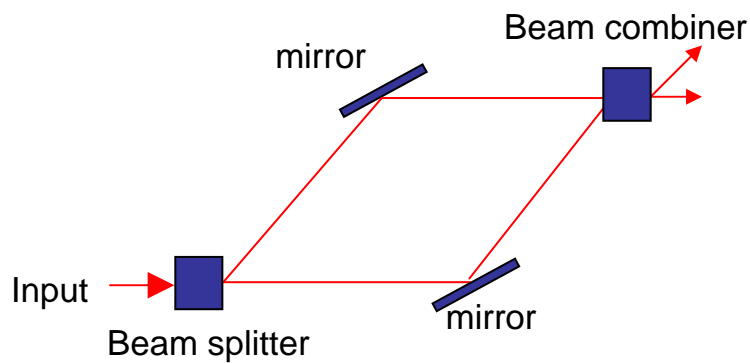
Figure 1.1 Conceptual drawing shows a simple interferometer where interference pattern is obtained when the electromagnetic wave such as laser beam is split, enclosing an area or traveling two different paths through a beam splitter and mirrors. Output interference is measured using a photo detector.

The resulting interference signal is measured by a photodetector as a measurable intensity. By measuring interference, we can learn about environment of path so that we can determine the types of effects and what was causing the electromagnetic wave in that particular path to shift phase. This is the basics of interferometer. It is a device that can quantify the effect in one of the arms' path by measuring the interference output. Such a technique is well established and already crystallized in the scientific history which

includes famous Young's double slit experiment, Michelson interferometer, Mach-Zender, and Fabry-Perot interferometers [2, 3]. Their uses in the modern era encompass astronomy, metrology, quantum mechanics, spectroscopy, and geology. Furthermore, there are plethora of industrial and military applications.

However, an interferometer is not only limited to electromagnetic waves from laser beams. We know from physics that the atom also has an equivalent matter-wave wavefunction and behave much like electromagnetic waves. Hence, if we use atom's wavefunction as the source of an interferometer, we can also construct an interferometer based on the atoms. The atom wavefunction exhibits constructive and destructive interference just like electromagnetic waves. More specifically, quantum mechanics states that the wavefunction of an atom is derived from the Schrodinger's equation as,

$$i\hbar\frac{d\psi}{dt} = H\psi .$$

(1.1.1)

We also assume an eigenstate exist for the condition,

$$H\psi = E\psi .$$

(1.1.2)

The solution to Schrodinger's equation is a simple mathematical solution, yielding,

$$\psi(\vec{r},t) = \psi_0 e^{-\frac{iE}{\hbar}t}$$

(1.1.3)

where ψ_0 is an amplitude, E is the energy of atom, t is time, and $\hbar$ is the Plank's constant divided by 2π. The atom wavefunction phase is given by the Bohr phase,

$$\phi_{Bohr} = \frac{Et}{\hbar} .$$

(1.1.4)

To illustrate the interference of two atom wavefunctions in an atom interferometer, specifically writing out the wavefunctions of the two paths,

$$\psi_1 = \psi_1 e^{-i\phi_1} \tag{1.1.5}$$

$$\psi_2 = \psi_2 e^{-i\phi_2} \tag{1.1.6}$$

where phases $\phi_1 = \dfrac{E_1}{\hbar}t$ and $\phi_2 = \dfrac{E_2}{\hbar}t$ and E_1 and E_2 are the energies of atoms associated with the wavefunctions ψ_1 and ψ_2 respectively. The total wavefunction is

$$\psi_{total} = \psi_1 + \psi_2 = \psi_1 e^{-i\phi_1} + \psi_2 e^{-i\phi_2} \tag{1.1.7}$$

and the resulting intensity when recombined is,

$$I = \left|\psi_{total}\right|^2 = \psi_{total} \cdot \psi_{total}^* = \left|\psi_1\right|^2 + \left|\psi_2\right|^2 + 2\psi_1 \cdot \psi_2 \cos^2(\Delta\phi) \tag{1.1.8}$$

where the phase $\Delta\phi = \dfrac{E_2 - E_1}{\hbar}t$. Equation (1.1.8) is a mathematical representation of the resulting interference intensity output and clearly shows that the interference signal varies as $\cos^2(\Delta\phi)$. Therefore, when the atom wavefunctions recombine, such an energy difference shows up as intensity variation in the interference output. The output intensity is basically a probability of the atom to be in a specific state in quantum mechanics. Such a quantity is observable using a conventional photodetector. Hence there is no need for a special quantum mechanical "atom detector" to observe the interference.

As a specific example, consider the measurement of gravity. Heuristically speaking, gravity can be measured with an atom interferometer by measuring the energy difference between two different vertical paths that the atoms traveled at different heights. The energy difference of the atoms traveling at different heights z_1 and z_2 is proportional to

$$\Delta E = mg\Delta z \tag{1.1.9}$$

where $\Delta z = z_2 - z_1$. Therefore a change in the energy changes the Bohr phase of the wavefunction and according to equation (1.1.8) an interference output is observed. Although the wavefunction is complex and cannot be observed, its probability - square of the wavefunction - is measurable.

To illustrate such concept, a hypothetical atom interferometer, as shown in Fig. 1.2, is similar to the laser interferometer previously mentioned. In this new atom interferometer, the atom packet from the left enters the "atom splitter" and splits into two distinct packets. One-half of the original atom packet is sent upward, while the other
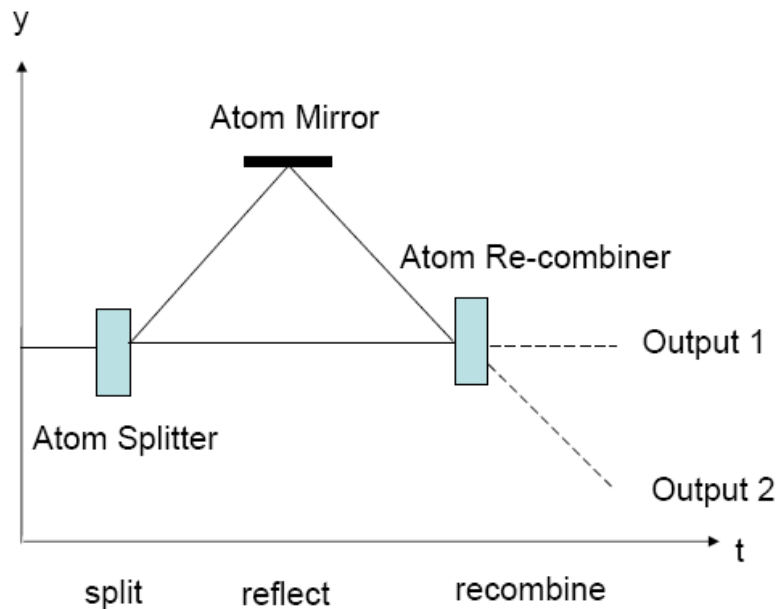
Figure 1.2   A simple concept of atom interferometer where it can split, reflect, and recombine to make atom interferometer.

one-half remains at the same height. After the top packet travels some height against gravity, the "atom mirror" reflects the top atom packet to travel in the opposite direction. A certain time later, an "atom re-combiner" is used to combine the two packets together. Following the basics of an interferometer, the top packet just experienced a different gravitational energy than the one that remained at the same height. The resulting

superposition of the two wavefunctions will show interference based on the energy difference, i.e. the height difference $z_2 - z_1$, between the two wavefunctions. The interference output is analogous to the light interferometer output where interference signal reveals any relative phase difference obtained by the two paths. We will go over detailed derivation of such an atom interferometer later in the thesis.

For the past two decades, before ultra-cold atoms became available to the scientific community, there had been a significant progress on gravity measurements using the thermal atom interferometry. A thermal atom interferometer uses a conventional gas, as opposed to a Bose-Einstein condensate. The relation between the two is similar to the difference between white light and a laser. The lower coherence of a thermal atom source restricts the operation of an interferometer to certain "white light" configurations, where the interferometer phase is independent of the atomic velocity. A few known gravity measurement using thermal atom interferometers have configurations such as dropping the atoms in a free fall and measuring its time to fall a known distance accurately, or in a fountain geometry where the atoms are launched up and then let it come down eventually due to gravity. In an interferometer of such configuration, the exact phase of a wavefunction can be calculated with an action function S(t) by

$$\phi = \int \frac{S(t)}{\hbar} dt . \qquad (1.1.4)$$

To gain significant phase to measure gravity, a thermal interferometer would require integration over longer times which directly translate into longer drop distances ($d \sim t^2$). Hence, measuring gravity with thermal atoms intrinsically requires taller and bigger systems. Furthermore, we will soon learn that the sensitivity goes as the inverse distance and time - a long-distance drop and long-times are needed for a high sensitivity

8

measurements, corroborating the requirement for a longer and bigger apparatus. Nevertheless, the technique has surpassed the conventional mechanical gravimeter [1].
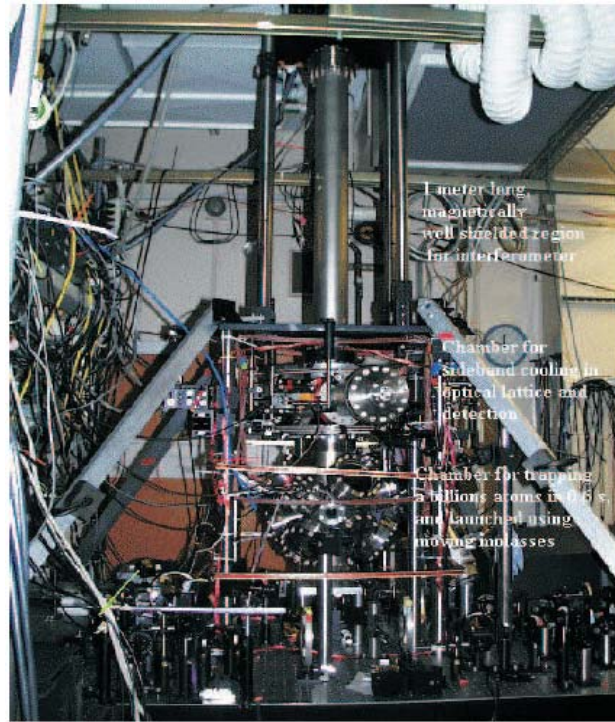
Figure 1.3 Typical thermal atom gravity sensing apparatus. Notice the vertical length atoms has to travel to make the measurement. [5]

Recently, atom interferometry with the Bose-Einstein condensate (BEC) promises similar sensitivity as thermal atom interferometry, but with the possibility to avoid large drop distances. Our scheme is not to drop BEC a longer distance but suspend the atom packets against gravity via repeated laser pulses so that the BEC does not drop significantly, but at the same time be able to separate a large packet displacement (~ cm) to attain a sensitivity that can exceed the current thermal interferometers. There are several reasons for using the BEC over the thermal atoms for such configuration.

First, the BECs are formed in a single potential in a same quantum state which is equivalent to a laser whose photons are all in the same coherent state. However, the

thermal atoms have a wide velocity spread, which has multiple states, making them equivalent to a beam of white light. Therefore, the BEC intrinsically has a longer coherence length over thermal atom, analogous to the longer coherence length of laser beam compared to that of white light. The coherence length, l, for atoms is given by

$$l = \hbar / \Delta p \qquad (1.1.10)$$

where $\hbar$ is Plank's constant and Δp is the momentum spread of the atom. The coherence length is basically the extent of the wavefunction for an atom. The BECs are spatially coherent across their entire wave-packet. Interference results if the difference in path length is equal or less than the coherence length of the wave packet which is around 10 - 100 μm. Therefore, the BECs have a good phase coherence length so they can exhibit interference even when using complex trajectories. However, for thermal atoms, the coherence length is about $1 \times 10^{-5} \mu$m which is much smaller than the coherence length of the condensates. For this reason, the thermal atoms require a careful design to make sure the waves overlap at the recombine where as the BECs are not bound to such rigorous alignment.

Second, the BECs are made with temperature close to absolute zero Kelvin. The resulting effect is that BECs do not have high group velocities, just few mm/s, whereas thermal atoms have velocities in the orders of hundreds of m/s. With such low kinetic energy, BECs are much easier to manipulate with weak laser beams allowing complex trajectories. For example, a simple 180 degree reflection of a BEC wave packet would require a few mW of laser power. For thermal atoms, even a small deflection would require hundreds of mW of laser power. It is very difficult to repeatedly suspend thermal

atoms against the gravity with laser pulses. This is a limit for the thermal interferometer geometry.

The thermal atom interferometers typically obtain their arm separation by inducing a transition to the internal state of the atoms. When measuring the output state, the populations of different internal states are recorded.   Because the interferometer includes this internal state transition, the output is susceptible to noise on that transition, including effects like fluctuating magnetic fields, ac Stark shifts, and inaccuracy of the oscillator generating the transition frequency. In turn, these depend on the relative phase which is sensitive to the phase of the laser. The phase of the laser will accumulate on top of any other additional phase the thermal atoms experience. This will introduce noise to the output if there is any noise in the laser beam, which often is the case. In contrast, a condensate interferometer can easily use atoms in a fixed internal state, because the motion of the condensed atoms is easier to directly manipulate and detect.

Overall, interferometers such as the Mach-Zender type configuration [4] are best achieved using a low velocity and longer coherent source, that do not require much effort to manipulate the atom wave packets. Therefore, the characteristics of BECs intrinsically have many advantages over thermal atoms in the interferometer business. However, as much as BEC seemed to be a dominating factor, the downside is that the BEC are produced in a small quantities at a time ($\sim 10^5$ atoms at best), and they are very fragile to external effects. However, the high sensitivity it offers may outweigh the disadvantages.

1.2   Motivation – Gravity and Recoil Frequency

With an ultra-cold atom interferometer with BEC, we can measure external effects like rotation, acceleration, electric fields, magnetic fields, fundamental constants such as electric polarizability, atomic kinetic energy, and gravity. Contemporary research with atom interferometers encompasses goals from measuring fundamental constants to purely application oriented military/commercial development. In this study, and in possible extensions from this study, we are mainly interested in measuring two quantities – 1) gravity, and 2) atomic kinetic energy.

First, accurately measuring gravity is important because many hidden underground features affect gravity values. For example, underground tunnels, oil and mineral deposits, and underground geological anomalies affect local gravity values. Digging to find these features is time consuming and takes time and resources. Hence a simple, quick, compact and an accurate way to ascertain the gravity value is needed. Using BEC may provide a solution to this problem. Several preliminary studies, both theoretical and experimental, point to its feasibility [1].

To approach measuring gravity with BEC interferometer, we go back to the hypothetical atom interferometer with trajectories previously shown in Fig. 1.2. In reality, these atom "splitters, mirrors, and re-combiners" do not exist as simple physical units like the beam splitters and mirrors in laser interferometry. Instead, these manipulations are done by pulsed laser beams to change the momenta of the wave packet velocities allowing the atom paths as shown in Fig. 1.3. Nevertheless, in this atom interferometer, if any one of those wave packets is exposed to the external effects such as gravity, a phase is introduced to the wavefunction and changes the resulting interference intensity as $\sin^2 \phi$ and $\cos^2 \phi$ where ϕ is the phase.

In addition to measuring gravity, the interferometer geometry in Fig 1.3 is well suited to measurement of kinetic energy, since the atoms move along one path but is stationary in the other. From this measurement, a value for the atomic recoil frequency can be obtained. This is a basic atomic parameter closely related to several important fundamental constants. When an atom absorbs or emits a photon, the atom recoils with a momentum $p = \hbar k$ where k is the wavevector. The resulting kinetic energy $\hbar^2 k^2 / 2m$ defines the recoil frequency $\hbar \omega_r$. By measuring the phase from the kinetic energy in the interferometer, ω_r can be measured, in principle very accurately. We will discuss how to measure the recoil frequency in more detail in later chapters.
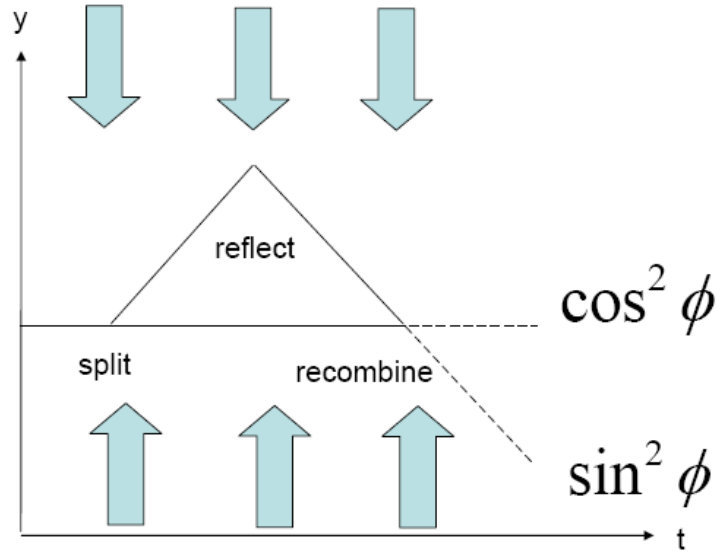
Figure 1.3   Atom wave packet trajectories and corresponding laser pulses.   Atom interferometer can also measure external effects such as gravity via phase measurement. Unlike Fig. 1.2. atom splitters, mirrors, and recombiners do not exist.   Instead, atom manipulations are done via laser pulses.

Before proceeding further, one must understand how much sensitivity can be achieved with a given separation and time.   To illustrate this, consider a gravity measurement.   The sensitivity on gravity in an atom interferometry is

$$\delta g = \frac{\hbar}{m} \frac{d\phi}{(t)(\Delta z)} \qquad (1.2.1)$$

where $d\phi$ is the accuracy of the phase measurement. The best conventional mechanical gravitational acceleration sensors have $\delta g = 4.9 \times 10^{-8} \, \text{m/s}^2$ after 15 minutes measurements averaged [1]. To improve on the gravity sensitivity with an atom interferometry, it is obvious one would want a large separation, Δz and time, t. For example, a separation of 1 cm with time of 1 second, and measuring $d\phi$ accurately to within 0.01 radians would yield $\delta g = 7.27 \times 10^{-10} \, \text{m/s}^2$. This is nearly a factor of 100 gain and measurement could take only 1 second. This would definitely be an advantage, for example, in a hostile environment where you do not have 15 minutes to make a measurement.

As indicated earlier, scientists have used thermal atoms to measure gravity. The first measurements of g with matter-wave interferometer with neutrons were done by Colella *et al.* (1975) [6], followed by atom experiments by Kasevich and Chu [7] in 1992. There are several more experiments using thermal atoms; notably, Peters *et al.* 1997, 1999, 2001 [8, 9, 10]; Schmiedmayer *et al.* 1997 [11]; McGuirk *et al.* 2002 [12]. To compare some of the sensitivities obtained in these experiments, McGuirk et. al 2002 used thermal atoms in a "fountain" experiment, launching atoms 12 cm high in 320 ms and yielding sensitivity of $\delta g = 5.06 \times 10^{-9} \text{m/s}^2$ in 1 minute averaged measurement. Peters *et al.* 1997 also uses fountain and improved gravity measurements to $\delta g = 3 \times 10^{-9} \, \text{m/s}^2$ with 1 minute measurement and $\delta g = 1 \times 10^{-10} \, \text{m/s}^2$ with 2 days of averaging. Fountains and long drop experiments make the apparatus big and also introduce side effects with falling time. For instance, since the fall distance increases as

$d \sim t^2$, improving the sensitivity rapidly leads to even larger systems. This makes the apparatus non-compact and difficult for practical use. Furthermore, over a long drop distance, the gravity is not constant throughout the apparatus, which leads to significant complications [13]. It is also more challenging to protect the atoms from other environmental effects. For example, the magnetic fields B contributes a large energy $U = -\vec{\mu} \cdot \vec{B}$, where $\vec{\mu}$ is the magnetic moment, and must therefore be precisely stabilized over the entire drop distance which becomes challenging [13].

To address these effects and to keep the system small, we propose to improve from a free-falling thermal atom configuration to something more compact so that the atoms do not drop very much but still gain sensitivity to measure g accurately. Our idea is to separate the BEC atoms against gravity by repeated laser pulses. Hence the BEC atoms separate from each other to get a large Δz, but never actually fall a significant distance, only in the orders of ~ cm total. However, the sensitivity one would gain by continuously separate atoms for a long time (~1 s) would be ideal as the system is compact but still gains sensitivity. This proposed concept first needs the key ingredient: BEC.

1.3 Bose-Einstein Condensate

The BEC is best described as a collection of atoms sharing the same wavefunction. This is equivalent to a coherent laser beam with many photons sharing the same electric field. The BEC is the key ingredient for our proposed method because our interferometer requires atoms with a very narrow velocity distribution. Without going too much into details of BEC, we will simply go over pertinent information needed to

understand our atom interferometry. Readers are invited to thoroughly understand BEC from list of references [14,15].

The understanding of Bose-Einstein condensate starts with the Bose-Einstein energy distribution which is

$$f(\varepsilon) = \frac{1}{e^{(\varepsilon - \mu)/k_B T} - 1} \qquad (1.3.1)$$

where ε is energy of boson, μ is chemical potential energy, k_B is boltzmann's constant, and T is temperature. For bosons as T goes to zero, occupation of the lowest energy ($\varepsilon = 0$) can get macroscopically large, and a phase transition occurs – a Bose-Einstein condensate forms.

The phase transition can be understood by examining a particle's thermal de Broglie wavelength defined as

$$\lambda_{dB} = \sqrt{\frac{2\pi \hbar^2}{m k_B T}} \qquad (1.3.2)$$

where m is mass of the particle. The thermal de Broglie's wavelength quantifies the quantum uncertainty in the atom's position: $\Delta x \simeq \lambda_{dB}$. At high temperatures, the atoms are very well localized in position. However, for low temperatures, the uncertainty in position is increased and the wave nature of the particle starts to dominate over the particle nature. At very low temperatures, the de Broglie wavelength is long enough that the individual wavefunctions start to overlap, constructively interfering due to exchange property of bosons, forming the condensate. For example, Rb at 1 nK, $\lambda_{dB} = 6$ μm where as at 300 K, $\lambda_{dB} = 0.01$ nm. To be considered a BEC, the density n must be high enough

that the number of atoms per cubic wavelength approaches one. This quantified with the phase space density which is represented as

$$PSD = n\lambda_{dB}^3 . \tag{1.3.3}$$

BEC occurs for $PSD > \zeta(3/2) = 2.61$ where ζ is the Reimann Zeta function. The chemical potential μ is effectively zero at this transition. We find the critical temperature by plugging in (1.3.2) into (1.3.3), yielding

$$T_C = \left(\frac{n}{2.61}\right)^{2/3} \frac{2\pi\hbar^2}{mk_B} . \tag{1.3.4}$$

For ^{87}Rb we find $T_C \approx 8 \times 10^{-8}$ K (density $\sim 10^{19} \, \text{m}^{-3}$). For a complete derivation on the Bose-Einstein condensate, readers are encouraged to a plethora of excellent books [16, 17, 18].

Our BECs are formed by laser cooling, magnetic trapping, and evaporative cooling. The end product is a collection of 10^4 ^{87}Rb atoms with temperature of around 1 nK acquired in the lab. The production process takes 100 seconds. We will discuss production of BEC in more details in chapter 4. The main concept needed to know for now is that the BEC is a coherent source for cold-atom interferometry, which makes use of its matter wave as atom wave packet, splitting, reflecting, and recombining to make an interferometer.

1.4 Symmetric vs. Asymmetric Splitting

To achieve an atom interferometer, one has to split the BEC wave packet, propagate the two packets some distance and have one or both arms of the wave packet exposed to an external effect. The packets are then recombined and finally we quantify

the interference signal it produces. As mentioned before, these manipulations are done via pulsed laser beams by transferring the momentum from photons to atoms.

Previously in our lab, the splitting has been done symmetrically. We use a single frequency, ω, laser beam and create a standing wave on top of the atoms by retro-reflecting the incoming laser beam as shown in Fig. 1.4. This configuration transfers momentum to the atoms equally in both directions, allowing an even split. The result is two distinct wave packets propagating in the opposite directions from each other. Using such technique, the previous atom interferometer measured gravity, the ac and dc electric polarizability, and is currently pursuing a gyroscope measurement. Although useful, the symmetric technique has some limitations that will be discussed below.
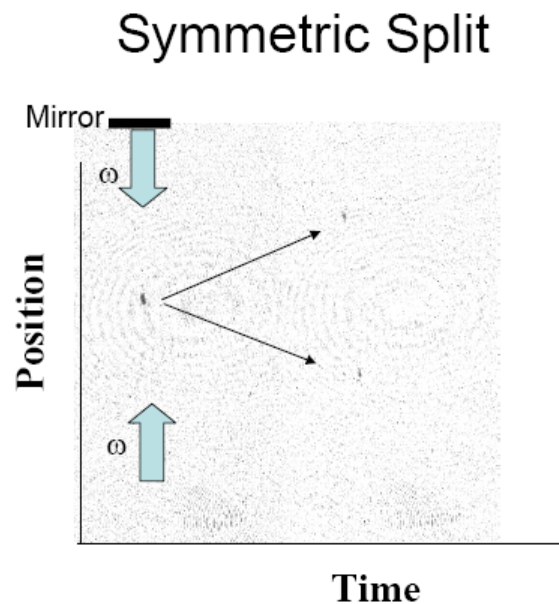
Figure 1.4 Symmetric splitting is done by sending one frequency (ω) laser beam and retro-reflecting from a mirror. This configuration creates standing wave which splits atoms evenly.
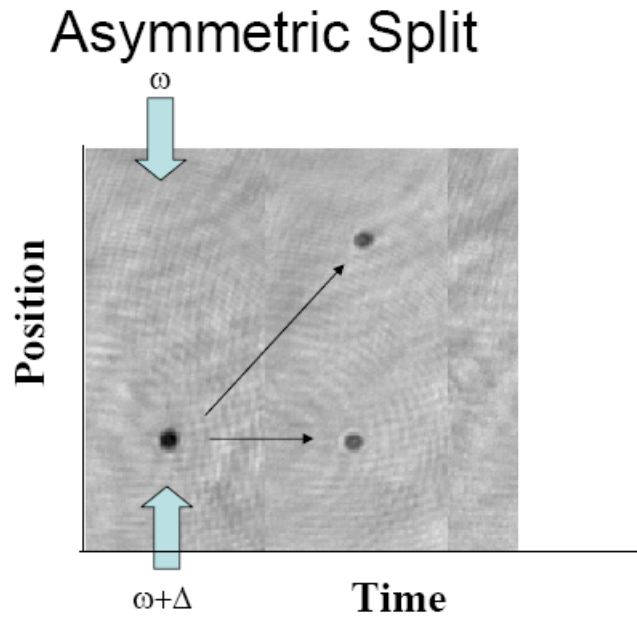
Figure 1.5 Asymmetric splitting is done by having two different frequency laser beams on atom wave packet. This creates the traveling standing wave, allowing asymmetric splitting.

In this study, we will change the symmetric scheme by splitting the wave packet asymmetrically with laser beams of non-equal frequency as shown in Fig. 1.5.   With this new configuration, which creates a traveling standing wave, we can split the atom wave packet asymmetrically, allowing greater flexibility in building an atom interferometer with different path ways, which will permit an improved gravity measurement method, and also allows recoil frequency measurement.   Nevertheless, the pulsed laser manipulation of the atom packets remains the key factor and must be understood thoroughly in quantum mechanics.   As you will see in the next chapter, we describe the transitions of atoms in a two-level system using quantum mechanics and use the Schrodinger's equation to understand the cyclic behavior of atoms in that two-level systems in the presence of two color laser beams.

1.5   Asymmetric Splitting of BEC Elsewhere in the World

Many scientists around the world have experimented with symmetric splitting. Two counter-propagating laser beams with an equal frequency creates the standing wave, making the atoms to split evenly. However, an asymmetric atom interferometer is not easily found in labs around the world. There have been just few cases of such work.

Back in 1999, Kozuma *et al*. (1999) a group from NIST-Gaithersburg have successfully split BEC of Sodium atoms asymmetrically with multiple orders *nℏk* of momentum states [19]. They report 1st order (n=1) asymmetric split with 100% efficiency, followed by 2nd and 3rd orders with 45%, and up to 6th order with efficiency 15%. Although asymmetric splitting was demonstrated, an interferometer of such type to measure recoil frequency or other measurements is not realized. Gupta *et al*. (2002) from MIT have built a modified type 'triple' splitting interferometer using Kapitza-Dirac pulse to measure the recoil frequency to ascertain the fundamental $\frac{h}{m}$ value accurately [20]. Horikoshi and Nakagawa 2007 from Japan have demonstrated the asymmetric interferometer experiment to measure the magnetic trap frequency [21]. Their proof-of-concept shows that asymmetric splitting can be used to make Sagnac rotational interferometer. However, a recoil frequency measurement with reflect and recombination pulses were not developed in this study.

We are able to take a step further than the previously attempted studies to construct an asymmetric atom interferometer by adding a spatial phase detection system and an active phase stabilization system. Such system allows detection of laser phase and stabilization of its laser phases which needed to demonstrate asymmetric splitting capability. We use a combination of electro-optical modulator and a feedback electronics

to quickly correct any offset phases of the laser. Such system will be explained in the following chapters.

1.6   Summary

We explored two main types of interferometer and briefly explored that the ultra-cold atom interferometer can offer a greater sensitivity to measure gravity. Like that of the laser interferometers, the wavefunction of atoms can be constructive and destructive depending on the phase it acquires along the path. Such phase can be measured, and can ascertain what effects had affected the beam path. We can measure quantities such as gravity, electric, magnetic fields, and kinetic energy associated with the atoms such as recoil frequency. The ultra-cold atom interferometer have advantages over the thermal atom based interferometer in that it can be made smaller volume and does not require long distance drops.

2.0

Theoretical Consideration

Theoretical Foundation in Quantum Mechanics

Before embarking on developing experimental techniques to make an asymmetric atom interferometer using BEC, we explore some theoretical aspects of asymmetric splitting. We consider a simple two-level system, the quantum mechanics of asymmetric splitting, and the general Schrodinger's equation governing the beam splitting process. These provide a firm foundation for developing the experiment according to our required criteria.

2.1 Asymmetric Schrodinger's Equation
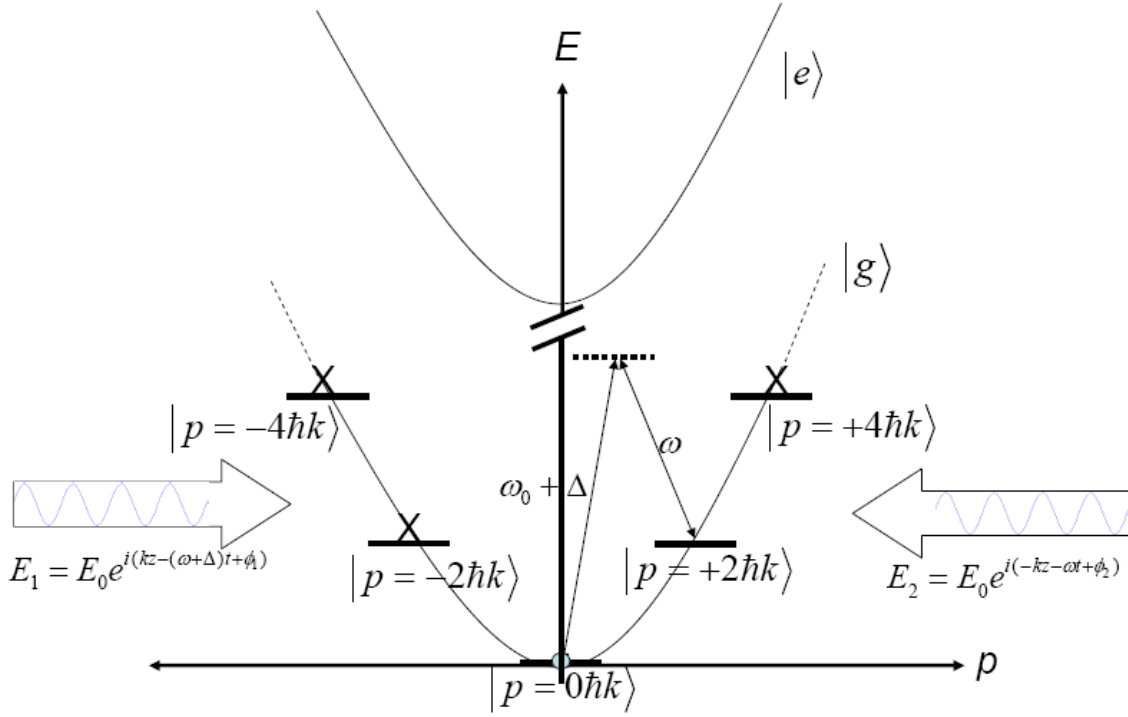
Figure 2.1. Energy level diagram for asymmetric splitting. An atom packet in the ground state $|p=0\rangle$ transitions to an excited state $|p=+2\hbar k\rangle$. A photon-atom momentum transfer occurs with a stimulated emission. Atoms gain total of $2\hbar k$. All other transitions are considered eliminated with "X" symbols. The shape of the curve for ground state and excited states are dictated by the relationship $E = p^2 / 2\mathrm{m}$.

To asymmetrically split the atom packet with pulsed laser beams, we need to understand the interaction picture of the laser beams with atoms. We know from physics that a quantum mechanical wave is governed by the Schrodinger's equation. Hence, the light interaction with atoms begins with the understanding of the Schrodinger's equation first. We can then build an evolution model from it. Let us consider two non-equal frequency counter-propagating laser beams as shown in Fig. 2.1 in which their electromagnetic waves are represented by $E_1(z,t) = E_0 e^{i(-kz-(\omega+\Delta)t+\phi_2)}$ and $E_2(z,t) = E_0 e^{i(kz-\omega t+\phi_1)}$ where E_0 is the amplitude of electric field, Δ is the frequency

difference between the two laser beams, and the variables k, ω, and ϕ represent the wavevector, angular frequency, and laser phase, respectively. At the atoms, the incident laser beams have combined total $E_{total}(z,t)$ field

$$E_{total}(z,t) = E_0 e^{i(kz-\omega t+\phi_1)} + E_0 e^{i(-kz-(\omega+\Delta)t+\phi_2)} \qquad . \qquad (2.1.1)$$

We factor out $e^{-i(\omega+\frac{\Delta}{2})t}$ and set $\dfrac{\phi}{2} = \dfrac{\phi_1-\phi_2}{2}$, so the $E(z,t)$ field is re-written as

$$= E_0 e^{-i(\omega+\frac{\Delta}{2})t} e^{i(\frac{\phi_1-\phi_2}{2})} [e^{i(kz+\frac{\Delta}{2}t+\frac{\phi}{2})} + e^{-i(kz+\frac{\Delta}{2}t+\frac{\phi}{2})}] \qquad (2.1.2)$$

Using Euler's identity

$$= E_0 e^{-i(\omega+\frac{\Delta}{2})t} e^{i(\frac{\phi_1-\phi_2}{2})} [2\cos(kz+\frac{\Delta}{2}t+\frac{\phi}{2})] . \qquad (2.1.3)$$

The magnitude squared of this field yields

$$|E|^2 = 4E_0^2 \cos^2(kz+\frac{\Delta}{2}t+\frac{\phi}{2}) \qquad (2.1.4)$$

$$= 2E_0^2[1+\cos(2kz+\Delta t+\phi)] \qquad (2.1.5)$$

The intensity is related to the electric field by the relationship $I(z,t) = |E(z,t)|^2 / 2\xi_0$

where $\xi_0 = 1/\varepsilon_0 c = 377\,\text{Ohms}$. Using the relationship for Rabi frequency [section 2.3]

$\Omega^2(z,t) = \dfrac{\Gamma^2 I(z,t)}{2I_s}$, we find the relationship

$$\Omega^2(z,t) = \frac{\Gamma^2}{2I_s\xi_0} E_0^2[1+\cos(2kz+\Delta t+\phi)] \qquad (2.1.6)$$

The two beams incident on the atoms will shift energy level of an atom via a potential that it creates. This is important as the atomic interaction with light plays a vital role in the optical manipulation of atoms. Specifically, for the detuning frequency Δ_d, the light

shifts the energy of the ground state by $V = \hbar \dfrac{\Omega^2}{4\Delta_d}$. Hence, ignoring the constant term

which simply offsets the energy, upon substitution, we get

$$V(z,t) = \frac{\hbar \Gamma^2}{8 I_s \Delta_d \xi_0} E_0^2 \cos(2kz + \Delta t + \phi) \qquad (2.1.7)$$

To make the equation (2.1.7) more simpler, we introduce the intensity parameter where

$$\beta = \frac{\Gamma^2 E_0^2}{8 I_s \Delta_d \xi_0} = \frac{\Gamma^2 I_0}{4 I_s \Delta_d} \text{ and } I_0 = \frac{E_0^2}{2\xi_0} \text{ yielding}$$

$$V(z,t) = \hbar \beta \cos(2kz + \Delta t + \phi) \qquad (2.1.8)$$

where $\Gamma = 2\pi \times 6\,\text{MHz}$ as the natural line-width, I_0 as the intensity of the standing wave,

and I_s as the saturation intensity which is 2.504 mW/cm^2 for our atoms and linear

polarization. Equation (2.1.8) describes a traveling standing wave.

The Schrodinger's equation is now

$$-\frac{\hbar^2}{2m} \frac{d^2\psi}{dz^2} + (\hbar \beta \cos(2kz + \Delta t + \phi))\psi = i\hbar \frac{d\psi}{dt}. \qquad (2.1.9)$$

The Schrodinger's equation from (2.1.9), gives us the relationship between the potential

created by the two laser beams and the wavefunction of the atom packet.

2.2 Theoretical Derivation - Population Density

We need to solve equation (2.1.9) to gain an understanding of the interaction. We

first approach this relationship using expansion of the eigen wavefunction. The

expansion of wave function in momentum basis is equation is simply

$$\psi(z) = \sum_{n=-\infty}^{+\infty} C_n(t) \left| 2n + \delta \right\rangle \qquad (2.2.1)$$

where $C_n(t)$ is time dependent population coefficient, $|n\rangle$ is the state with momentum $n\hbar k$, and $\delta = \dfrac{mv_0}{\hbar}$ where v_0 is the initial velocity of the atoms. Note that the expansion shows that the potential only couples the atomic states with momentum difference of $2n\hbar k$ because our interaction only allows the transition of that difference by a photon-recoil interaction. All other states are excluded. Re-writing the wave function in the position basis

$$\psi(z) = \sum_{n=-\infty}^{+\infty} C_n(t)e^{i(2n+\delta)kz} \qquad (2.2.2)$$

The first and second derivatives are

$$\frac{d\psi}{dz} = \sum_n C_n(t)i(2n+\delta)ke^{i(2n+\delta)kz} \qquad (2.2.3)$$

$$\frac{d^2\psi}{dz^2} = -\sum_n C_n(t)(2n+\delta)^2 k^2 e^{i(2n+\delta)kz} \qquad (2.2.4)$$

Substituting the equations (2.2.3) and (2.2.4) into (2.1.9) and changing the $\cos(kz)$ term in the middle into exp notations with $\omega_r = \dfrac{\hbar k^2}{2m} = 2.36 \times 10^4 \, s^{-1}$

$$\omega_r \sum_n C_n(t)(2n+\delta)^2 e^{i(2n+\delta)kz} + \frac{\beta}{2}\sum_n C_n(t)\left(e^{i[(2(n+1)+\delta)kz+\Delta t+\phi]} + e^{i[(2(n-1)+\delta)kz-\Delta t-\phi]}\right) = i\sum_n \dot{C}_n(t)e^{i(2n+\delta)kz}$$

$$(2.2.6)$$

Shifting the indices

$$\omega_r \sum_n C_n(2n+\delta)^2 e^{i(2n+\delta)kz} + \frac{\beta}{2}\sum_n \left(C_{n-1}e^{i[(2n+\delta)kz+\Delta t+\phi]} + C_{n+1}e^{i[(2n+\delta)kz-\Delta t-\phi]}\right) = i\sum_n \dot{C}_n e^{i(2n+\delta)kz}$$

$$(2.2.7)$$

Putting in all into one term and combining summations,

$$\sum_n \left\{ C_n \omega_r (2n + \delta)^2 + \frac{\beta}{2} \left(C_{n-1} e^{i[\Delta t + \phi]} + C_{n+1} e^{-i[\Delta t + \phi]} \right) - i\dot{C}_n \right\} e^{i(2n+\delta)kz} = 0 \qquad (2.2.8)$$

If we set $\tau = \omega_r t$, and $\tilde{\beta} = \frac{\beta}{\omega_r} e^{i\phi}$ and $\tilde{\beta}* = \frac{\beta}{\omega_r} e^{-i\phi}$, equation (2.2.8) reduces to

$$i \frac{dC_n}{d\tau} = C_n (2n + \delta)^2 + \frac{1}{2} (\tilde{\beta} C_{n-1} e^{i\tilde{\Delta}\tau} + \tilde{\beta}* C_{n+1} e^{-i\tilde{\Delta}\tau}) \qquad (2.2.9)$$

Equation (2.2.9) is a state coupling equation which governs the population states for the atoms during the manipulation of asymmetric split, reflect, and recombine of the wave packets. These manipulations are performed using pulsed laser beams by transferring momentum between photons to atoms. Equation (2.2.9) is hard to solve exactly with analytical approach. One approach is to investigate it with numerical modeling, as will be discussed in section 2.4. Another approach is to reduce the equations to an approximate two-level system, which can be solved analytically in the next section.

2.3   Two Level System Review

We can approach the two-level system with an analytical model first before attempting to solve with the numerical programming. We start with a solid foundation by reviewing the basic two-level system.

Let us first consider a multi-level energy system as shown in Fig. 2.1. The atom, initially at the ground state $|g\rangle$ with momentum $p = 0$ can be excited to a momentum $p = +2\hbar k$ state by absorbing a detuned laser beam, excited to a virtual state ΔE with momentum $+\hbar k$ temporarily, as indicated in dotted-line just below the excited level $|e\rangle$. If the atom emits a stimulated photon in the opposite direction of the higher frequency incident beam it gains another momentum kick $+\hbar k$ and finally arrives at the ground

state with total recoil momentum $+2\hbar k$.   Contrarily, if the excited atom emits a stimulated photon in the same direction of the higher frequency incident beam, it will lose $-\hbar k$, then the atom will return to its original state ($p = 0$).   The stimulated emission is represented by $E_e - E_g = \hbar\omega_s$ where the E_i represents the energy of the ground and the excited states and ω_s is the angular frequency of the stimulated emission.   All other momentum states are off-resonant with the correct Δ only allowing the transition from $p = 0\hbar k$ to $p = +2\hbar k$ state.   Hence the other states are indicated by "X" in Fig. 2.1.

It is important to realize that the frequencies of the stimulated photon generated from the excited state atom depend on the incoming beam's pulse time.   The uncertainty of a BEC is only limited by the uncertainty principles $\Delta x \Delta p \sim \hbar$ and $\Delta E \Delta t \sim \hbar$ where the variables Δx, Δp, ΔE, Δt stand for the uncertainties in position, momentum, energy, and time, respectively.

Elaborating further, the energy equation can be re-written as $\Delta\omega\Delta t \sim 1$ where ω is interpreted as the frequency of a laser driving an atomic transition, and Δt the time duration of the laser pulse.   This gives us a tool to control the frequency sensitivity if we have a well defined pulse time Δt.   For example, we if have a long laser pulse exciting an atom from a ground state to an excited state, then we can be certain that when the atom eventually returns to the ground state by a stimulated emission, the frequency of the stimulated emission $\Delta\omega$ generation is limited to a very narrow window of frequencies. However, if we have a very short pulsed beam, then the rule suggests that we have a wider range of stimulated emission frequencies.   Hence depending on how short or long the pulsed beam is, the stimulated photons with different frequencies can be generated. The frequency emitted may not always be the same as the frequency absorbed.   This is

not a drawback but actually an advantage when it comes to optical manipulation of atoms. We have better control of the frequencies, allowing us to, at times, eliminate certain transitions, or allow other transitions. For instance, we choose laser pulse duration such that the final kinetic energy $\frac{(2hk)^2}{2m}$ is within the uncertainly limit, but the exchange of four photons, leading to final energy $\frac{(4hk)^2}{2m}$, is suppressed. This tool is used to selectively split the atom packets as desired.

For short interaction times, we can safely assume that the kinetic energy in equation (2.1.9) is negligible since the wavefunction which describes the wave packet will not move much while applying the pulse. Hence we can directly calculate the components in the Hamiltonian matrix, i.e.

$$\langle +2|H|0\rangle = \int dz \langle +2|z\rangle \hbar\beta \cos(2kz + \Delta t + \phi)\langle z|0\rangle = \frac{\hbar\beta}{2} e^{i(\Delta t+\phi)} \tag{2.3.0}$$

and get

$$H = \hbar \begin{bmatrix} 0 & \frac{\beta}{2} e^{i(\Delta t+\phi)} \\ \frac{\beta}{2} e^{-i(\Delta t+\phi)} & 4\omega_r \end{bmatrix}. \tag{2.3.1}$$

The Schrodinger's equation is

$$i\hbar \frac{d}{dt}|\psi\rangle = H|\psi\rangle \tag{2.3.2}$$

where $|\psi\rangle$ is the wavefunction. We write the wave function as superposition of the ground state and the excited state as

$$|\psi\rangle = c_g|0\rangle + c_e|2\rangle \tag{2.3.3}$$

where c_g and c_e are the population coefficients for the ground and the excited states, respectively. We define these coefficients as time dependent as, $c_e(t) = d(t)e^{-i\Delta t}$ where $d(t)$ is slowly varying amplitude. We use Rotating Wave Approximation (RWA) which is a mathematical technique yielding valid approximation when the applied electromagnetic radiation is near resonance with an atomic transition and the intensity is low. With it, the effective Hamiltonian can be re-written as

$$H_{eff} = \hbar \begin{bmatrix} 0 & \dfrac{\beta}{2}e^{i\phi} \\ \dfrac{\beta}{2}e^{-i\phi} & -\Pi \end{bmatrix} \tag{2.3.4}$$

where $\Pi = \Delta - 4\omega_r$. So we let the wavefunction evolve in time

$$\left|\psi'(t)\right\rangle = U(t)\left|\psi'(0)\right\rangle \tag{2.3.5}$$

and use appropriate ansatz for $d(t) = Ae^{i\mu t} + Be^{-i\mu t}$ where A and B are coefficients which are calculated with boundary condition at t = 0, and $\mu = \dfrac{1}{2}(\Pi \pm X)$ with $X = \sqrt{\beta^2 + \Pi^2}$.

Solving the relationship yields $d(t)$ and $c_g(t)$ which yield the $U(t)$ which is the time evolution operator

$$U = e^{i\frac{\Pi t}{2}} \begin{bmatrix} \cos\dfrac{Xt}{2} - i\dfrac{\Pi}{X}\sin\dfrac{Xt}{2} & -i\dfrac{\beta}{X}\sin\dfrac{Xt}{2}e^{i\phi} \\ -i\dfrac{\beta}{X}\sin\dfrac{Xt}{2}e^{-i\phi} & \cos\dfrac{Xt}{2} + i\dfrac{\Pi}{X}\sin\dfrac{Xt}{2} \end{bmatrix} . \tag{2.3.7}$$

From equation (2.3.7) we can calculate various experimental parameters (in experiment chapter) such as $\dfrac{\pi}{2}$ – pulse. For example, to split the atoms asymmetrically with equal population distribution on two packets, we use values $\Pi = 0$ which we infer

$\Delta = 4\omega_r$ and $X = \beta$. Hence starting with the initial population in the ground state, we get

$$\begin{bmatrix} c_g(t) \\ d(t) \end{bmatrix} = e^{i\frac{\Pi t}{2}} \begin{bmatrix} \cos\dfrac{\beta t}{2} & -i\sin\dfrac{\beta t}{2}e^{i\phi} \\ -i\sin\dfrac{\beta t}{2}e^{-i\phi} & \cos\dfrac{\beta t}{2} \end{bmatrix} \begin{bmatrix} 1 \\ 0 \end{bmatrix} \qquad (2.3.8)$$

$$\begin{bmatrix} c_g(t) \\ d(t) \end{bmatrix} = \begin{bmatrix} \cos\dfrac{\beta t}{2} \\ -i\sin\dfrac{\beta t}{2}e^{-i\phi} \end{bmatrix} \qquad (2.3.9)$$

For equal population we set $\cos^2\left(\dfrac{\beta t}{2}\right) = \sin^2\left(\dfrac{\beta t}{2}\right)$ from which is only true if

$$\beta t = \frac{\pi}{2} \qquad (2.3.10)$$

Hence this is the reason why we call the even split, the $\dfrac{\pi}{2}$ – pulse. With the intensity parameter β fixed, we can calculate the pulse time at which we achieve an even split occurs from the condition in equation (2.3.10). For a pulse that populates the excited state, we set $\sin^2\left(\dfrac{\beta t}{2}\right) = 0$ from which

$$\beta t = \pi \qquad (2.3.11)$$

Hence the total population inversion from the ground state to the excited state is called a π – pulse.

It is also useful to understand the asymmetric splitting with $\dfrac{\pi}{2}$ – pulse in quantum mechanical notations. For symmetric splitting as illustrated in Fig. 2.1, noting the bra-ket

notation represents its momentum state in units of $\hbar k$, the splitting of the atom packets from the zero momentum in its equivalent quantum operation is,

$$|0\rangle \to \frac{1}{\sqrt{2}}\left(|0\rangle + |+2\rangle\right) \tag{2.3.12}$$

This means that the wave packets go from the rest state, $p = 0\hbar k$, to the split states with momenta $0\hbar k$ and $+2\hbar k$. If we choose the pulse duration to be corresponding with a $\frac{\pi}{2}-$ pulse as indicated in equation (2.3.10), the wave packet is split 50/50 to $p = 0$ and $p = +2\hbar k$. However, if we choose a pulse time duration corresponding to a $\pi-$ pulse as shown in equation (2.3.11), the atoms transfer 100% to $p = +2\hbar k$ state. Equation (2.3.12) is the main operation of this thesis. We want to be able to split asymmetrically so that the ½ of the atoms remain at rest while the other ½ is moving away with $+2\hbar k$ momentum.

For reflection, while the wave-packet is moving away with momentum $\pm 2\hbar k$, we apply a pulse to drive the $4\hbar k$ total transition, allowing the atom to change direction and propagate in the opposite direction. For example, the atom, initially at the $-2\hbar k$ state will absorb a photon from left and emit a stimulated photon to the opposite direction gaining recoil net of $+2\hbar k$ and making the transition to $0\hbar k$ state. Immediately after, the atom repeats the photon absorption-stimulated emission cycle and finally arrives at $+2\hbar k$ state. The atoms has just been reflected, changing the initial momentum from $-2\hbar k$ to $+2\hbar k$ state by gaining the total momenta of $+4\hbar k$. The quantum state representation is,

$$|+2\rangle \leftrightarrow |-2\rangle. \tag{2.3.13}$$

which means the atom can go from $p = +2\hbar k$ state to $p = -2\hbar k$, or vice versa. Reflection is not something new but was used in previous symmetric experiments [14,15]. For analytic solution to the reflect pulse, it require bit more work. The reflect pulse drives three transitions in series: $|+2\rangle$ to $|0\rangle$ and then finally to $|-2\rangle$. Hence an analytical solution is not possible hence if desired, need to solve numerically much like the Rabi solution. Rob Horne has performed this calculation and obtained a numerical value as will discuss in chapter 6.

For recombining, as the atom packets are coming together, a laser pulse with one laser beam frequency switched from $\omega + \Delta$ to $\omega - \Delta$ can recombine the atom wave-packets as,

$$\frac{1}{\sqrt{2}}\left(|+2\rangle + |0\rangle\right) \rightarrow |0\rangle \tag{2.3.14}$$

where the wave-packets traveling with momentum $+2\hbar k$ to come to rest, $p = 0$.

2.4   Numerical Simulation

We now consider a numerical solution to the analytical problem considered in section 2.3. We solve equation (2.2.9) numerically, with initial velocity $\delta = 0$, including the indices n up to ± 6. We only calculate n up to ± 6 as the dominant population states are between $n = 0$ and ± 2 and other higher states probability amplitudes are small and are safely neglected. We investigate the behavior of the population density in the presence of asymmetric beams by plotting the probability of states of interest, in our case, $|0\rangle$, $|+2\hbar k\rangle$, and $|-2\hbar k\rangle$ states, and see how this varies with time. The plot in Fig. 2.2 represents the normalized population of the two states, $|0\rangle$ and $|+2\hbar k\rangle$ for $\beta = 1$. The

major behavior we observe is a Rabi oscillation of the population between the two states. It is obvious that mainly the two states, C_0 and C_{+1} oscillate population while the third state C_{-1} is insignificantly affected (not shown). We note that as the parameter β is increased, the Rabi oscillation frequency increases as well. This also tells at which laser beam pulse times, either equal inversion ($C_0 = \frac{1}{2}$ and $C_{+1} = \frac{1}{2}$) or total inversion ($C_0 = 0$ and $C_{+1} = 1$) occurs. Such pulses are labeled as the $\frac{\pi}{2}$ – pulse or the π – pulse, as previously mentioned. For the graph shown in Fig. 2.2, we can have the $\frac{\pi}{2}$ – pulse occurring at 1.75μs where as the π – pulse occurs at 3.5μs which is twice as long as the pulse times for the other pulse.
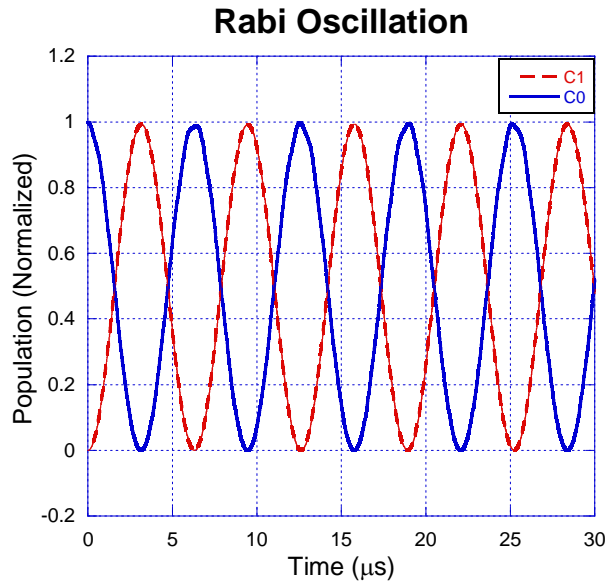
Figure 2.2 Shows Rabi oscillation, for $\beta = 1$, between C_0 (blue) and C_{+1} (red). The population density inversion is mainly between C_0 and C_{+1} with negligible amount in C_{-1}.

Splitting Efficiency
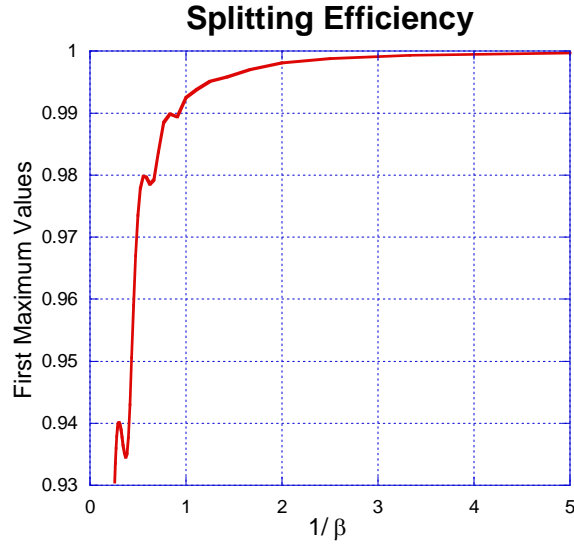
Fig. 2.3   Maximum population inversion efficiency for a given β. We would prefer higher inversion around $1 / \beta \approx 0.5$.

We studied the Rabi oscillation curves for β values ranging from 0.2 to 4 and ascertain the first $\pi -$ pulse total inversion efficiency. For various values of β where the maximum $\pi -$ pulse population inversion occurs, we investigate this inversion efficiency relationship to ascertain at which β, the desired (maximum) population inversion occurs as shown in Fig. 2.3. As β increases, the coupling to the other states increases, so that the efficiency of the $\pi -$ pulse drops. However, at lower β, the inversion efficiency is higher and one would immediately choose to select such values for the laser beam parameter. However, for lower β values the population inversion is very sensitive to Δ. Hence a nominal optimal value, in our case, β closer to 2 is optimal.

The graphs shown in Fig. 2.2 and Fig 2.3 form the foundation for constructing the actual experiment. We need to have the estimated values for β and pulse time t_{pulse}

before starting the experiment to get a rough idea of pulse times and intensity we need to split the atoms.

Now we have the three main atom manipulation techniques: asymmetric split, reflect, and recombine. The previous theoretical work lays the foundation for an experimental development. We want to use the asymmetric splitting to achieve an asymmetric atom interferometer, allowing us to measure the recoil frequency and gravity with much more accuracy.

2.5 Motivation Behind Recoil Frequency Measurement

The recoil frequency is interesting to measure because it relates to the fundamental measurement of the fine structure constant α - a dimensionless parameter that quantifies the strength of the electromagnetic force. This quantity is currently accurate to within 4 parts per billion (ppb) via electron positron (g-2) measurement together with QED. We approach this from atomic physics perspective as,

$$\alpha = \frac{2R_\infty}{c}\frac{h}{m_e} = \frac{2R_\infty}{c}\left(\frac{M}{M_e}\right)\left(\frac{h}{m}\right) \tag{2.5.1}$$

where R_∞ is Rydberg constant (0.008ppb), M_e is electron mass (0.7ppb). M and m are test particle masses. The equation offers possibility to accurately measure α in ppb if M and $\frac{h}{m}$ can be measured accurately. From the recoil frequency,

$$\omega_{rec} = \frac{1}{2}\frac{\hbar}{m}k^2 \tag{2.5.2}$$

where k is wave vector of the photon absorbed by the atom. Recently, Cesium, M_{Cs}, have been measured 0.17 ppb, k_{Cs} to within 0.12 ppb, and $\omega_{rec,Cs}$ have been measured at

Stanford with atom interferometer to 6 ppb. Hence we can also use Rb to measure $\omega_{rec,Rb}$.

In our test, we are not pursuing an accuracy to ppb but using it as a test to our system.

With further improvements in the future, it might be possible to accurately measure to

within 1 ppb.

2.6 Interferometers

We investigate a few asymmetric interferometers using the operations asymmetric

split, reflect, and recombine.   The simplest interferometer we experiment is an

interferometer where the atoms are asymmetrically split only to be followed immediately,

short wait time τ, by another asymmetric split. We control the wait time between the

two pulses to be very short so that the atoms do not have enough time to separately

completely, but have two distinct packets with different momenta. After the second split

we give the atoms enough time to separate, which is often called time-of-flight.

The basic idea behind the time-of-flight is to wait a relatively long time until the

packets are separated with a significant distance. At the end of time-of-flight, we can

measure the number of atoms in different output states and will be used to ascertain the

phase information via the number of atoms, N_0 / N_{total} where N_0 is the number of atoms

left in rest state and N_{total} is the total number of atoms in the system (both states) after the

recombination. By measuring the period, we can measure the interference output.

The purpose of this interferometer is to test the asymmetric splitting operation.

We find that the probability of finding atoms in state $|0\rangle$ is $\cos^2\left(\dfrac{\phi_r}{2}\right)$ while finding

atoms in state $|2\rangle$ is $\sin^2\left(\dfrac{\phi_r}{2}\right)$ where $\phi_r = 4\omega_r\tau$. We call this first interferometer the

Ramsey interferometer named after American physicist Norman Ramsey who used a

similar technique to measure the transition frequencies of atoms using magnetic

resonance.
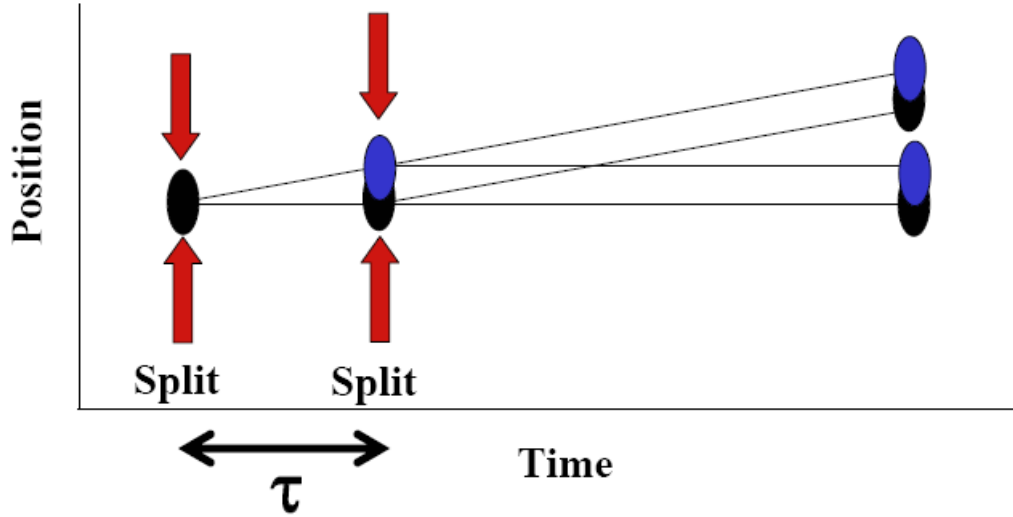
Figure 2.4. Ramsey interferometer configuration. Two identical asymmetric pulses with wait time τ in between. Atoms are separated in momentum space but spatially overlapped.
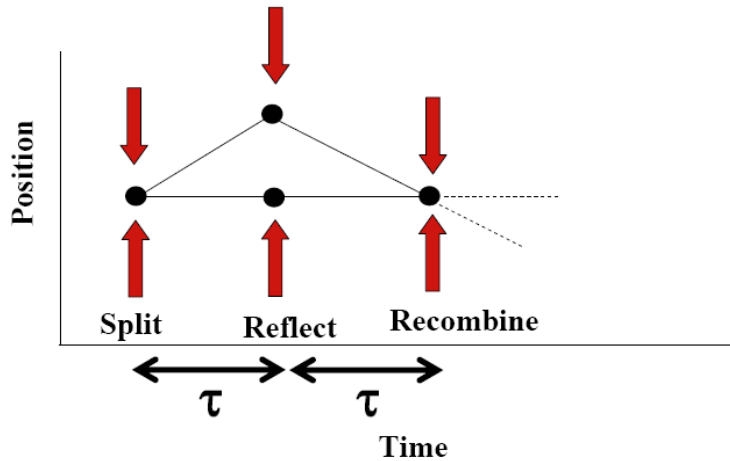
Figure 2.5. Ramsey-Borde type 1 interferometer configuration. After asymmetric split, one atom packet remains at rest while the other gains momentum $+2\hbar k$. At τ time later, a reflect pulse is applied, only reflecting the moving atom wave packet. Again at second τ time later, recombination pulse is applied, showing interference as a result.

The second interferometer we can build, as shown in Fig. 2.5 uses a single reflection. The atoms are split asymmetrically, the moving atoms are later reflected and returned back to the original position, and then finally recombined with the atoms at rest. We find that the probability of finding atoms at rest $|0\rangle$ is $\cos^2(\phi_r)$. We call this Ramsey-Borde type 1 interferometer - Borde is named after French physicist Christian Borde who use atomic recoil to create a beam splitter for an atom interferometer.

The third interferometer is the Ramsey-Borde type 2 interferometer where the moving atom packet under goes two reflections, making the path journey on both side of the initial position, and then recombining with the atoms at rest as shown in Fig. 2.6. We find that the probability of finding atoms at rest $|0\rangle$ is $\cos^2(2\phi_r)$. The only difference between RB1 and RB2 is that this one reflects twice and waits time 2τ before the second reflect pulse is applied. The total phase it experience is $4\phi_r$ compared to ϕ_r in Ramsey and $2\phi_r$ in RB1.
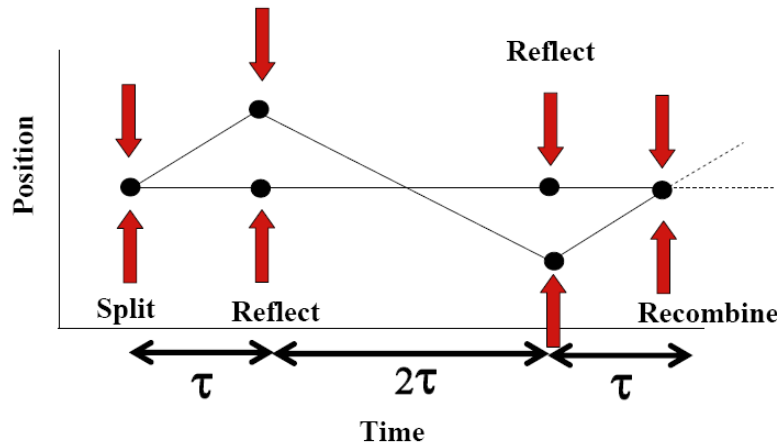
Figure 2.6. Ramsey-Borde type 2 interferometer configuration. After asymmetric split, one atom packet remains at rest while the other gains momentum $+2\hbar k$. At τ time later, a reflect pulse is applied, only reflecting the moving atom wave packet. Wait 2τ time later, second reflect pulse is applied. At τ time later, recombination pulse is applied, showing interference as a result.

For all three interferometers, since we know that $\phi_r = 4\omega_r\tau$ so for a full period, τ, we can get the value of ω_r which is the recoil frequency by measuring the period of the interference. This can be done by successfully measuring the number of atoms at rest at the end of the interferometer for different τ times.

Although we can manipulate the atom packets asymmetrically to build an atom interferometer, such a task still remains elusive as we have to consider the overall phase stability. For asymmetric split to occur, we have to stabilize the laser beams' phases. We will review this utmost importance in the next section.

2.7   The Importance of Phase Stability in Asymmetric Interferometer

In the interference output, the populations in the final momentum states depend on the phase. This includes the phase developed by the atoms as well as any uncertainty phase from the laser. With with the atom manipulation technique understood, let us investigate what happens to the phase of the atom wavefunctions during the operations.

The interferometer shown in Fig. 2.6 can be analyzed in detail including the phase introduced by the laser beam on atoms. Start with the initial atom packet at rest state with zero initial velocity $\delta = 0$ (see 2.2.1):

$$|\psi\rangle = |0\rangle \tag{2.7.1}$$

After an asymmetric split, this becomes

$$\frac{1}{\sqrt{2}}\left[|0\rangle + ie^{i\phi_1}|2\rangle\right] \tag{2.7.2}$$

where ϕ_1 is the laser phase introduced from the laser pulse. As we wait time t, the atom packet evolves in time and becomes

$$\frac{1}{\sqrt{2}}\left[|0\rangle + ie^{i\phi_1}e^{-i4\omega_r t}|2\rangle\right] \qquad (2.7.3)$$

with $\omega_r = \dfrac{\hbar^2 k^2}{2m\hbar}$. Reflecting the packet, the wavefunction becomes

$$\frac{1}{\sqrt{2}}\left[|0\rangle + ie^{i(\phi_1-2\phi_2)}e^{-i4\omega_r t}|-2\rangle\right] \qquad (2.7.4)$$

where ϕ_2 is the laser phase introduced from the reflect pulse. Let the atoms evolve over time $2t$

$$\frac{1}{\sqrt{2}}\left[|0\rangle + ie^{i(\phi_1-2\phi_2)}e^{-i12\omega_r t}|-2\rangle\right] \qquad (2.7.5)$$

Reflecting again

$$\frac{1}{\sqrt{2}}\left[|0\rangle + ie^{i(\phi_1-2\phi_2+2\phi_3)}e^{-i12\omega_r t}|+2\rangle\right] \qquad (2.7.6)$$

where ϕ_3 is the laser phase introduced from the second reflect pulse. Again let atoms evolve over time t

$$\frac{1}{\sqrt{2}}\left[|0\rangle + ie^{i(\phi_1-2\phi_2+2\phi_3)}e^{-i16\omega_r t}|+2\rangle\right] \qquad (2.7.7)$$

Finally recombine and add ϕ_4 the laser phase from the recombination pulse and finding the amplitude to be in the $|0\rangle$ state is

$$\frac{1}{2}\left[|0\rangle - e^{i(\phi_1-2\phi_2+2\phi_3-\phi_4)}e^{-i16\omega_r t}|0\rangle\right] \qquad (2.7.8)$$

The above equation (2.6.8) will result if the laser phases are uncorrected. Always results will fluctuate if phases fluctuate. It comes clear that we must be able to control the phase so that we can eliminate the phase contribution from the laser pulses. This can be done if,

at each operation, experimentally set the laser phase to zero. Hence if this is to happen, we get, $\phi_1 = \phi_2 = \phi_3 = \phi_4 = 0$. Then equation (2.6.8) reduces to

$$\frac{1}{2}\left[1 - e^{-i16\omega_r t}\right]|0\rangle \qquad (2.7.9)$$

and the probability finding the atoms at rest is

$$P_0 = \cos^2(8\omega_r t) \qquad (2.7.10)$$

Therefore, by measuring the period of the interference curve, one can measure, for example, directly, the recoil frequency ω_r.

2.8 Correcting the Laser Phase

Even though we can asymmetrically split, reflect, and recombine, the end result does not tell us anything about the recoil frequency, ω_r, unless we can control the laser phase. For asymmetric interferometer to work, we need to consider our overall laser beam phase stability. As the laser beam fluctuates and mirrors vibrate, unstable phases can be introduced onto the laser beam. In previous symmetric split experiments [Hughes 2008], a single mirror controlled the relevant laser phase (Fig. 1.4). The standing wave is produced by retro-reflecting off of that single mirror. Since the laser beam follows the same path, only that mirror has to be carefully stabilized and vibration free to keep the phases of the two beams constant. A great deal of work was put into the vibration isolation and stabilization of that mirror. However, the asymmetric splitting requires a more complex setup. Two beams with two different frequencies will follow two different optical paths with many mirrors to reach the atoms. If those mirrors vibrate independently, it changes the relative phases of the laser beams. It is very hard to

control and stabilize many mirrors. The result is the introduction of an unknown phase to the interferometer, making it noisy or even useless as shown in equation (2.6.8).

Hence for an asymmetric interferometer to work, this external phase must be corrected. Our approach is employing an active phase stabilization through an electro-optical feed back system. This stabilization system would be able to measure the phase quickly and actively correct it during the experiment. We describe in detail the active phase correction electronics in our experiment chapter.

2.9   Future Asymmetric Gravity Interferometer Concept

So far, we have not addressed specifically how we can actually measure gravity. Some of the previously mentioned interferometers can measure recoil frequency but need to be oriented vertical to measure gravity. Our motivation was to devise a method to not fall atoms very far but still achieve a longer arm separation distance to measure gravity. This is more evident by examining the proposed vertical interferometer where the wave-packets follow the path shown in Fig. 2.11. In this vertical interferometer, the two separate wave-packets experience different heights manifests in a gravitational phase, $\phi_g = \frac{1}{\hbar} \int S(t) dt$ where $S(t)$ is the action which is integrated over time t. We use the action integral as the atoms are moving in a potential where the momentum, p, is not constant. We will dig deeper into the details of manipulations and value of ϕ_g in chapter 7, however, it is worth mentioning now that we can make such interferometer and at the end of recombination, we expect interference where the probability of finding atoms at

$|0\rangle$ state is derived to be $\cos^2\left(\dfrac{\phi_g}{2}\right)$, whereas the probability at finding atoms at $|-2\rangle$

state is derived to be $\sin^2\left(\dfrac{\phi_g}{2}\right)$.
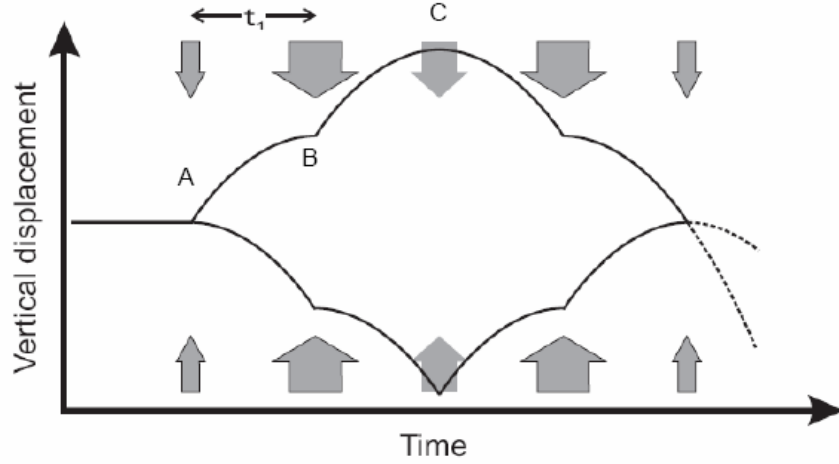
Figure 2.11   Proposed atom packet trajectory to measure gravity with better precision through large distance separation and larger separation times. This configuration would require asymmetric splitting and reflection to make it work.

Theoretically, a trajectory with 1000 pulses will yield about 1 cm separation in 1 second.   If the phase accuracy is 0.01 radians, one can achieve sensitivity to about $\delta g = 7.27 \times 10^{-10}$ m/s^2 which is a significant improvement over previous experiments and surpasses the sensitivity of a mechanical sensor.

The asymmetric splitting and recombining operation is needed to build our proposed atom interferometer. These transitions allow the atom wave-packet to gain momentum in only one direction, and require beams with slightly different frequencies. This is the main motivation for this thesis, and is the first step toward implementing interferometer of Fig. 2.11.

2.10   Summary

We explored the theoretical aspects of the asymmetric splitting and have the tools to design and configure the laser pulses' characteristics to asymmetrically split, reflect, and recombine the wave packets. It is evident that in order for our interferometer to work properly, we must find a way to stabilize the laser beam phase so that the laser phase is not introduced during the atom manipulations. The mathematical derivation in this chapter forms the basis for the instrument development, hence the goal of our instrument is to phase stabilize both beams in a very short times, in the order of few percent of the pulsed time.

We covered the theory on the interferometers and how it can measure the phase via an interference obtained at the output. With such an understanding, we are able to devise a few interferometers that use the asymmetric splitting to measure the recoil frequency and gravity. Henceforth, all we need is to build an interferometer that fits the bill. We explore such instrumentation in the next chapter.

3.0

Instrumentation

Optical & Electronics

For the asymmetric interferometer to work, as mentioned in the previous chapters, we must stabilize the laser phases at each optical operation: asymmetric split, reflect, and recombine. Without stabilizing the laser phase, at each laser pulsed operation, we introduce unknown laser phase onto the atoms' Bohr phase. As derived in equation

(2.6.8), the extra phases accumulate on top of the atom phase. Hence interference measurement for recoil frequency or gravity may yield incorrect result.

We need to be able to stabilize the phase so that those laser phases are eliminated altogether. Our strategy is to employ a feedback system to control the laser phase. We use an electro-optical system to stabilize the relative phase between the two beams. Further, we need to stabilize the beam quickly, within a few percent of the pulse time, so that the stabilization process does not affect the atomic wavefunctions. For example, if a pulse is 70 μs long, then we want to stabilize the phase to within a few μs. The required stabilization time, t_s, is calculated from considering our split fidelity from equation (2.4.8) with $\Pi = 0$ (hence $X = \beta$)

$$U = e^{i\frac{\Pi t}{2}} \begin{bmatrix} \cos\frac{\beta t_s}{2} & -i\sin\frac{\beta t_s}{2} \\ -i\sin\frac{\beta t_s}{2} & \cos\frac{\beta t_s}{2} \end{bmatrix} \qquad (3.0.1)$$

The concern is that while the phase stabilization apparatus is correcting the phase, we want to make sure that there is no significant effect on the wavefunction during stabilization period. Taking $\beta = 2\omega_r = 2\pi \times 7.5\,\text{kHz}$, we consider $\beta t_s \ll 1$ corresponding to $t \ll 20\,\mu s$. Under this condition, (3.0.1) becomes

$$\begin{bmatrix} 1 & -i\frac{\beta t_s}{2} \\ -i\frac{\beta t_s}{2} & 1 \end{bmatrix}. \qquad (3.0.2)$$

When (3.0.2) is applied to our initial state $\begin{bmatrix} 1 \\ 0 \end{bmatrix}$, we get $\begin{bmatrix} 1 \\ -i\dfrac{\beta t_s}{2} \end{bmatrix}$. Hence the population in

the moving state is $\dfrac{\beta^2 t_s^2}{4}$. If $t_s < 4\,\mu s$, then $\dfrac{1}{4}\left(\dfrac{4\,\mu s}{20\,\mu s}\right)^2 \sim 1\%$ so we will have, less than

1% unwanted population. So we want time $\dfrac{\beta t_s}{2}$ less than $4\,\mu s$. We operate at $3.6\,\mu s$.

Therefore, we require the phase locking apparatus bandwidth to be much greater than $1\,/\,3.6\,\mu s$, which is ~ 300 kHz. To ensure reliable locking, we need a bandwidth at least 10 times that, so 3 MHz or more. Hence the challenge of this experiment is in the instrumentation: the opto-electronics that can quickly stabilize the laser phase as we apply the optical manipulating pulse to the wave packets. We also demand the phase locking accuracy to within 10 mrad as this is the accuracy at which we can measure the interferometer output. We achieve these feats by employing an active electro-optical phase correction system. The system detects the relative phase of the laser beams, generates an error signal, and locks to the error signal to correct the phase of laser beams. So the challenge is finding a clever way to approach this issue with a simple solution.

This chapter describes our approach and is divided into three main parts. The first part explains the optical set up of the laser beams to extract the interference of the laser phase. The second part explains the electronic system used to import the laser phase information and generate the error signal to feedback to the electro-optical-modulator which can correct the phase via electro-to-optical phase conversion. The third part explains the design and construction of the amplifier system to drive the AOMs. All three parts constitute the main apparatus which allows the asymmetric splitting.
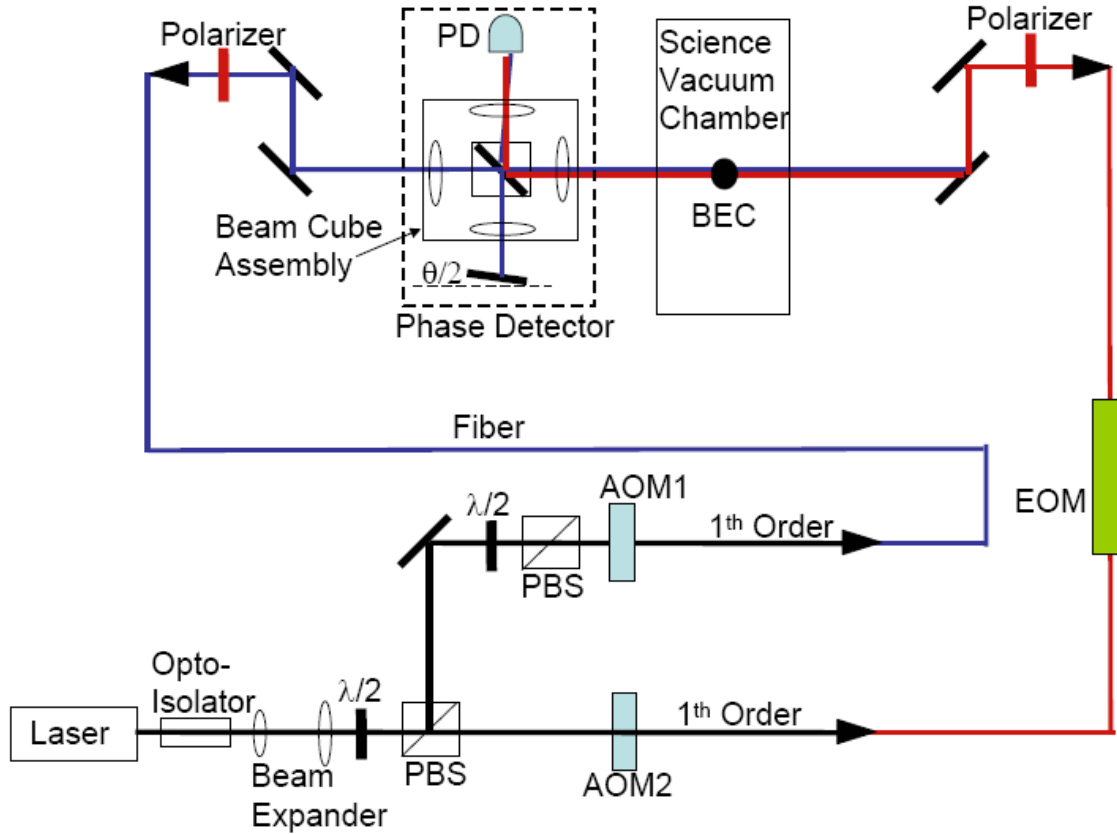
Fig. 3.1 Optical test bed for asymmetric splitting development. We use two acoustic-optical modulators (AOMs) followed by an electro-optical modulator (EOM). The beam cube allows interference of the two beams at the duel photo-detector (PD) where phase information is extracted. A single laser beam is split using polarizing beam splitter (PBS).

3.1 Optical Set-up

Figure 3.1 shows the basic schematic of the optical set up. The phase stabilization apparatus is a combination of electronics and optical systems working together in unison to provide laser phase stabilization. The optical component of the apparatus serves two purposes; 1) set up the laser beam alignment to split the atom packets, and 2) set up the laser beam geometry to extract the laser phase signal. The first is set up by having the two beams overlap on the atoms. The latter is set up using a Michelson-like interferometer configuration geometry to reveal spatial interference of laser phase with respect to each other. Our aim is to hold this spatial standing wave via electro-optical

feedback system to keep the differential phase to zero. Thus, we can implement a system where the relative laser phase that is stable and not changing.

As shown in Fig. 3.1 the laser is a 780 nm diode laser from New Focus TLM7000 with the output power up to 50mW. The laser beam is split into two using a half-waveplate and a polarizing beam splitter. The two beams are directed to two NEOS acoustic optical modulators (AOMs) (part #AOBD-461103LTD). The AOMs are devices which shift the frequency of the incoming laser beam via phonon-photon coupling. Simultaneously the AOMs also deflect the beams. In our set up, we use two AOMs with one AOM driven slightly higher frequency ($\Delta = 15\,\text{kHz}$) from the central $f = 100$ MHz. We also use the AOMs to turn the beams on and off like a shutter. In principle, the AOMs could be used to correct the laser phase, but in practice they are too slow for that purpose. It takes an AOM about 300 ns to transition signals from acoustic phonons to photons. This corresponds to a 500 kHz bandwidth, which is too slow for our purpose. Instead, we employ an electro-optical-modulator (EOM) from EOSpace (part # pm-0k5-00-pfu-pfu-780-ul-s) in-line with one of the laser beams. The EOM is used to change the phase of the laser beam proportional to an input voltage and has bandwidth of several hundred MHz. For the EOM we employ, the control voltage value at which the phase is shifted by π is called V_{π} and is measured to be 1.4V.

The laser beams from the two AOMs are coupled into optical fibers through THorlabs C220-TM-B achromat lenses with a focal length f = 11 mm. The EOM is also fiber coupled so that both beams can be delivered to the experiment via optical fibers in lieu of mirrors. Also, fiber coupling cleans the TEM modes of the laser beam, making the output beam very Gaussian. Another two sets of coupling lenses are on the outputs of

the fiber/EOM near the experiment. The measured output beam waist at $1/e^2$ is about 1

mm for both beams.

3.1.1 Phase Detection Concept
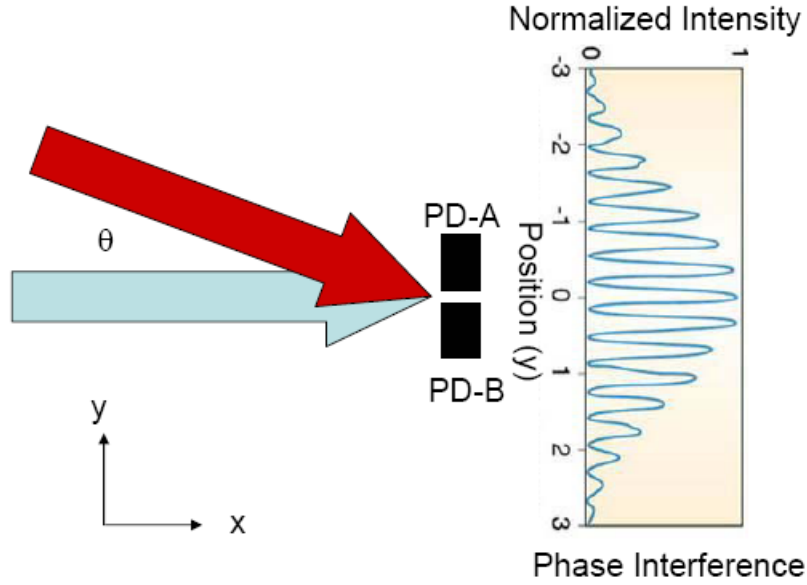
Fig. 3.2   Cartoon representation of interference signal at PD.

The phase difference between two laser beams can be approached in two different

ways. One way is to employ a heterodyne technique in temporal domain to detect the

phase by beating two frequencies of the laser. However, this technique is not fast enough

as ours is a 15kHz frequency which must be detected in a few microseconds. The second

way is instead of using the time domain detection, we use spatial interference signal and

obtain a "snap shot" of the phase signal to ascertain the phase information.   We use the

latter technique by using a fast photodetector (to be discussed in later sections) to detect

the interference signal created by the two beams at an angle as shown in Fig. 3.2. For the

situation in Fig. 3.2, the two laser beams have electric fields

$$\vec{E}_1 = E_1 e^{i(\vec{k}_1 \cdot \vec{r} - \omega_1 t)} \qquad (3.1.1.1)$$

$$\vec{E}_2 = E_2 e^{i(\vec{k}_2 \cdot \vec{r} - \omega_2 t)} \qquad (3.1.1.2)$$

where the wavevectors $\vec{k}_1 = k\hat{x}$, $\vec{k}_2 = k(\cos\theta \hat{x} - \sin\theta \hat{y})$, and $\vec{r} = x\hat{x} + y\hat{y}$. The detectors see an interference signal

$$I = E_1^2 + E_2^2 + 2E_1 E_2 e^{i(k + k\cos\theta x)} e^{-i(k\sin\theta y)} e^{-i(\omega_1 + \omega_2)t} \qquad (3.1.1.3)$$

which depends on the angle between the beams and the frequency difference of the laser beams. Hence the detector sees a spatial variance signal proportional to the phase of the laser beams. We can achieve the spatial phase detection through the following way: as shown in Fig. 3.1 the two beams are aligned counter propagating and overlapping the atoms. On the same path, on the left side of the atoms in Fig. 3.1, the beams also enter a phase detecting beam cube assembly. The beam cube assembly is composed of 30R/70T beam splitter cube with a mirror and a photodiode (PD) on 2D translation stage on cage mount system. The purpose of this beam cube assembly is to simply set up the beam path geometry to acquire interference signal of phase between the two laser beams. At the end, the Hammamatsu S4202 dual PD is used to resolve spatial standing wave parallel to the detectors as shown in Fig. 3.2.

The Hammamatsu dual PD is 1×2 mm two square element array with 0.02 mm gap between the photodetector A (PD-A) and photodetector B (PD-B). The distance between the anti-nodes of the standing wave is $D = \lambda / \theta$. The dual PD have a spacing of 2 mm, so by setting D = 4 mm (θ= 0.2 mrad), difference between the signals detected by PD-A and PD-B indicates the laser interference phase.

3.1.2 Phase Detection Implementation

The angle θ is achieved between the two beams to the detector using a mirror situated perpendicular to the beams incoming path to the beam cube in the cage mount assembly. The beam cube has only one reflective surface diagonal to the cube so our beam "A" will reflect once to PD while the other beam "B" will reflect, then bounce off mirror on the opposite side of the PD, and then finally arrive at the PD through passing the beam cube one more time. Simultaneously, this same beam will allocate most of its first split beam (70% transmit) towards the atoms. A beam power balancing is a juggling act in this configuration. We want about equal amount of intensities to overlap the atoms as well as having an equal amount of intensities from both beams hitting the PD. We adjust the input intensities of the two beams by a series of half-wave plate adjustments at the AOM side of the optical set up.

Although the cage mount system worked well to acquire the interference signal of laser phase, we decided to surround the beam cube with four singlet lenses ($f = 35$ mm) mounted on Thorlabs CM1-4ER cage mount. The purpose of the four lenses spatially at 35 mm from the center of beam cube on all four sides can be explained by examining Fig. 3.3. The beam "A" (color red) is focused at the center of the beam cube and then reflected towards the PD as it focuses out. As the beam is reflected/transmitted and is expanded, the second focusing lens re-creates the beam diameter of the original beam hence no change is realized for beam "A" as it exits the second lens. For laser beam "B" (color blue) the beam incident on lens is focused, reflected to another lens at 35 mm away, and when it exits the lens, it is likewise, re-formed with same diameter beam. However, the mirror with deflection angle $\theta / 2$ will reflect the beam off-axis so that when the

beam enters the focusing lens again from the back side, the beam does not focus at the center of the cube but rather at an off-axis as shown. As the beam passes through the final lens before hitting the PD, the beam is directed to the PD with an angle θ which results in an overlap with the laser beam "A." What we achieve by creating such complex web of lens is that it makes the alignment simpler and easier. Regardless of the angle of the reflecting mirror, the beam will always find a path back to the PD. Hence, we can control the interference angle θ without affecting the over-all beam paths. Also, we want to put the whole assembly on a vibration-free stage eventually so we want to make all components compact hence minimal adjustment is required to resolve the phase interference.

In the beam cube assembly, we use a cube beam splitter instead of a plate beam splitter. Use of a cube beam splitter is important, as compared to a plate splitter, since a plate beam splitter can introduce aberrations to the beams through a multiple passing of the beam splitting side. We are not able to resolve a good beat note with plate beam splitter as one of the beam going into the PD was elongated horizontally, reducing the visibility of the beat note. This aberrations is significantly reduced with the use of cube beam splitter.

Unlike the previous symmetric splitting experiment where the most important reflecting mirror is set up on a vibration controlling stage, we will put the beam cube assembly in lieu of that mirror. The main purpose is to make it one piece on a standard 1 inch mount. For this experiment, we did not use an isolation stage.
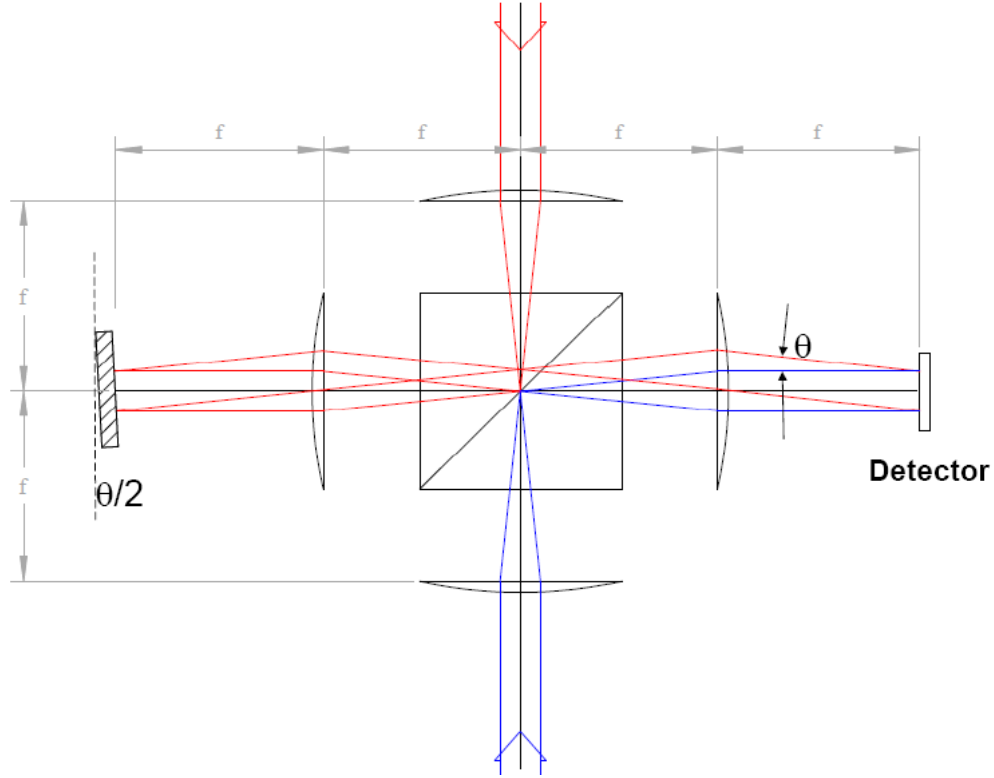
Fig. 3.3 Schematic showing the beam cube assembly. The beam splitter is 30R/70T which allows maximum beam to the atoms and enough beam power to be directed to duel PD where the phase information is extracted. The four surrounding focusing lens allows change of θ without changing the direction of the collimated beam onto PD.

3.1.3 Phase Detection Performance

Obtaining the interference at the PD is another balancing act that must be understood. As laser beams A and B arrive at the PD with B at beam angle θ with respect to the beam A, we obtain interference. As we vary the angle between the two beams, we can adjust the phase interference offset as detected by the PD.

We want to adjust the angle θ so that the transverse period of the spatial interference signal is nominally twice the photodiode spacing, as shown in Fig. 3.4. In this configuration, the difference between the two photodiode signals is maximally

sensitive to the phase of the interference. The intensity as a function of position can be expressed using Eq. (3.1.1.3) as

$$I \propto 1 + \cos\left[(1 - \cos\theta)kx + ky\sin\theta + (\omega_2 - \omega_1)t\right], \qquad (3.1.3.1)$$

which for small θ reduces to

$$I \propto 1 + \cos(k\theta y + \phi) \qquad (3.1.3.2)$$

where $\phi = (\omega_2 - \omega_1)t + \phi_i$. By sampling this function at half its period in y, we can determine ϕ as desired.
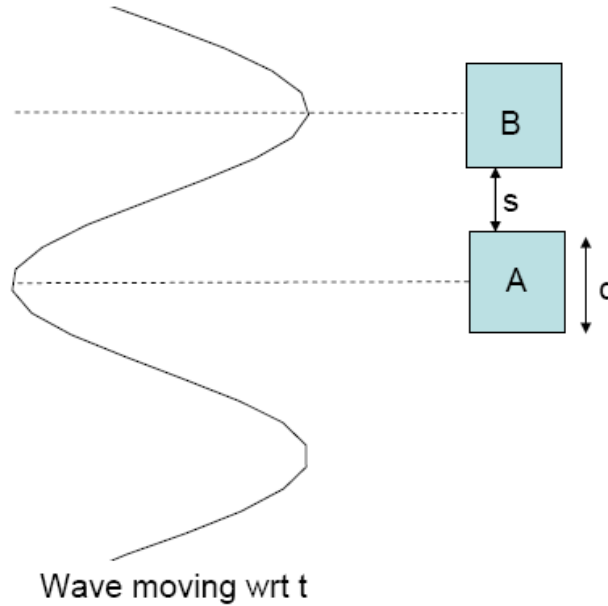

Wave moving wrt t

Fig. 3.4 Dual PD with width d and separation distance s. As the phase from the two beams is moving with respect to time, the detectors see two different spatial intensities. Subtracting the two signals yield spatial phase information.

In practice, the photodiode elements have width d and separation s as shown. The signal produced by one PD is therefore

$$S_1 = \int_0^d I\,dz \propto \int_0^d 1 + \cos(k\theta y + \phi)\,dy \qquad (3.1.3.3)$$

Evaluating the integral we get

$$S_1 \propto d + \frac{1}{k\theta}\left[\sin(k\theta d + \phi) - \sin\phi\right] \qquad (3.1.3.4)$$

The signal from the second photodiode will be

$$S_2 = \int_{s+d}^{s+2d} I\,dz \propto d + \frac{1}{k\theta}\sin\left[k\theta(s+2d) + \phi\right] - \frac{1}{k\theta}\sin\left[k\theta(s+d) + \phi\right]. \qquad (3.1.3.5)$$

For the ideal spacing $k\theta(s+d) = \pi$ the difference signal is

$$S_1 - S_2 = \frac{2}{k\theta}\left[\sin(k\theta d + \phi) - \sin\phi\right] = \frac{4}{k\theta}\sin\left(\frac{k\theta d}{2}\right)\cos\left(\phi + \frac{k\theta d}{2}\right). \qquad (3.1.3.6)$$

Our photodiodes had s = 0.99 mm and d = 0.02mm, so the nominal angle was $\theta = 0.07$

degrees.

Hence the visibility oscillates so we want to maximize the visibility by adjusting

θ to detect the maximum visibility. Originally, we intended to offset the phase

difference to be 180 degrees which we thought would give us the maximum contrast.

However, upon practice and theoretical investigation (3.1.3), 90 degrees phase worked

best for us. This is because the intensity is attenuated at 180 degrees so that the

difference is better at 90 degrees as compared to 180 degrees. To illustrate such

examples, the phase differences are shown in Fig. 3.4. For our phase locking system to

work, the phase is relative and we are not stringently set for 180 degrees. We prefer

having a higher contrast between the two beams so that our electronics (to be discussed

next section), have enough voltage to work with. Therefore, we choose 90 degrees as our

set phase. If desired, any phase offset that yields maximum contrast will work well as long as enough voltage is acquired.
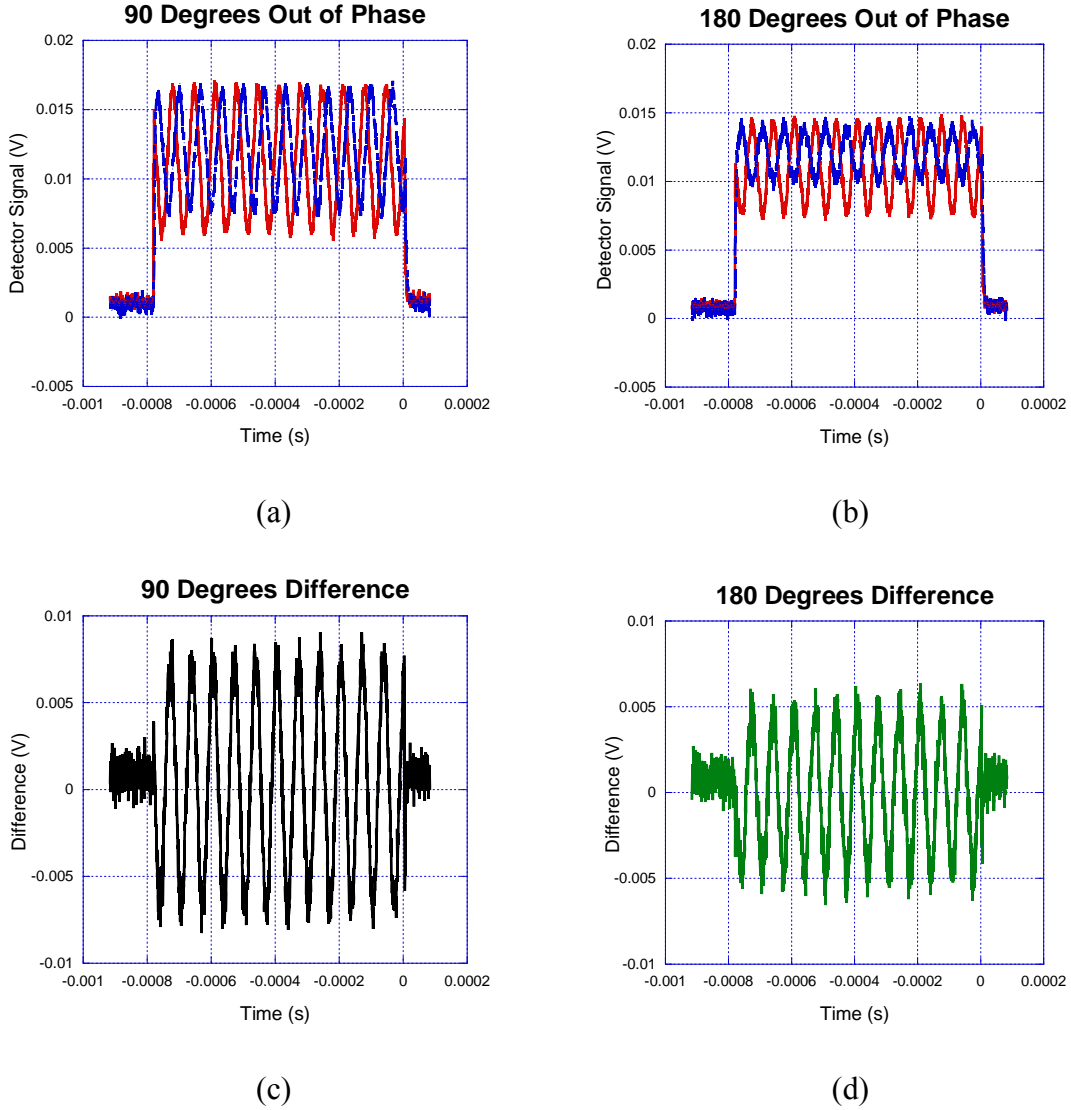

Fig. 3.4. Shows (a) phase difference of 90 degrees of laser beams, (b) phase difference of 180 degrees, (c) difference of signals in (a), (d) difference of signals in (b).

3.2 Electronic Phase Feed-back System

The result of the optical component of the experiment is to attain the phase information in terms of the voltage signal. We can now devise a complementing active

electronic feedback system that can correct the laser phase offset to zero in 10 MHz bandwidth. The electronics system, as shown in Fig. 3.5 is a series of sub-components that can subtract the PD signal, generate error signal based on a PI feedback circuit, and sample and hold the error signal to ultimately provide feedback to the EOM to stabilize the phase. During the process, amplifications and attenuation are an essential part of the circuit.
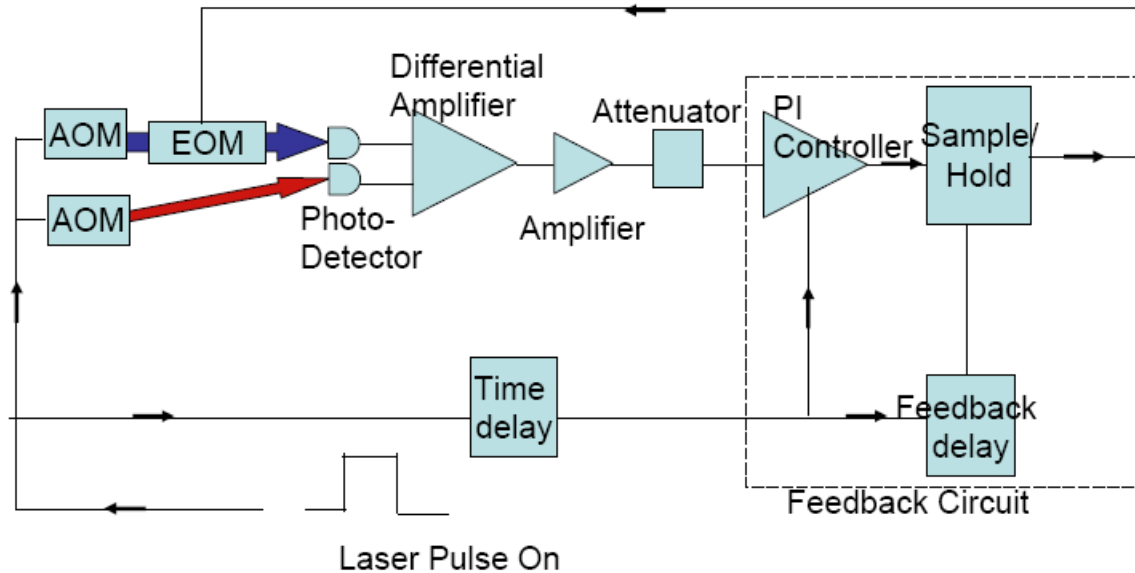
Figure 3.5. Block diagram for all electronics. Starting from two laser beams feedback to EOM is generated as a final product of the electronics.

The utmost importance in designing an electronic feedback system is the bandwidth. How fast should we make our circuit to operate? Clearly we want bandwidth greater than 3 MHz. To comfortably rely on good practice, we aim for bandwidth in the 10 MHz range (equation 3.0.2). Without focusing too much on going above 10 MHz which would require some selective rf components which are exorbitant in cost, we find cost effective balance by building a circuit with bandwidth of 10 MHz with a reasonable cost. We describe the electronics development in the next sections.

3.2.1 Photodetector

The photo-diode pair (PD) is a Hammamatsu S4202 as shown in Fig. 3.6 which is a dual-element Silicon P-I-N photodiode with nominal 30 MHz bandwidth. We find 0.25 A/W efficiency. A simple circuit diagram of the PD unit is shown in Fig. 3.7. It is simply a 12 V biased circuit with output current converted with a 50 Ω resistor for a fast response.
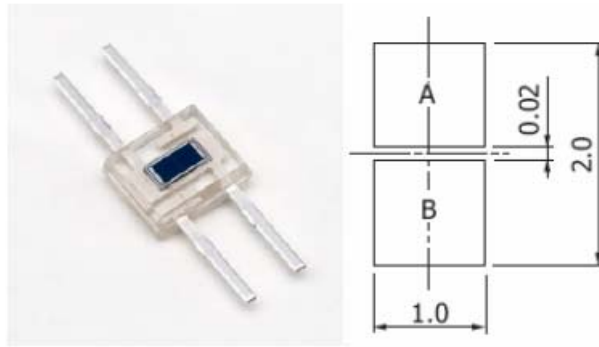
Fig 3.6. Hammamatsu S4202 dual photodetector with dimensions (in mm).

For higher gain, 100 Ω resistors can be used instead. The whole PD assembly is fit inside the one-inch optical barrel mount on a 2D translation stage with micrometer mounted to the stage to accurately position the PD to obtain the laser phase interference signal.
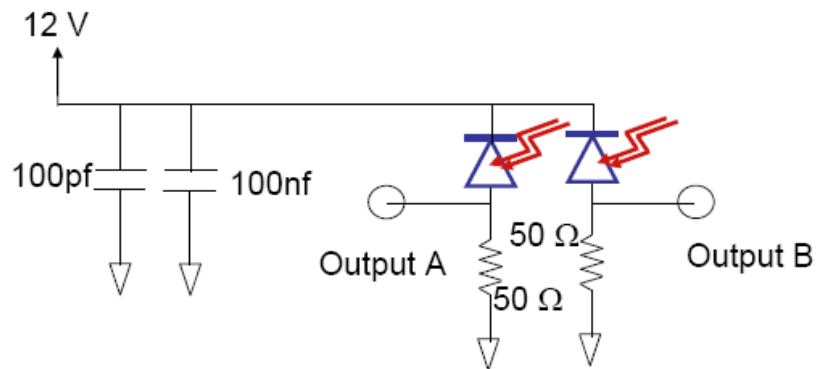
Figure 3.7 Schematic of PD Circuit. We bias the PD using existing 12V and convert current to voltage via 50 Ω resistors.

For our purpose, the frequency response of the electronics component is the most important as our system must operate quickly to stabilize the phase. Hence, we measure frequency response of the PD to ensure that our desired 10 MHz bandwidth is achieved. For testing purpose, we set up a simple interferometer as shown in Fig. 3.8, modulating only one of the beams with the EOM.
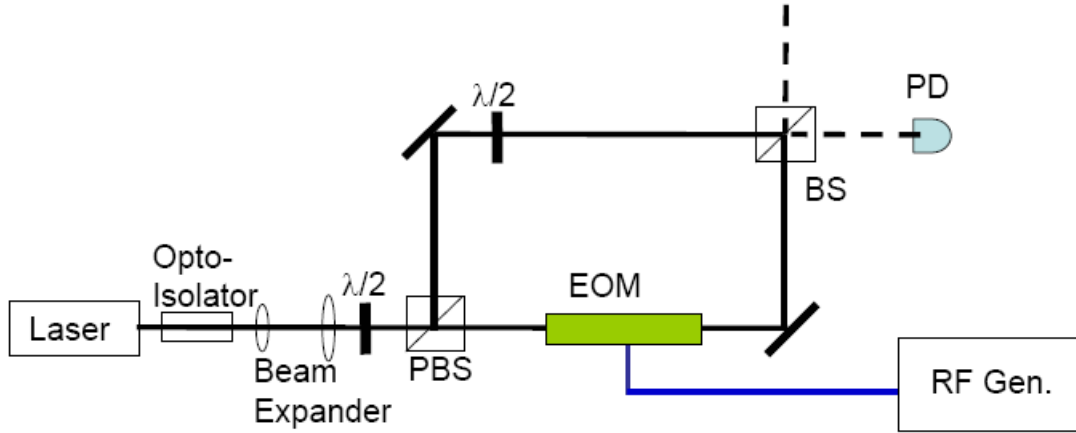
Fig. 3.8. Optical testing of PD as function of frequency.

(a)   (b)

Figure 3.9 Bode plot of photodiode response. (a) shows amplitude gain as function of frequency, (b) shows phase as function of frequency. 50 Ω resistor is used for this measurement.

By varying the modulating frequencies to the EOM with a rf function generator, we spot check at several frequencies up to 30MHz. This is a direct optical modulation measurement. The Bode plot is shown in Fig. 3.9. We find that gain is 40 dBm at 1MHz to 38.5 dBm at 10 MHz while phase lag is zero until after 5 MHz and then quickly lags about 50 degrees at 10MHz.

3.2.2 Differential Amplifier

The output of the dual element PD feeds to an Analog Devices AD8138 differential amplifier (DA) which subtracts the PD-A input from the PD-B input. The AD8138 chip is mounted on an evaluation board EVAL-8138 with a fixed relative gain 0.75 for each output channel. The schematic of the unit is shown in Fig. 3.10 with its component values. It should be noted that there are two outputs from the differential amplifier but only one output is used for electronics following after. For example, we use Output A to feed into the amplifier, and use Output B to monitor the signal with an oscilloscope to verify that we have a good differential signal from PD-A and PD-B during the actual experiment.
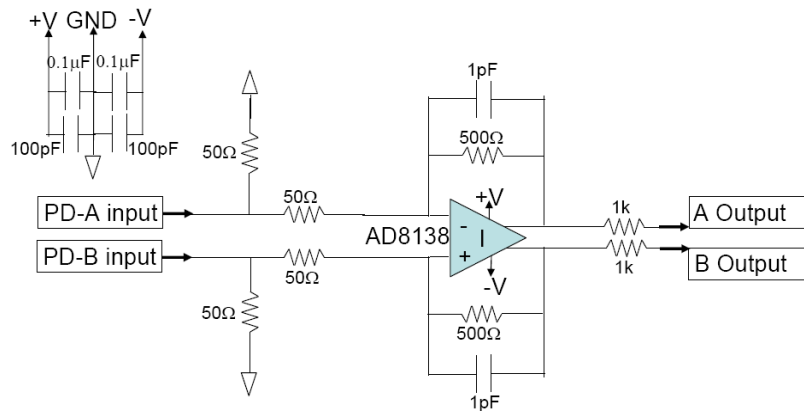
Fig. 3.10 The schematic for differential amplifier. Two inputs from PD are differentially subtracted. Two outputs show two different polarity subtractions.
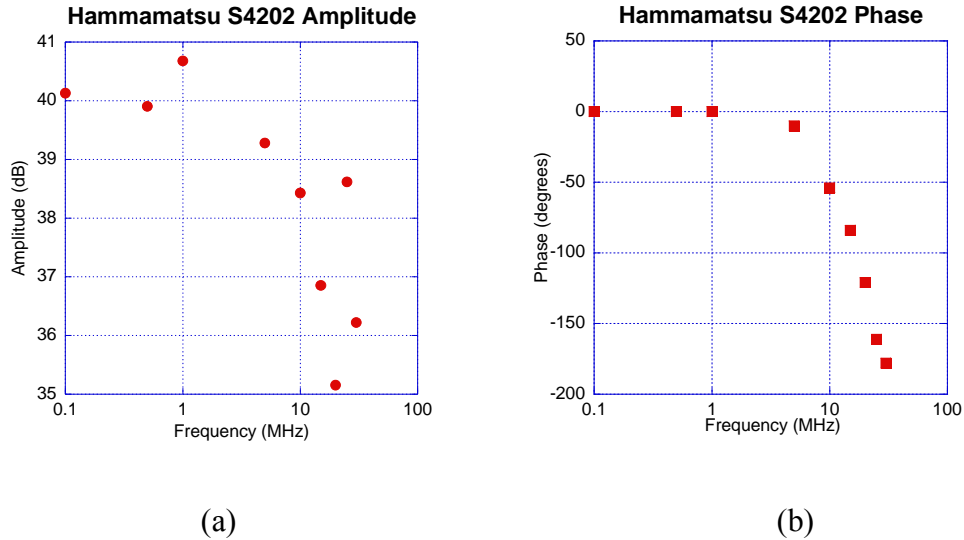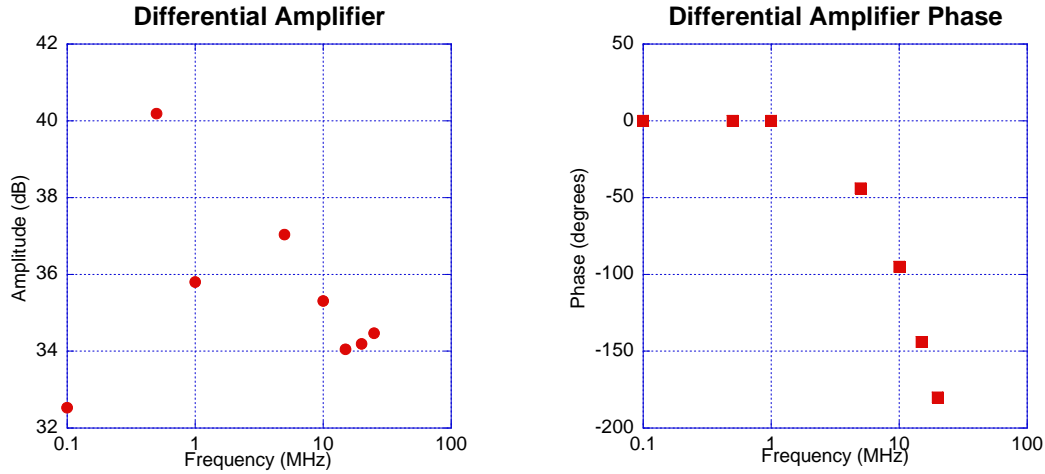
Figure 3.11 BODE plot of differential amplifier. (a) shows amplitude gain as function of frequency, (b) shows phase as function of frequency.

We test the frequency response of the circuit by directly feeding in an rf signal to the input of the differential amplifier and observing the output. This gives the Bode plot as shown in Fig. 3.11. As seen, the phase lag is 45 degrees at 5 MHz.

3.2.3 Amplifier

We need gain to amplify the voltage to generate the error signal. We do this by using a dc coupled high speed amplifier. The amplifier is a fixed gain amplifier commercially available at RF Inc. part number DCA-50-23. We also measure the frequency response as shown in Fig. 3.12. The amplifier yields very good gain and phase frequency response at 10MHz. The gain is fairly constant at about 24 dBm until 10 MHz and phase is delayed only by 20 degrees at the same frequency.

The output from the amplifier contains the relative phase information of the two PD signals. In reality, for a nominal input of two beams of 2 mW each making the fringe

pattern on the photo-detector, after the differential amplifier and amplifier, we measure about 375 mV of signal output at 0 degrees phase.
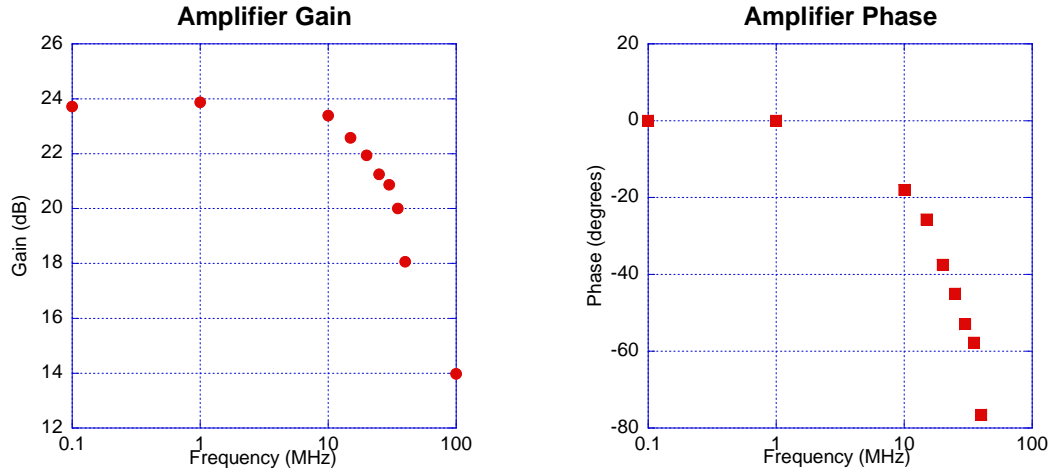
Figure 3.12 Bode plot of amplifier. (a) shows amplitude gain as function of frequency, (b) shows phase as function of frequency.

3.2.3.1 Overall Gain & Phase

We measure the overall gain and phase lagging of all components in series: PD, differential amplifier, and amplifier. For this test, the input is an optical laser beam on PD and the EOM is modulated with an rf function generator. We find that our operating range is close to 10MHz. This suggests that our locking circuit can successfully lock in the few μs range.

The overall gain and phase is not entirely consistent with that of the individual components. The reason for this is not clear, but it likely has to do with the effect of electrical loading between the subsystems. When all systems are connected, it must change the impedance load of the system.
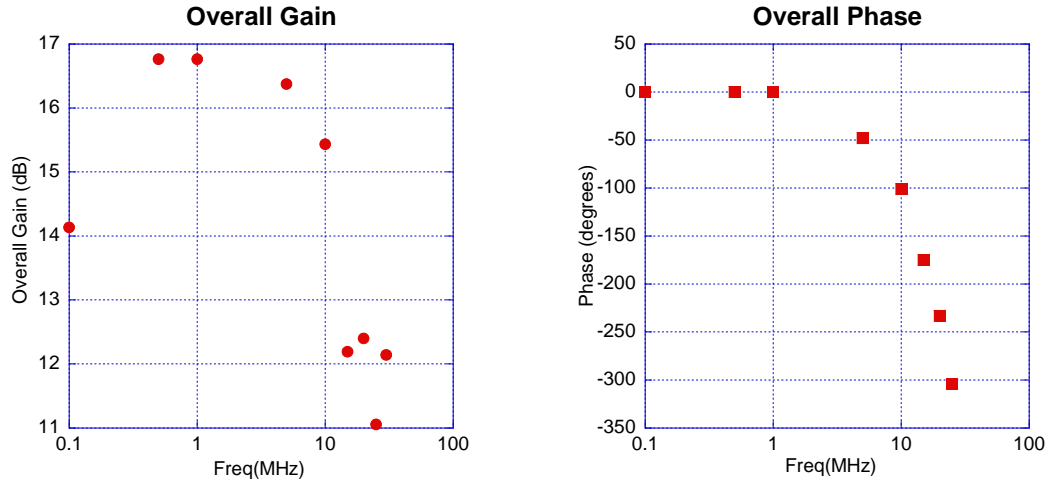
Figure 3.13 Bode plot of overall gain and phase. (a) shows amplitude gain as function of frequency, (b) shows phase as function of frequency.

3.2.4 Attenuation

In order to provide an adjustable gain in the feedback circuit, we pass the error signal through a voltage controlled attenuator. This is done through a simple circuit shown in Fig. 3.14. It is a high speed attenuator which can be accomplished via a fast transistor and a fast op-amp. The field effect transistor (FET) acts like a variable resistor, controlled by the attenuation voltage, which controls the amplitude of the signal going to the buffer op-amp. The attenuation is variable hence we can adjust the error signal level as needed by the feedback circuit. The attenuation is adjusted through a one-turn potentiometer on the front panel. We set the attenuation level empirically by optimizing the lock behavior.
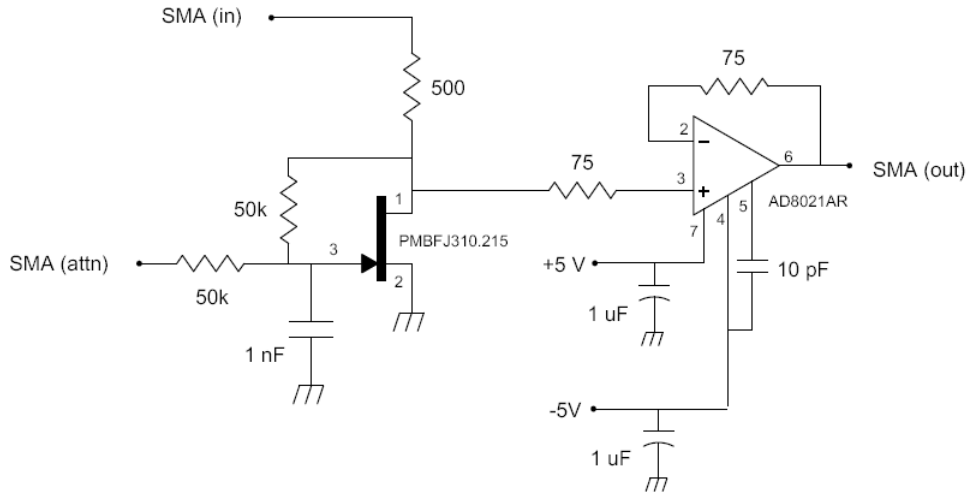
Figure 3.14 Schematic of attenuate circuit. SMA (In) is the differential signal in through the SMA port, SMA (out) is the attenuated signal out, and SMA (attn) is the control voltage applied to adjust the gain. We use this circuit to attenuate the error signal going into the lock circuit.

3.2.5 Proportional and Integrate Circuit

We need to generate error signal to feed back to EOM to stabilize the phase. There are several widely known error signal generating mechanisms such as proportional-integral-derivative (PID) controller that can generate the feedback signal to correct for the error from a set point of our desired value [22]. In our system, we use a proportional-integral control circuit. We omit the derivative portion of the circuit as we anticipate that our system does not need it. The basic idea of the error generating circuit is equivalent to a thermostat in a house. The thermostat keeps the house at a certain temperature by subtracting the measured temperature of the house from a set point (i.e. 70 degrees Fahrenheit). If there is any deviation from the set point, either an air conditioning or a heater will be applied to regain the set temperature. For our system, the differential phase of the laser beams is like the temperature and we would like to set this to zero.

Mathematically, the error signal generation for the PI is,

$$u(t) = K_p e(t) + K_i \int_0^t e(\tau) d\tau \tag{3.2.5.1}$$

where K_p is the proportional gain, K_i is the integral gain, t is time, and $e(t)$ is the error

signal, defined as the difference between the current value and the set point value. For

detailed analysis of the PI control theory there are plethora of control theory books and

on-line [23].
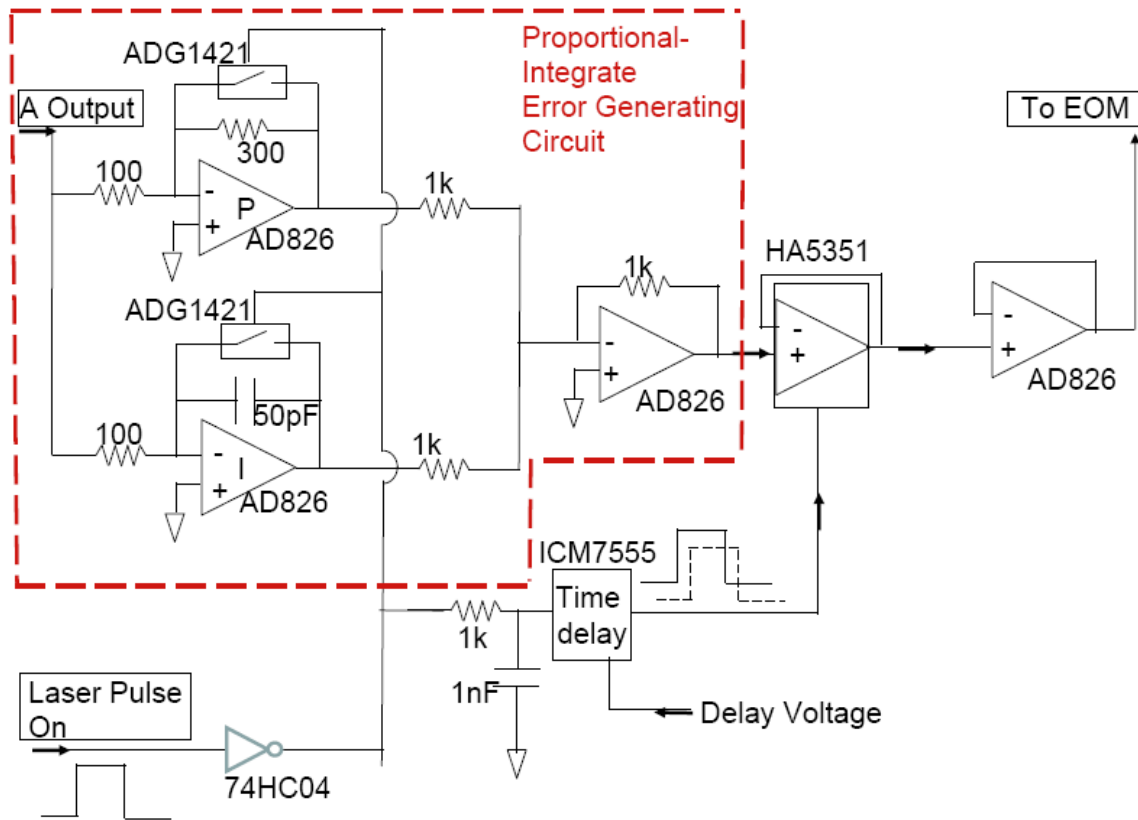
Figure 3.16 Schematic diagram for S/H Circuit. The circuit is combination of proportion and integrate error signal circuit followed by a sample and hold circuit. Switching the locking on and off and time delay is also needed to lock the phase when needed. Time delay is adjustable at the front panel by a turning knob potentiometer.

A part of our PI circuit is shown in Fig. 3.16 enclosed by red dashed lines. The

proportional component is an operational-amplifier AD826 labeled "P" with gain of $K_p =$

3 set by the resistors combination ($300\,\Omega$ and $100\,\Omega$). The integrate is an identical operational-amplifier labeled "I" with resistor and a capacitor with $K_i = 1/RC = 1/(100\,\Omega \cdot 50\,\mathrm{pF}) = 2.0 \times 10^8 \, s^{-1}$. The proportional and integral signals are equal at a signal frequency $\dfrac{K_i}{K_p} = 2\pi \times 10 \, \mathrm{MHz}$. The two op-amps are equipped with ADG1421 switch on the feedback loop which can toggle on/off error generating circuits by an external TTL signal. When the switch is off, the error signals from the proportional and integrate are added at a third op-amp and is fed into the HA5351 Sample & Hold chip.

3.2.6 Sample and Hold Circuit

The PI circuit is followed by the sample and hold chip, HA5351. A brief circuit diagram is shown in Fig. 3.16. The sample and hold circuit's main task is to sample the incoming signal, which is the feedback signal from the PI, and store its value for some length of time until the input is sampled again. Electronically, when the S/H is in a sample state, the error voltage at the input appears at the output and varies simultaneously. When the control is changed to hold mode, the last sampled error signal voltage is held inside the chip and its output is a constant value of this voltage. For phase locking, the main purpose of the S/H circuit is to correct the phase of one beam respect to another to zero at the start of the asymmetric splitting only for a very short time ($\sim 3.6\,\mu s$) so that the beams' phase do not contribute to the overall phase gained by the atoms during the actual interferometer experiment. After the initial $3.6\,\mu s$, the phase of the pulsed beam must be allowed to develop as $\phi = \Delta t$, in order for the asymmetric splitting to occur. At

this point, the phase locking circuit must be inactive. Hence, the chip "sample and hold" is in fact "track and then hold." Of course, the sample and hold gets its error signal from the PI circuit which determines the amount of error correction needed to stabilize the phase. The control signal is generated from the laser on/off signal by adding a 3.6 μs delay using the ICM 7555 chip . We can adjust how long we want to keep the S/H on sample mode by changing the automatic set delay time via a 10-turn potentiometer.

The actual circuit is designed using Eagle CAD software. The two-layer board (top and bottom) is a surface mount component design and is sent to a manufacturer to get fabricated and its board layout is included in the Appendix A

3.2.7 Control Timing

It is worth going over some details on the timing signals. Our electronics are built for a fast operation ~ 10MHz. Hence some aspects of the timing control needs clarification to design and operate our locking circuit properly. Recall that our atom manipulation is done by pulsed laser beams of tens to hundreds of micro-seconds duration. We want the following events to occur in sequence to lock the phase successfully as shown in Fig. 3.17.

First, the "laser pulse-on" TTL signal turns on the AOM applying the light to both the atoms and the lock system. It takes about $1.8\,\mu s$ for the laser to fully fire on. This is done through an initial delay which is explained in detail in Appendix B. Immediately after the $1.8\,\mu s$ delay, we activate the PI circuit so that the error signal is generated. At the same time, the sample and hold is in sample mode hence the output of the chip follows the feedback signal generated by the PI and adjusts the EOM to stabilize the

phase. After a 3.6 μs delay from the original laser pulse-on TTL, the sample & hold chip

is switched to the hold state. The feedback signal on the EOM is then held at a constant

voltage. This is when we allow the laser phase develop for the asymmetric splitting

process. When the laser pulse-on TTL goes low, the AOMs and the laser beams turn off.

The circuit returns to the initial state which is: PI-off, sample & hold – sample (but has no

signal), and the time delay – low.
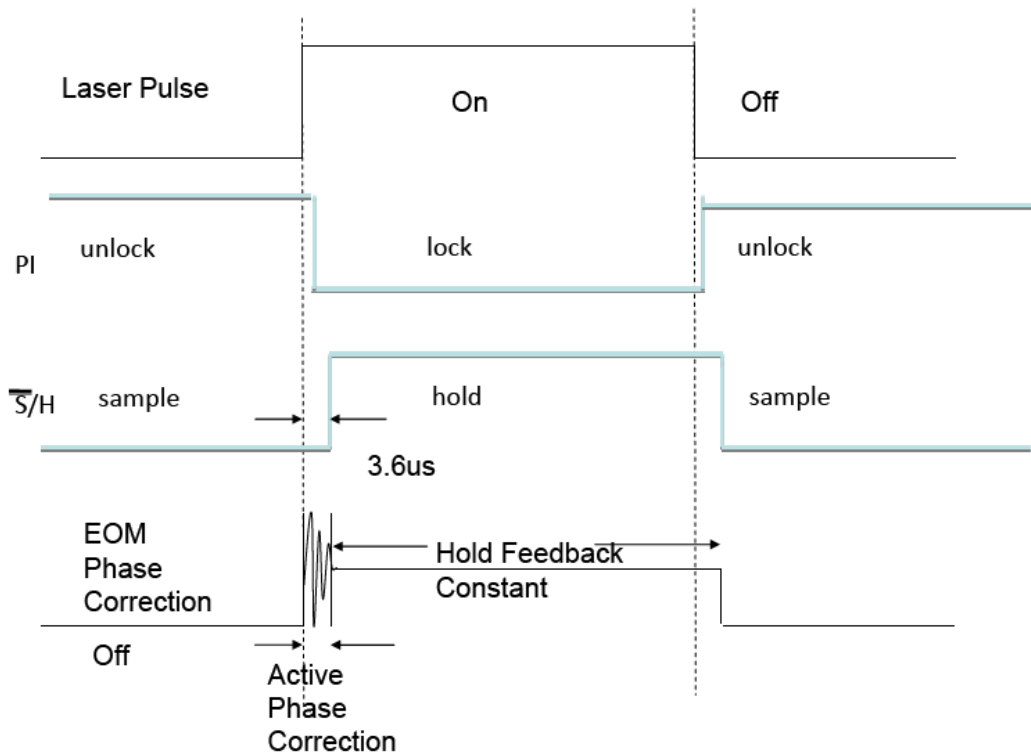
Fig. 3.17. Shows the timing sequence of relevant component of the lock circuit. Initial
1.8 μs delay from a delayer is not drawn as it shifts all timing by 1.8 μs. Active phase
correction of EOM is set for 3.6 μs.

3.3   AOM Driver

A second part of the electronics deals with an in-house built AOM drivers to

accurately generate two frequencies - $2\pi \times 100\,\mathrm{MHz}$ and $2\pi \times 100.015\,\mathrm{MHz}$ – and be able

to provide enough rf power to drive the AOMs. We implement the driver system by

using a single master rf frequency generator with $\omega = 2\pi \times 100\,\text{MHz}$, splitting the master rf signal into two signals - A_{rf} and B_{rf}, but mixing A_{rf} with $\Delta = 0.015\,\text{MHz}$ with IQ modulator via multiplexer. The two rf signals then go through power amplifiers which can drive AOMs. Remember that the offset frequency, $\Delta = 2\pi \times 0.015\,\text{MHz}$, is set by the frequency that is needed to drive the atoms from $0\hbar k$ to $+2\hbar k$ which was discussed in the theory chapter.

The overall schematic of the driver is shown in Fig. 3.18. Briefly, the AOM drivers consist of a single master oscillator generating the 100 MHz frequency followed by a splitter in which one signal is fed into IQ modulator while the other input goes to power amplifier through an attenuator. The IQ modulator mixes the 100 MHz with a small 15 kHz signal and outputs to another power amplifier via an attenuator. There are two AOMs in the experiment, driving AOM1 with $\omega + \Delta$ and AOM2 with ω where $\omega = 2\pi \times 100\,\text{MHz}$ and $\Delta = 2\pi \times 0.015\,\text{MHz}$. This section describes how we generate those frequencies.

We need two phase coherent sources with exactly Δ difference. Independent oscillators will generally not provide this as exactly tuning both oscillators with precision is very difficult with simple commercially available products. Fortunately, there are two different ways we can implement the frequency generation. One way is using two oscillators and locking the frequency. Or alternatively, drive both frequencies from a single oscillator. Either could work, but we chose the latter. We therefore had to implement frequency mixing component to the circuit with an IQ modulator.
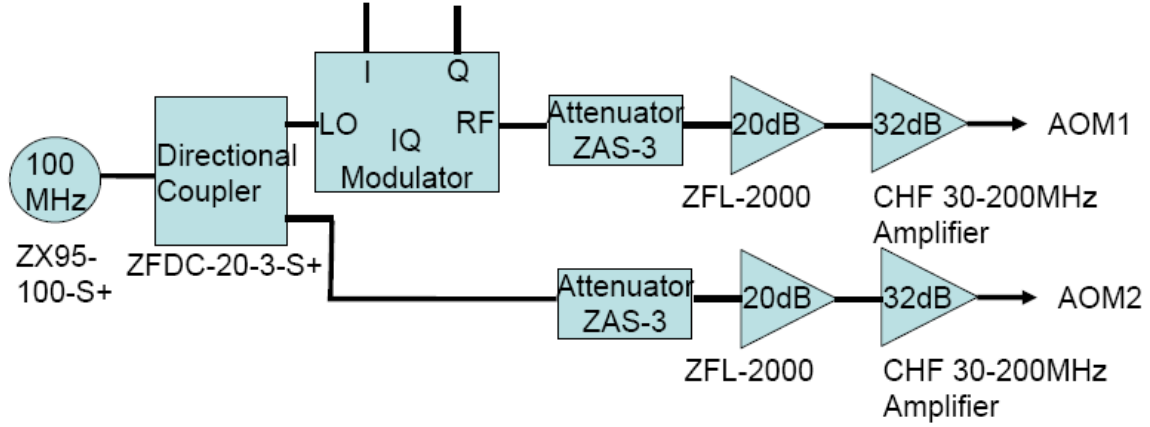
Figure 3.18. Block diagram for IQ modulator and amplifier circuit. The main frequency, 100 MHz is mixed with 15 kHz at the IQ modulator and drives AOM1 where as the second amplifier drives AOM2 with just the main frequency.

3.3.1 IQ Modulator

The main purpose of the IQ modulator is to impose a phase-controlled frequency shift to the master oscillator. Since we are only using one master oscillator using the IQ modulator can shift the frequency as desired for the laser beams. Using only one master oscillator, the latter is easily achieved by simply driving the AOM with the master oscillation. However, A_{rf} will need an IQ modulator to mix two signals to give $\omega + \Delta$.

The IQ modulator works by mixing the input signal with a combination of $I = \cos(\Delta t)$, and $Q = -\sin(\Delta t)$. Its operation schematic is shown in Fig. 3.19.

Recall that a signal can be characterized by its complex amplitude, so the real voltage $v(t)$ is

$$v(t) = \text{Re}\{V(t)\} \tag{3.3.1.1}$$

where $V(t) = Ae^{i\omega t}$ for the oscillation frequency ω and a complex amplitude A. With an IQ modulator, the Local Oscillator (LO) input, $\omega = \omega_0$, is a fixed carrier
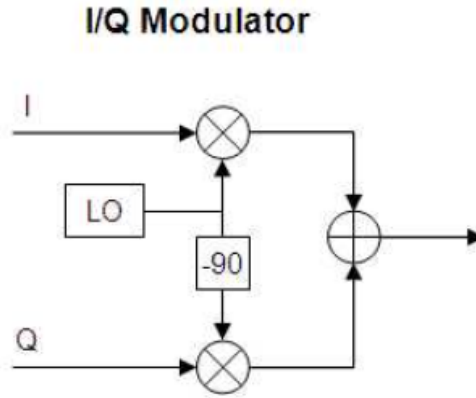
I/Q Modulator

Fig. 3.19. IQ modulator operation schematic. LO is local oscillator, -90 represents 90 degrees out of phase, and I and Q are mixing inputs to the modulator.

$LO = A_0 e^{i\omega_0 t}$. The modulator outputs the signal $RF = A_1 e^{i\omega_0 t}[I(t) + iQ(t)]$. Hence if we make $I(t) = M\cos(\Delta t)$ and $Q(t) = M\sin(\Delta t)$, the output is simply

$$RF = A_1 M e^{[i(\omega_0 + \Delta)t]} \tag{3.3.1.2}$$

The expression in equation (3.3.1.2) is a signal oscillating at $\omega_0 + \Delta$ that is phase coherent with the original LO input.

We use one master oscillator (mini-Circuits ZX95-100-S+) and split the signal into two channels using a directional coupler, ZFDC-20-3-S+. One of the outputs is fed into the LO of the IQ modulator while the other side goes to a ZAS-3 attenuator. The ZAS-3 attenuator is used to attenuate the rf power going into the AOM amplifier (Wideband CHF 30-200 MHz RF power amplifier) which is a commercial unit with maximum output power of 1.5 W. For the IQ side, the ω input at LO is mixed with (I+iQ) at the modulator and output is sent to "RF" as shown in Fig. 3.18. Again, the signal can be attenuated using a ZAS-3 before going into the power amplifier.

3.3.2 Power Amplifier

To drive the AOMs there is not enough power from the master oscillator. We will need to employ two rf amplifiers to drive the AOMs. In our experiment, the NEOS AOMs require 2W (33 dBm) of power according to the manufacturer. Upon measuring the NEOS driver, we find that power is actually 1.5 W (32 dBm). Hence, we want to acquire a commercially available amplifier with at least 1.5 W (32 dBm) to drive the AOMs. We purchased two "wideband VHF 30-200MHZ RF power amplifier" from seller bg7cr on ebay.

We tested the amplifiers and found the minimum input power to be 0.5 mW (-3 dBm) to 1mW (0 dBm). Anything less than 0.5 mW reduced the output power significantly. The maximum output of the amplifier is 1.5 W (32 dBm). The amplifier is powered by about 0.3 amps at 12 V (DC).

We have the flexibility to control the power output of the amplifier. This is needed in order to attenuate the power of the laser beam during the experiment to change laser beam parameters such as β. Although we used full maximum power for each pulses in this study, for future experiments, we want to be able to vary the intensity of the beams eventually. Therefore, we measure the relative optical power as a function of attenuation control voltage of ZAS-3. If desired, this result is used to calculate the correct β. The normalized power is shown in Fig. 3.20.
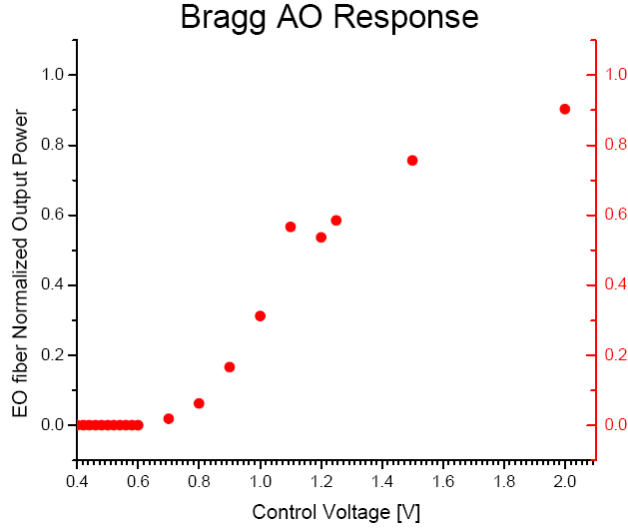
Figure 3.20. Response of AOM power as a function of ZAS-3 input voltage. We planned on using attenuated signal of this but ended up using the full power (5V).

3.3.3 Multiplexer

The split, reflect, and recombine pulses require different frequency components. We generate these by providing different frequency signals to the IQ modulator through a multiplexer. We manipulate the outputs of the multiplexer via control digital bits. The multiplexer has four inputs: 15 kHz, 15 kHz (90 degrees out of phase), Ground, and DC offset. The DC offset signal allows us to set both laser beams to the same frequency for symmetric operations. We did not use the DC input for experiments discussed here. The 15 kHz input from the function generator is shifted 90 degrees by a phase shifter circuit. The original 15 kHz signal and the 90 phase shifted signal both go into two multiplexers but in a swapped pin configuration as shown in Fig. 3.21.

The output, labeled "D" in Fig. 3.21, of the multiplexer is chosen by the control bits labeled "A" and "B." The control bits are two-bit binary which give 4 possible output configurations. Each output goes to a buffer, the two signals then goes to the inputs of the IQ modulator and mixed with LO which is ω_0 from a master oscillator

previously described. At the end, we get the output to the AOM1 driver with the following output with control bits:

Function	C1	C2	I	Q	Frequency1
Split	0	0	$\cos(\Delta t)$	$\sin(\Delta t)$	$\omega_0 + \Delta$
Reflect	0	1	$\cos(\Delta t)$	0	$\omega_0 + \Delta$, $\omega_0 - \Delta$
Recombine	1	0	$\cos(\Delta t)$	$-\sin(\Delta t)$	$\omega_0 - \Delta$
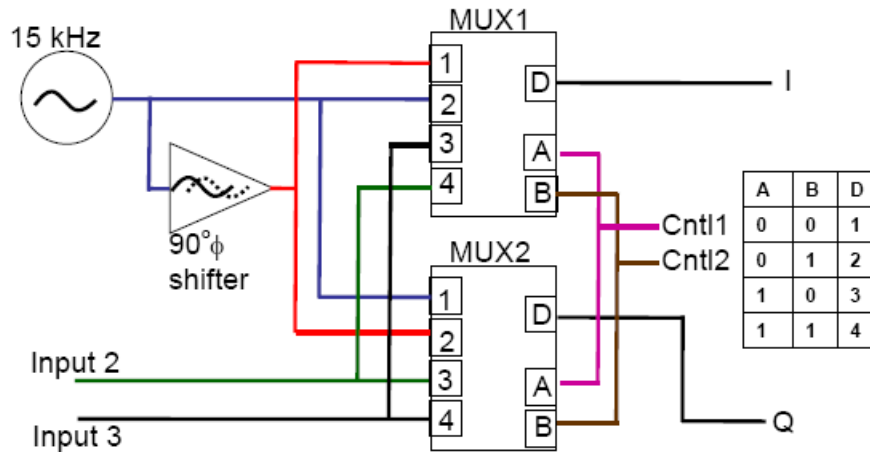
Figure 3.21. Schematic diagram of multiplexer. Four inputs are fed into the multiplexer and digital control bits (Cntl1 and Cntl2) select which two signals are fed into the IQ modulator.

3.4   Optical & Electronics Performance

With all locking electronics and optical components working in unison, examining the differential signal is the first step in making the locking circuit work. As shown in Fig. 3.22, the two elements of the PD show exactly opposite phase (180 degrees) beat frequency that is exactly at 15 kHz. Note that the DC level is the same which allows the complete subtraction at the differential amplifier and subsequently attenuated as desired.

Photodetector Output
PD-A and PD-B
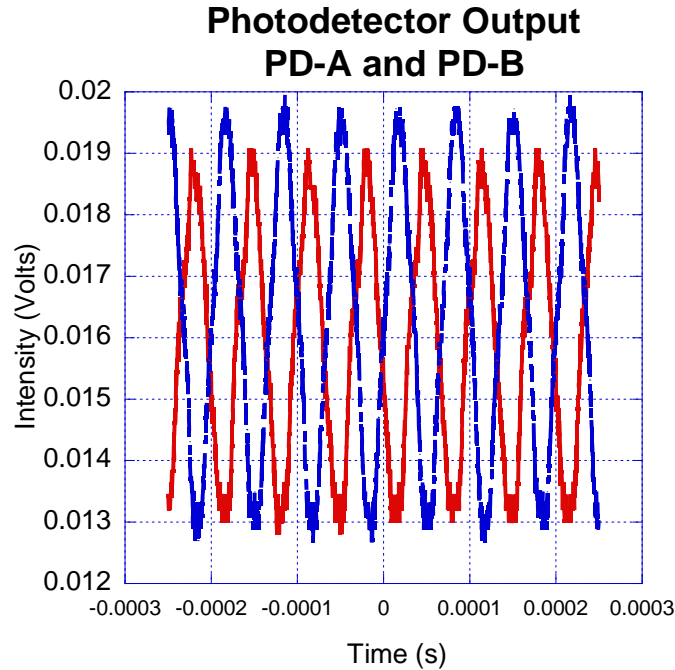
Figure 3.22 Interference from the two laser beams show as 15kHz beat note. Holding
this signal constant is equivalent to holding phase constant.

From the PD output we can do further analysis with the error signal and feedback signal.

As an example of the working vs. non-working locking signal, we see the phase locking

(working) in action as shown in Fig. 3.23. When the locking pulse is on (blue), the S/H is

on a sample mode. The error signal (red) is initially at zero as we are holding the phase

at zero by having the error signal feedback to the EOM, which in turn, adjusts the phase.

Therefore, the feedback to the EOM (black) is increasing. The circuit awaits until a

specified delay time ($\sim 3.6\,\mu s$) and then sets the S/H to hold mode. From this time on,

the feedback to the EOM is constant; the laser phase is starting to develop as shown by

start of sine wave from zero in the error signal.

Notice that the feedback signal (black) is not same shape at every pulse-on cycle

which means the phase is different and constantly changing. When the pulse is off, the

lock is no longer in effect and the feedback is zero. At every locking pulse-on, the shape

Phase Locked Signal
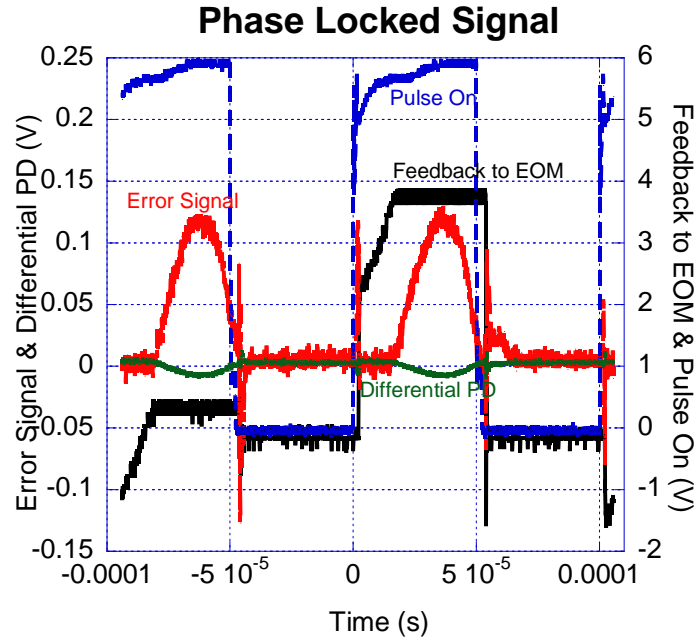
Figure 3.23. Plot shows good locking of phase. Pulse on (Blue). Differential PD signal – inverted (Green). Locking signal (Red). EOM Feedback signal (black). Shows error signal start at zero for 3.6 μs and then starts sinusoidal wave form indicating laser to develop its phase.

Phase Unlocked Signal
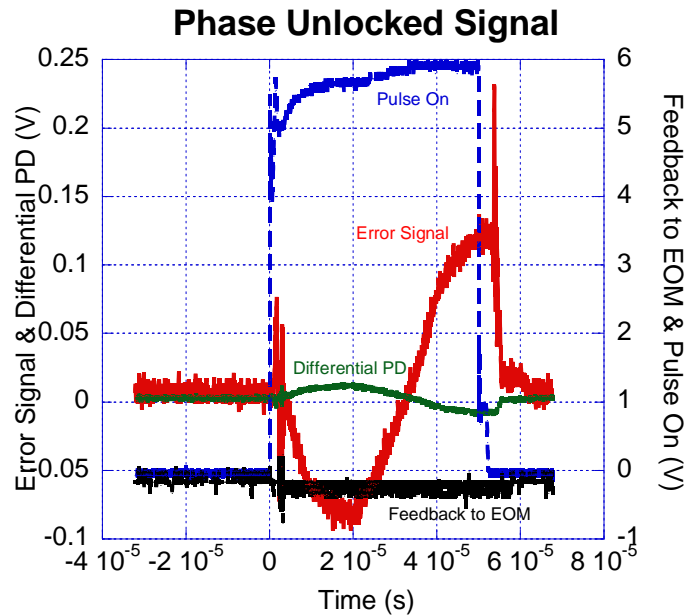
Figure 3.24. Plots here show circuit not locking the phase. Notice the error signal (red) starts as upside-down sinusoidal wave. Compare this with Fig. 3.20 to see the difference.

of the error signal should be identical – it should quickly go to zero and be delayed $3.6\,\mu s$ before starting a sinusoidal oscillation. As long as the differential PD signal is stable the circuit is working properly. However, there are cases when the locking fails due to a power glitch, sudden bumping of PD, laser beam intensity fluctuation, etc.

In Fig. 3.24, this graph shows example phase lock not working. At the start of the pulse (blue), the phase is not stable and is no longer the proper sinusodial wave (red). It is actually flipped inverted here, however, this is arbitrary and could show up as any incorrect phase. With this error signal, the phase is random and feedback to the EOM is arbitrary. This occurs more often when the delay time for locking is shortened. This can be clearly be seen when the delay is reduced from $3.6\,\mu s$ to $2.0\,\mu s$. This error signal is used as a monitoring signal during the actual experiment. This is a direct way of checking the phase stability at the start of the pulsed beams.

Figure 3.27. Monitoring of phase locking during experiment. Shows error signal for (a) short and (b) long pulse times which shows locked behavior.

As a final test to the instrumentation, we monitor the error signal as we asymmetrically split the atoms for Rabi oscillation measurement (chapter 5). When the

pulse is on, we verify that error signal shows the proper waveform. Such an example is shown in Fig. 3.27 where the error signal, as well as the two PD signals, are seen.
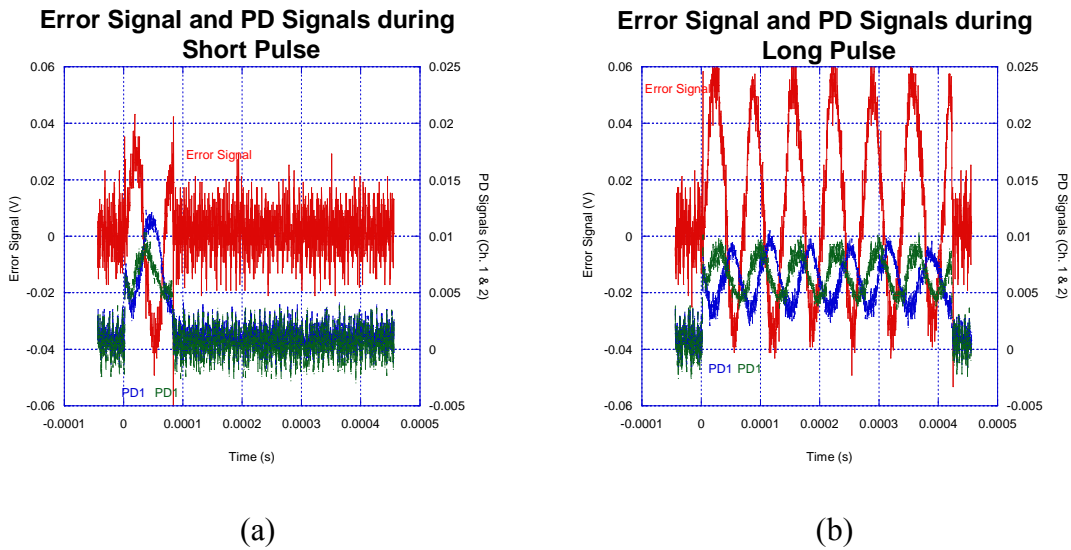
With the phase locking circuit and the AOM driver circuit working, we can implement the circuit to the actual asymmetric splitting of the BEC. However, before proceeding further, a quantitative analysis of phase locking performance is explored.

3.5 Phase Correction Accuracy & Locking Stability ($d\phi$)

As the S/H circuit and AOM amplifier unit performs jointly, we study the stability of the locking circuit. This can be done statistically. For the locked circuit, which yields a sinusoidal waveform after a lock, we recorded N samples $f_i(t)$ where i is the waveform number. We defined the average $\overline{f(t)} = \sum_i f_i(t)/N$ and the deviations

$$\delta f_i(t) = f_i(t) - \overline{f(t)}. \tag{3.5.1}$$

We see that $\overline{f(t)}$ is well described as

$$\overline{f(t)} = A_0 + A\sin(\Omega t + \varphi) \tag{3.5.2}$$

where A_0 is an offset, A the amplitude, Ω the frequency, and φ is the offset phase. Consider each waveform to be a deviation from this average $\overline{f(t)}$ as

$$f_i(t) = A_0 + (A + \delta A)\sin(\Omega t + \varphi + \delta\phi) \tag{3.5.3}$$

where δA is a small deviation in amplitude and $\delta\phi$ is a small deviation from the phase φ. Re-writing the equation (3.5.3) in an expanded form

$$= A_0 + (A + \delta A)(\sin(\Omega t + \varphi) + \delta\phi\cos(\Omega t)) \tag{3.5.4}$$

Ignoring the second order quantities

$$= A_0 + (A\sin(\Omega t + \varphi) + \delta A\sin(\Omega t + \varphi) + A\delta\phi\cos(\Omega t + \varphi) + \cancel{\delta A\delta\phi\cos(\Omega t + \varphi)}) \tag{3.5.5}$$

So, (3.5.1) becomes

$$\delta f_i(t) = \delta A\sin(\Omega t + \varphi) + A\delta\phi\cos(\Omega t + \varphi) \tag{3.5.6}$$

Multiplying both sides by $\cos(\Omega t + \varphi)$

$$\frac{1}{A}\cos(\Omega t + \varphi) \cdot \delta f_i(t) = \frac{\delta A}{A}\sin(\Omega t + \varphi)\cos(\Omega t + \varphi) + \delta\phi\cos^2(\Omega t + \varphi) \tag{3.5.7}$$

Define $\theta = \Omega t + \varphi$ and n is a multiple cycle index, integrate both sides

$$\int_0^T \frac{1}{A}\cos(\theta) \cdot \delta f_i(t)d\theta = \int_0^{n\pi} [\frac{\delta A}{A}\sin(\theta)\cos(\theta) + \delta\phi\cos^2(\theta)]d\theta \tag{3.5.8}$$

RHS is equal to $\delta\phi$ and recasting the integral in terms of time

$$\delta\phi = \frac{2\Omega}{n\pi}\int_0^T \cos(\Omega t + \varphi) \cdot \left(\frac{\delta f_i(t)}{A}\right) dt \tag{3.5.9}$$

Substituting $U = \cos(\Omega t + \varphi) \cdot \left(\frac{\delta f_i(t)}{A}\right)$ and converting the integral as discrete sum

$$\delta\phi_i = \frac{2\Omega}{n\pi}\left[\frac{1}{2}U_0 + \sum_{ij}^{N-1} U_{ij} + \frac{1}{2}U_n\right]\Delta t \tag{3.5.10}$$

Where i is column matrix. Hence

$$U_i = \cos(\Omega t) \cdot \left(\frac{\delta f_i(t)}{A}\right) \tag{3.5.11}$$

So this gives $\delta\phi_i$. So

$$< \phi_i^2 > = \frac{1}{N}\sum_{i=1}^{N} \delta\phi_i^2 \tag{3.5.12}$$

Finally arriving at the expression of accuracy of phase as

$$\delta\phi = \sqrt{< \phi_i^2 >} \tag{3.5.13}$$

For different delay times, we measure 100 samples. As the delay gets longer, the phase accuracy improves. Our desired delay is $3.6\,\mu s$, which is experimentally set by a potentiometer dial of 7.5 turns from zero. As shown in Fig. 3.25, we plot and fit the average $\overline{f(t)}$ for each delay times and calculate $\delta\phi$'s for each delay times. We fit the data and obtain a relationship between the phase accuracy and delay times as plotted in Fig. 3.26.

The stability of the lock is very stable as indicated by ~ 1 mrad at $3.6\,\mu s$. As you vary the S/H delay times, glitches show up when getting too close to shorter delay times. This is due to the fact that it takes some time for the electronics to lock and also timing between the laser being present in the actual AOM crystal and S/H trying to lock when there is no beam. Of course, when there is no beam in the AOM/EOM, there is no lock
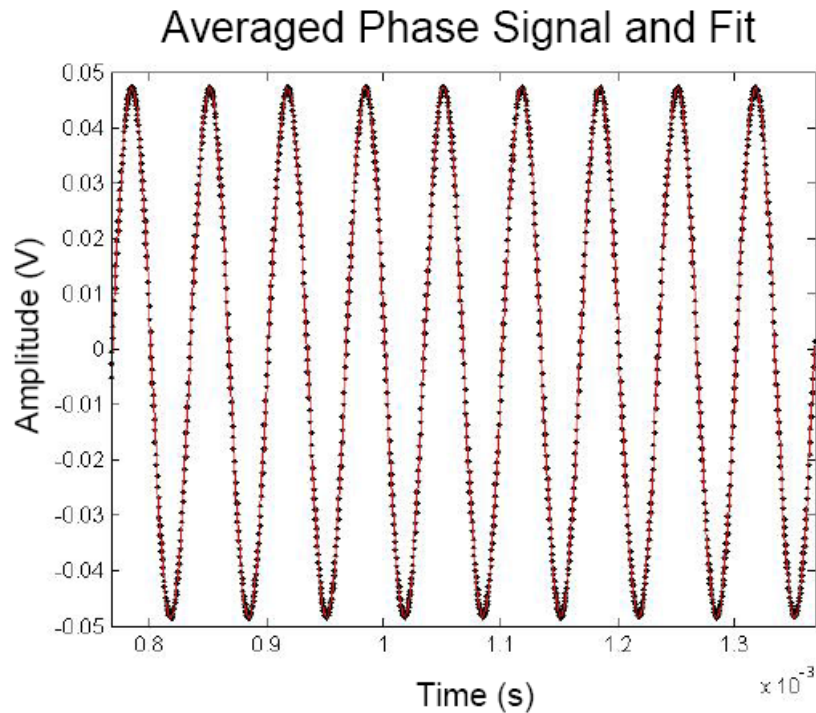
Figure 3.25. Sine fitted phase locked signal of 100 sampled averaged for delay time = 3.6 us.

Phase Lock Accuracy
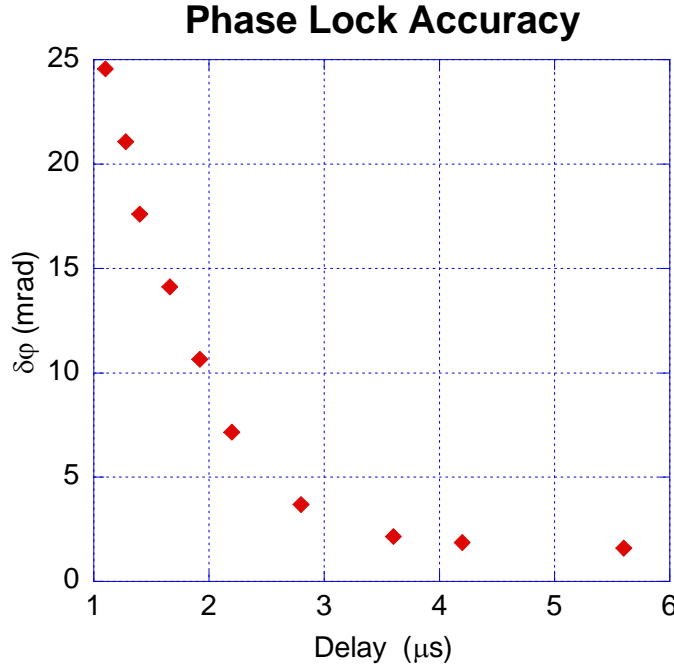
Figure 3.26.   Delay of sample and hold. For our purpose, 7.5 turns is equal to about 3.6 μs delay. At this setting, the phase locking accuracy is ~1mrad.

signal. Originally, we proposed that we want to accurately lock ϕ to within 10 mrad as this is the accuracy that we have in measuring the interferometer phase. However, from our results, we can control the phase of the laser beams down to 1 mrad which is a factor of 10 better than proposed. This means that although there are plenty of other sources of phase noise in the experiment, we are far from being limited by the laser system.

3.6   Summary

We successfully built an optical and electronic feedback system to accurately phase lock the two laser beams for the asymmetric splitting operation. Some of the major practical challenges were finding and correctly implementing low cost rf power amplifiers, and determining an effective protocol for aligning the laser beams quickly and

repeatedly. We overcame these challenges and the system now works reliably and can

stay locked for days.

4.0

Bose-Einstein Condensate

Production of BEC and its Trap Characteristics

The atom interferometry experiment starts with the production of BEC. Our lab has been doing atom interferometry for over a decade and have previously used an atom interferometer to measure the electric polarizibility, gravity, and to implement an atom gyroscope. All experiments used the symmetric splitting process. Our work presented here is a different type of atom interferometer using asymmetric splitting. In this chapter we describe the BEC producing apparatus, its production, and the waveguide trap.

4.1   A Brief History of Bose-Einstein Condensate

In the early 1920, an Indian physicist Satyendra Bose and Albert Einstein developed the idea that a certain type of atoms called bosons exhibit an unusual behavior when cooled to a lower temperatures. Unlike the fermions which obey the Pauli-exclusion principle, multiple bosons can occupy the same quantum. When many bosons co-exist in the same state, they produce a coherent matter wave. The comparison of BEC to a gas of thermal atoms is equivalent to comparing laser to a white light source in optical interferometer. In practice, BEC is formed by laser cooling and trapping techniques combined with a rf forced evaporation. The first BEC production was awarded the Nobel prize in 1995 to a group of physicists at the University of Colorado and at MIT.

4.2   Casslab BEC production

The experiments described here were performed in a new BEC apparatus. Our it first produced ^{87}Rb BEC on Feb 18th, 2014. The vacuum chamber consists of two glass cells linked by a thin tube, as shown in Fig. 4.1. The first chamber has a base vacuum pressure of 2×10^{-9} Torr. In this cell, atoms are loaded into a magneto-optical trap (MOT). The MOT consists of a quadrupole magetic field with three pairs of mutually perpendicular cooling laser beams slightly red tuned of the $5S_{1/2}, F = 2 \rightarrow 5P_{3/2}, F = 3$ transition of ^{87}Rb . Also present is a weaker 'repump' laser beam which drives the $5S_{1/2}, F = 1 \rightarrow 5P_{3/2}, F = 2$ transition. This is needed to prevent the atoms from being trapped in the F=1 state. The temperature of the MOT is approximately $200\,\mu K$ and
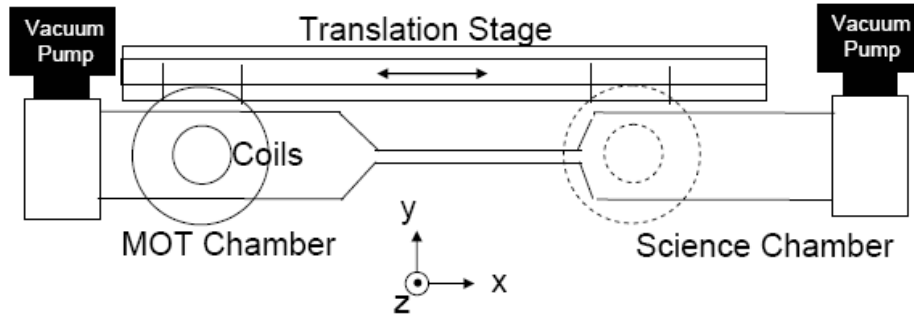
Figure 4.1 Top view of the experiment chamber. The MOT chamber and BEC chamber is connected via small tube and coils move on a translation stage. The bragg beam is in the y direction at the science chamber.
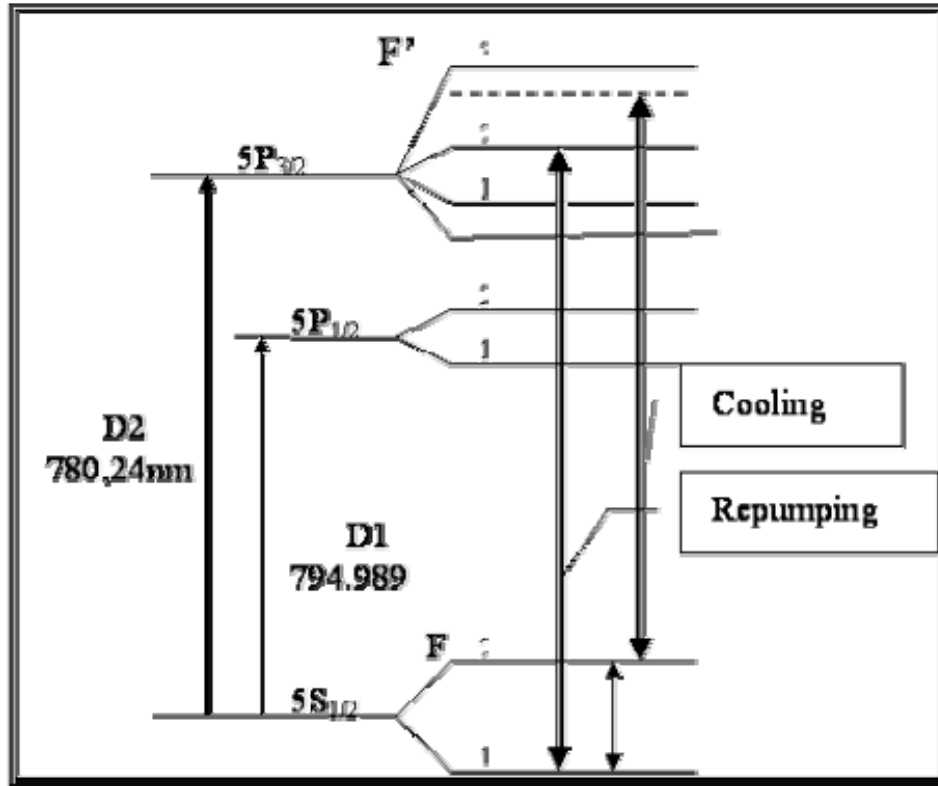
Fig. 5.1 Energy level diagram for [87]Rb D2 cooling and repump.

amasses about 10^9 atoms in a spherically shaped 'ball' at the center of the cell.

The temperature of the atoms in the MOT cannot be further reduced due to the constant momentum recoil-exchange with photons via an absorption and emission

process. This prevents atoms to come to a complete stop, and the minimum temperature is often called the Doppler limit. There are other laser cooling techniques which can cool beyond the Doppler limit, but in our system, the density of the atoms is too high to achieve sub-Doppler cooling.

However, the density of atoms in the MOT is too low to produce a condensate. Typically, the MOT density is around 10^{10} atoms/cm^3, but at a temperature of $200\,\mu K$, BEC would require a density of 1×10^{13} atoms/cm^3 at temperature of $1\,nK$. Therefore, another stage of cooling is required. This involves turning off the laser beams and holding the atoms with only the magnetic fields. We call this a magnetic trap.

The magnetic trap initially consists of a quadrupole field with anti-Helmholtz coil configuration. This is similar to the field used in the MOT but we increase the magnetic gradient state from 10 Gauss/cm to 450 Gauss/cm. In this configuration, the atoms are trapped in the $5S_{1/2}, F=2, m_f=2$ state where m_f is the magnetic quantum number. No laser beams are present. We then move the coil (along with atoms) using a translation stage to the science chamber where the vacuum is maintained at a much lower pressure of 3×10^{-11} Torr.

The quadrupole trap has a significant flaw: at the zero point of the magnetic field, atoms can get lost, via the Majorana transition, $m_f=2 \rightarrow m_f=-2$. These atoms fall out of the trap, experiencing it as an anti-trapping potential. This is very important as at the center of the trap where the density is the highest, more loss will occur preventing the formation of condensate. To prevent the zero point loss, we use a more sophisticated trap called the time-orbiting-potential (TOP). It is basically an added time-dependent magnetic field on top of the quadrupole field so that the zero point of the magnetic field

moves around in a circular path at a high frequency. We carefully design the orbiting frequency so that the atoms cannot physically follow the orbiting zero point. Instead the atoms experience a time-averaged force that confines them at the center.

The final stage before making the BEC is the rf evaporative cooling. It is a forced evaporative cooling process which ejects the hottest energy atoms from the trap via rf radiation which is resonant with the atoms near the edge of the trap. More specifically, only the most energetic atoms are able to reach the edge of the trap where the potential is highest. Hence the rf evaporation tunes the frequency to drive the $m_f = 2 \rightarrow m_f = -2$ transition at the trap edge. Once the high energy atoms are ejected, the remaining atoms re-thermalize to a lower temperature. Re-thermalization occurs as a result of inter-atomic collisions. We go through a successive iteration of rf evaporation process, lowing the temperature of the remaining atoms at each succession. The whole process takes about one minute. The result is a formation of BEC with temperature of about 100 nK, with about 1×10^4 atoms. For further information of BEC formation, previous graduates thesis contain wealth of information and details of apparatus and techniques [25,26,27,28].

4.3   Transfer to Cube Trap

In the BEC chamber, another effort led by Rob Horne is to create a novel atom trap based on six independent coils inside the vacuum chamber on a one-inch cube as shown in Fig. 4.2. The original intention of the cube trap is to create a circular path geometry for realizing an atom gyroscope. For our purposewe excite atomic motion along only one direction. The cube trap is positioned inside the science chamber with the center of the trap overlapping that of the quadrupole trap. the cube coils produce the
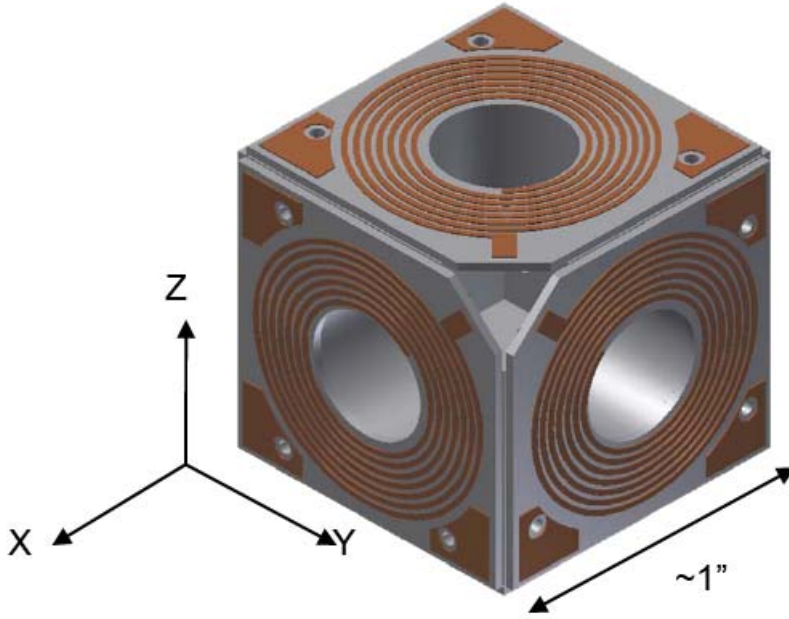
Fig. 4.2. Shows cube trap with six side coils independently biased to create adjustable trap configuration for atom waveguide. Originally built for gyroscope atom waveguide experiment. Centers on each sides have holes for laser beams to pass through. Reference [24]

rotating field used to make the TOP trap. To load the cube trap, we adiabatically reduce the dc quadrupole field to zero.

The cube trap can generate the cylindrically symmetric trapping potential,

$$U = \mu B_0 + mgz - \frac{\mu B_{ACz}}{2} z + \frac{1}{2} m\omega_z^2 z^2 + \frac{1}{2} m\omega_\rho^2 z^2 \rho^2 \qquad (4.3.1)$$

where the trap frequencies,

$$\omega_\rho^2 = \frac{\mu_B}{m} \left(\frac{1}{8} \frac{B_{DCz}^2}{B_0} + \frac{7}{64} \frac{B_{ACz}^2}{B_0} \right) \qquad (4.3.2)$$

$$\omega_z^2 = \frac{\mu_B}{m} \left(\frac{B_{DCz}^2}{2B_0} + \frac{B_{ACz}^2}{8B_0} \right) \qquad (4.3.3)$$

where B_0 is rotating bias field, $B_{DCz} = \dfrac{\partial B}{\partial z}$ is the dc qudrupole field, and $B_{ACz} = \dfrac{\partial B}{\partial z}$ is the cube quadrupole field. Te cube quadrupole field also provides support against gravity.

One attractive feature about this trap is we can manipulate the trap frequencies by adjusting the coil currents. For our experiment we use trap frequencies:

$$\omega_x = 2\pi \times 2\,\mathrm{Hz},\ \omega_y = 2\pi \times 2\,\mathrm{Hz},\ \omega_z = 2\pi \times 6.5\,\mathrm{Hz} \qquad (4.3.4)$$

The trap with the above condition provides a weakly confining waveguide for the atoms [29].

4.4   Imaging

The imaging of the atoms is used to ascertain the number, temperature, position, and velocity of the atoms. We use a technique called absorption imaging to take a snapshot of the atoms at a given time. Technically, an image is acquired by passing a near-resonant laser beam through the atoms to a CCD camera on the opposite side. Since the laser beam is near resonance, it is absorbed by the atoms leaving a darker spot on the CCD where the atoms should be as compared to a bright background. At the same time we take an image, we also destroy the BEC due to photon scattering.

We take two images, one with the atoms present and one without. In addition, a background image is taken for no laser probe. The images are processed to give a signal image defined by

$$\mathrm{Signal(x,y)} = \frac{\text{atom image - background}}{\text{no atom image - background}}. \qquad (4.4.1)$$

The transmission of the laser beam through the atoms follows the Beer's law, so that at each pixel (x,y)

$$\text{Signal(x,y)} = Ae^{-\kappa(x,y)} \tag{4.4.2}$$

where $\kappa(x, y)$ is the absorption coefficient of the atoms at location (x,y). We fit $\kappa(x, y)$ to a Gaussian to ascertain various parameters such as the atoms central position and cloud size.

We use an Apogee Alta U1 CCD camera. Three different signal images of the atoms in the final stages of rf forced evaporation cooling are pictured with a false color as shown in Fig. 4.3

| (a) | (b) | (c) |
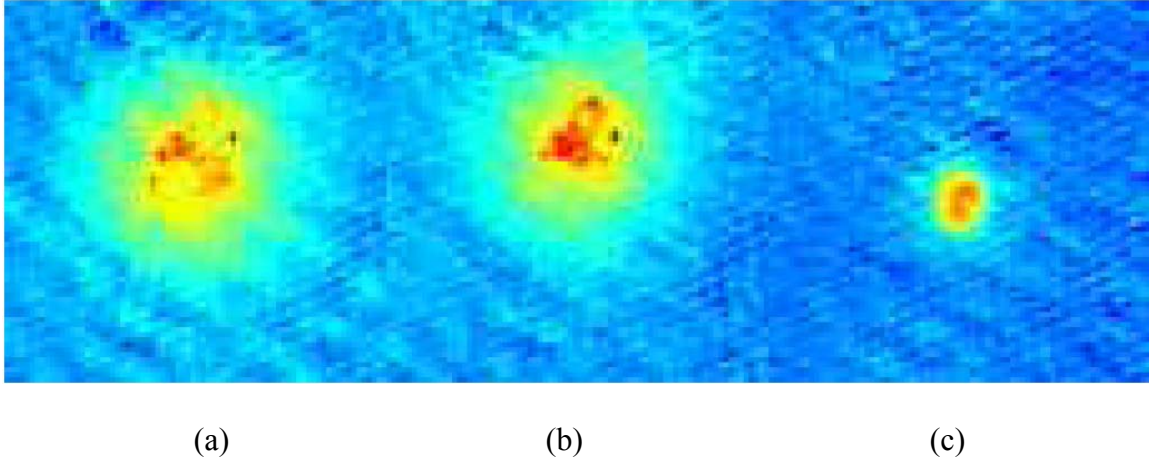
Figure 4.3.   First picture of BEC production on Feb 18th, 2014. (a) thermal atom cloud, (b) thermal/bec atoms, and (c) BEC.

4.5   Summary

In this chapter, we described the BEC production through the stages of MOT, magnetic trap, TOP trap, and rf evaporation cooling. Our set up is a two chamber system connected via a small thin tube which separates the MOT chamber to the science chamber where the BEC is made. In the science chamber is a new type of trap which provides the weakly confining waveguide for our asymmetric splitting experiment. We

use the absorption imaging method to take the images of the atoms at the end of interferometer measurement. At this stage, we have all the necessary tools to start the interferometer: optics, electronics, BEC, waveguide, and imaging.

5.0

Asymmetric Splitting

Manipulating Atoms with Pulsed Laser Beams

With a solid understanding of the theory, optical, electronics, and atomic ensembles, we can proceed with the asymmetric splitting experiment. From the previous chapters we had amassed quite a bit of expertise in setting up the instrumentation to control the phase of the pulsed laser beams. We can now put that to work and finish towards an asymmetric interferometer. During the process, we will revisit some theoretical relationships to ascertain key laser beam values such as intensities and pulse times. In

this chapter, we describe testing of the asymmetric splitting technique. We measure the population in the two interferometer states as a function of pulse times, as described in the theory chapter (chapter 2). Such a test forms the basis for further interferometer work.

5.1   Asymmetric Splitting Test Set-up

We discussed the theory of Bragg asymmetric splitting of BEC in chapter 2 and described the optics and electronics for implementing Bragg splitting in chapter 3. Briefly re-stating the concept, we want to split BEC atoms asymmetrically by making the transition from the $|0\rangle$ to the $|2\hbar k\rangle$ motional state. Experimentally, this transition can happen by sending pulsed laser beams with two different frequencies, ω and $\omega + \Delta$ while fixing the initial relative phase of the laser beams to zero. The Bragg beam portion of the experiment is shown in Fig. 5.1.

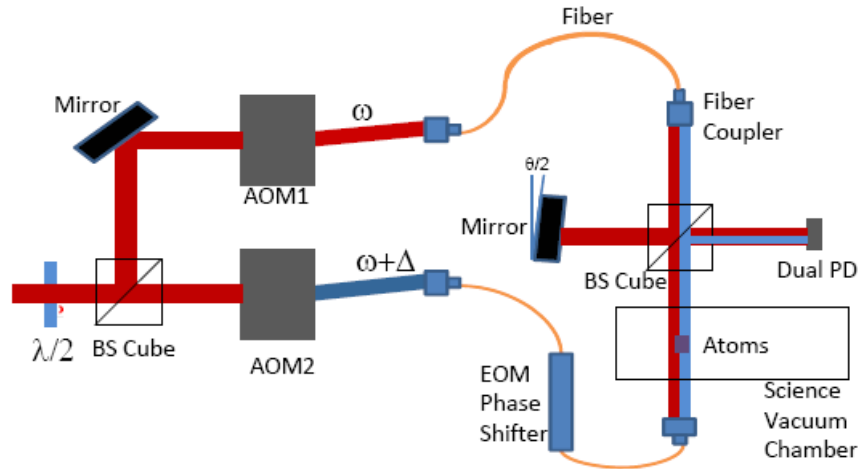Fig. 5.1. Beam delivery to the science chamber via optical fiber and EOM. Several mirrors and polarizers are omitted in the drawing to focus on beam delivery and alignment set up. For detailed optical set up, refer to Fig. 3.1.

The splitting laser beam comes from a New Focus Stablewave 7000TLM laser, blue detuned from the cooling transition $5S_{1/2}, F = 2 \rightarrow 5P_{3/2}, F = 3$. During the testing

process we tried several different wavelengths but at the end used $\lambda = 780.152$ nm for the interferometer work (chapter 6). The laser beam is split into two via a half-waveplate and polarizing beam splitter cube. The two beams go through two AOMs to provide intensity control and to generate the frequency offset. The beam with frequency ω is coupled into a single mode fiber and while the beam with frequency $\omega + \Delta$ is coupled into a fiber based electro-optical modulator (EOM). Near the science chamber, both beams have a $1/e^2$ radius of 1.4 mm. The plain fiber output is mounted on XYZ translation stage with micrometers for position accuracy. The output of this beam passes along the y-axis as defined in Fig. 4.2, through a polarizer and the beam cube assembly before going through the chamber where the atoms are located. On the other side of the chamber, the EOM fiber output goes through a polarizer and two mirrors before passing through the chamber. The beam cube assembly detected the relative laser phase as explained in chapter 2. Two beam phase interference output is spatially detected with a PD.

For asymmetric splitting to work, we must align the laser beams onto the atoms as well as aligning the beams at the phase detector. Hence we have two constraints we need to satisfy. The alignment of the beams on the atoms is performed by tuning the laser near resonance and measuring the loss produced by a laser pulse. We first adjusted the position of the plain fiber output to maximize this loss. Figure 5.7 shows the loss measurement as a function of beam position. We then used mirrors to direct the beam from the EOM fiber back into the plain fiber. This ensured that both beams were overlapped on the atoms.
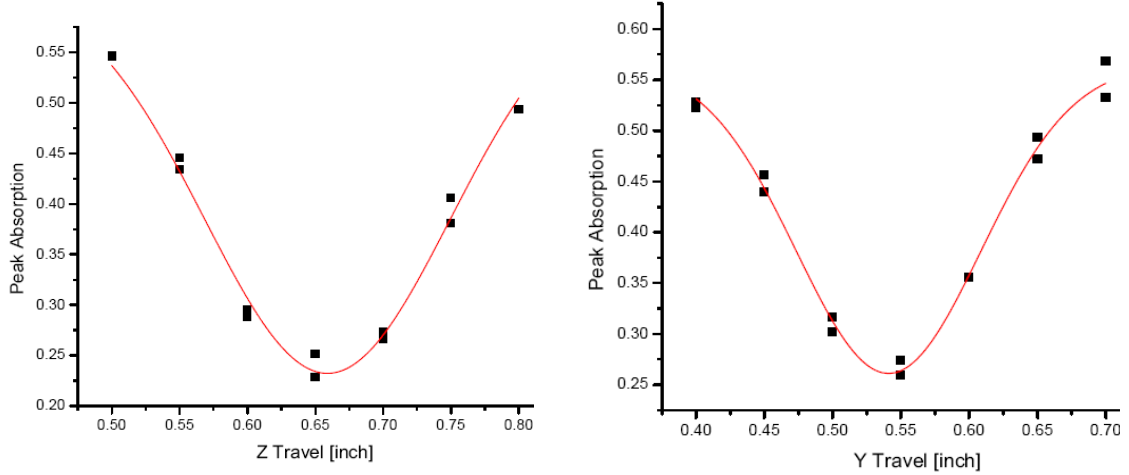
Figure 5.2 Bragg beam alignment using absorption technique. We fit the inverted Gaussian curve which gives us the position in the Z and X direction.

After aligning the beams on the atoms, we adjusted the phase detector photodiode and mirror alignment to maximize the phase detection signal. This process does not (by design) change the alignment of the beams on the atoms.

Another effect that needs attention is the polarization. For the splitting operation and to obtain interference at the phase detection PD, we need to set the linear polarization axis of the laser beams to the same axis. In our case we set the polarization axis to vertical. Both optical fibers are polarization maintaining. We established vertical polarization by fibers' axis to be vertical. However, we found that it was necessary to use polarizers to obtain good polarization accuracy. This was evident in the phase detection signal as its visibility is reduced when the two beam polarizations are not identical.

We asymmetrically split the atoms using a pulsed laser beams counter-propagating with respect to each other at the atoms. When verifying the phase locking, we see an error signal initially locked at zero and then develop into a sinusoidal wave as the pulse starts as previously shown in Fig. 3.27. Once a good error signal is obtained, we run a few tests by splitting the atoms with a short pulse of tens of μs.

We monitor and stabilize our laser frequency by picking off one of the 0th order beam from one of the AOM outputs and feeding it into a wavemeter. After turning the laser on, it takes about 30 minutes to stabilize. Infrequently, the wavelength of the laser beam shifts by 0.001 nm, and then we manually re-adjust the laser to the desired wavelength of 780.152 nm. We monitor the intensity of the beams by picking off the 0th order from the other AOM, and meqasuring it with a photodetector throughout the experiment. Another way to monitor the intensity is by constantly observing the phase detector PD signals at every pulsed operation to make sure the voltage level is consistent throughout the experiment. Minor optical adjustment is occasionally needed.

5.2   Rabi Oscillation

Based on the numerical simulation in chapter 2, the asymmetric split pulse, can induce a transition from the $|0\rangle$ state to the $|2\hbar k\rangle$ state with varying population inversion. To verify this, we initially image the atom position via an absorption imaging technique. Once the position and the number of atoms are ascertained, we run the experiment again and apply the Bragg beams. We wait 100 ms, allowing the $2\hbar k$ atoms to move 1.2 mm (140 pixels). We then take an absorption image and process it to determine the relative number of atoms at different velocities.

To asymmetrically split the atoms, initially we obtain the intensity parameter β from our numerical simulation from chapter 2 Fig. 2.2. From the plot in Fig. 2.2, we choose β to be around 2, providing a good compromise between efficiency and velocity sensitivity. We initially used 3mW total beam power with beam waist of 2 mm at a

detuning of 780.220 nm. We calculate $\beta \equiv \dfrac{\Gamma^2 I_0}{4\Delta I_{sat}} = 6.75$ kHz which is $\sim 1.79\,\omega_r$. Later

in the experiment we change the detuning and try several different wavelengths to settle

on an optimal wavelength which will be discussed in the next chapter.

For each experiment run, which encompasses making the BEC to absorption

imaging, we analyze the image calculating position and atoms numbers. This is plotted

and we see the Rabi oscillation as predicted as shown in Fig. 5.3. To characterize the

effect of the pulse, we vary pulse duration from $10\,\mu s$ to $300\,\mu s$.
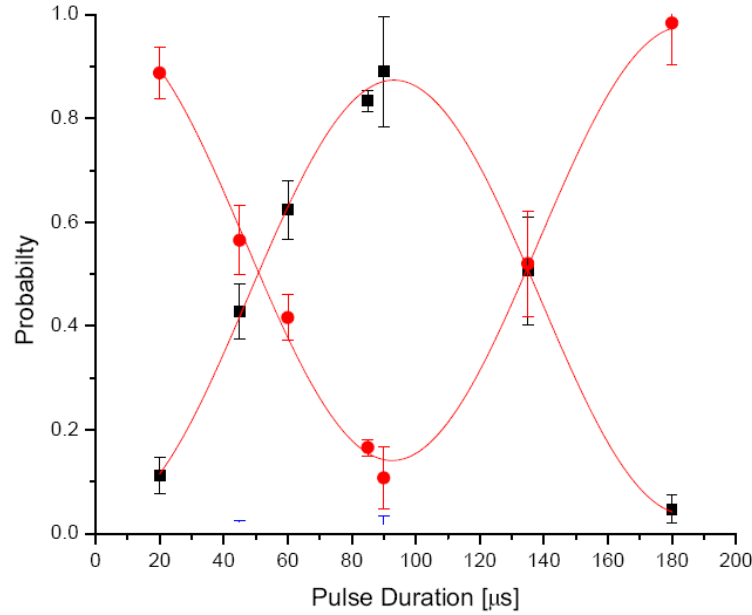
Figure 5.3 shows first cycle of Rabi oscillation. Population density inversion is evident at $\tau = 90\,\mu s$.

An example of such an asymmetric split is shown in Fig. 5.4. We are able to drive the

transition where the two momentum states are equally populated with a $\dfrac{\pi}{2}-$pulse, as

well as transferring all atoms to the $\left|2\hbar k\right\rangle$ state with a $\pi-$pulse. Recall that the different

pulse duration gives different population states from the Rabi model. For example,

during our initial testing stage, an asymmetric split pulse duration of $45\,\mu s$, the atoms are ½ and ½ in both states where as a pulse time of $90\,\mu s$ the transition to $|2\hbar k\rangle$ state is mostly complete. Note that each experiment requires making a new BEC.
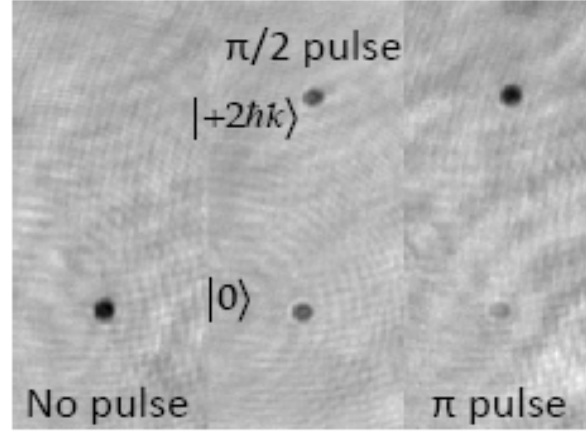
Figure 5.4. Three different laser pulses, $0, \pi/2, \pi$ with $\beta = 1.79\,\omega_r$. Different pulse times determine population density in asymmetric splitting. This result is the direct effect of the Rabi oscillation.

For one complete Rabi oscillation, we use laser intensity parameter I = $\sqrt{2 \times 0.2}/(\pi \times 0.175^2)$ = 6.57 mW/cm^2, with beam waist 1.75 mm, and detuning of 780.220 nm. Note that one of the beam had 2mW but the other had 0.2mW. We calculate $\beta \equiv \dfrac{\Gamma^2 I_0}{4\Delta I_{sat}}$ = 3.2 ω_r. From the period of oscillation T=182 μs, we infer $\beta T = 2\pi$ and obtain $\beta = 1.45\,\omega_r$. This indicates that our experiment estimate for β is about a factor of 2 off. A part of the issue is that although the beams are aligned to the atoms, this alignment is not perfect, and can drift over time. This lowers the intensity and thus β. Usually, the β values calculated from the intensity and detuning are not reliable as the intensity of the beam may fluctuate and polarization may change during every experiment runs (for an extended time, we did not use polarizers). What is reliable is

obtaining the Rabi curve. We focus on getting the correct β value from the period rather than calculated value.

5.3   Summary

We perform the initial asymmetric splitting experiment and obtained a Rabi oscillation curve. The Rabi oscillation is a direct check of asymmetric splitting, allowing us to implement $\frac{\pi}{2}$- pulse and π- pulse. We use the Rabi curve to calibrate the beam intensity via the β parameter. We verify that asymmetric splitting works as expected and will be using it to create atom interferometer in the next chapter.

6.0

Asymmetric Interferometers

Measuring Recoil Frequency Using an Asymmetric Interferometer

We investigate a few asymmetric interferometers using the operations asymmetric split, reflect, and recombine. The simplest interferometer we perform is an interferometer where the atoms are asymmetrically split only to be followed immediately by asymmetric recombination. We configure the wait time between the pulses such that the atoms do not have enough time to spatially separately completely, but they do have

two distinct packets with different momenta. After the second pulse we allow the atom wave packets enough time to separate and measure the resulting momentum distribution. The main advantage of this interferometer is that it requires only the asymmetric splitting operation demonstrated in chapter 5. We call this first interferometer a Ramsey interferometer, after American physicist Norman Ramsey who used a similar technique to measure transition frequencies of molecules using magnetic resonance.

The second interferometer uses a reflection pulse, where the atoms are split asymmetrically, the moving packet is reflected and return back to the original position, and then the two packets are recombined. We call this the Ramsey-Borde type 1 interferometer. French physicist Christian Borde developed a similar interferometer scheme for a thermal atom interferometer.

The third interferometer is the Ramsey-Borde type 2 interferometer where the moving atom wave packet undergoes two reflections, making the path journey on both side of the initial position, before recombining with the atoms at rest. Through all three interferometers, we can measure the recoil velocity of atoms and compare it with current accepted values. We will explore these interferometers in more details in the next few sections.

6.1 Ramsey Interferometer

The Ramsey interferometer provides a simple and reliable test for us to illustrate the phase locking performance. At the same time, it can also measure the atomic recoil frequency. The basic trajectories for the interferometer are shown in Fig. 6.1. The atom packet is initially at rest, and is split with a $\frac{\pi}{2}$ – pulse. Within a very short time later, τ ,

an identical $\frac{\pi}{2}$ – pulse is applied. Te time τ must be short enough that the two packets

do not separate. This interferometer has two outputs. We will analyze the behavior this

section.

The moving atom velicoty is 12 mm/s, and the packet size is about 0.1 mm. The

interferometer time τ must therefore be small compared to 0.01s. We explore the τ

dependence of the interferometer signal below.
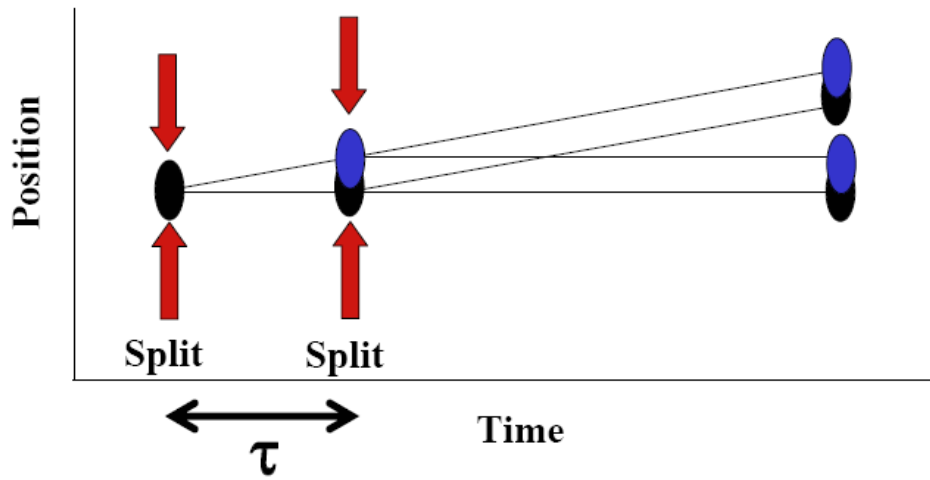
Figure 6.1. Ramsey interferometer configuration. Two identical asymmetric pulses with wait time τ in between. Atoms are separated in momentum space but spatially overlapped.

To accurately understand the Ramsey interferometer, we must include the fact

that the atoms start with a small non-zero momentum $p_i = \delta \hbar k$. Quantum mechanically,

we start with a wave packet described as $|\psi\rangle = |\delta\rangle$. After the first asymmetric split, the

wavefunction becomes

$$|\psi\rangle \rightarrow \frac{1}{\sqrt{2}}\left[|\delta\rangle + i|2 + \delta\rangle\right] \tag{6.1.1}$$

where $|2+\delta\rangle$ describes a packet with momentum $(2+\delta)\hbar k$. After free evolution time τ, the atoms in the both states develop phases

$$|\psi\rangle \to \frac{1}{\sqrt{2}}\left[e^{-i\frac{\delta^2 \tau}{2m\hbar}}|\delta\rangle + ie^{-i\frac{(p+\delta)^2 \tau}{2m}\frac{\tau}{\hbar}}|2+\delta\rangle \right]$$

$$= \frac{1}{\sqrt{2}}\left[e^{-i\frac{\delta^2 \tau}{2m\hbar}}|\delta\rangle + ie^{-i\frac{p^2 \tau}{2m\hbar}}e^{-i\frac{2p\delta \tau}{2m}\frac{\tau}{\hbar}}e^{-i\frac{\delta^2 \tau}{2m\hbar}}|2+\delta\rangle \right]$$

$$= \frac{e^{-i\frac{\delta^2 \tau}{2m\hbar}}}{\sqrt{2}}\left[|\delta\rangle + ie^{-i\frac{p^2 \tau}{2m\hbar}}e^{-i\frac{2p\delta \tau}{2m}\frac{\tau}{\hbar}}|2+\delta\rangle \right] \tag{6.1.2}$$

where $p = 2\hbar k$. If we substitute $\omega_r = \frac{\hbar^2 k^2}{2m\hbar}$ and set $\phi_r = 4\omega_r \tau$, and omit the overall phase, the equation is simplified as

$$\frac{1}{\sqrt{2}}\left[|\delta\rangle + ie^{-i\phi_r}e^{-i\frac{2k\delta\tau}{m}}|2+\delta\rangle \right] \tag{6.1.3}$$

After the second split, the packets undergo the transformation

$$|\delta\rangle \to \frac{1}{\sqrt{2}}\left[|\delta\rangle + i|2+\delta\rangle\right] \tag{6.1.4}$$

$$|2+\delta\rangle \to \frac{1}{\sqrt{2}}\left[|2+\delta\rangle + i|\delta\rangle\right] \tag{6.1.5}$$

Combining the above equations together, the final product is

$$|\psi\rangle = \frac{1}{2}\left[\left(1 - e^{-i\phi_r}e^{-i\frac{2k\delta\tau}{m}}\right)|\delta\rangle + i\left(1 + e^{-i\phi_r}e^{-i\frac{2k\delta\tau}{m}}\right)|2+\delta\rangle\right] \tag{6.1.6}$$

The probability finding the atoms with final momentum δ is

$$P_0 = \frac{1}{4}\left|1 - e^{-i\phi_r}e^{-i\frac{2k\delta\tau}{m}}\right|^2 = \cos^2\left(\frac{\phi_r}{2} + \frac{k\delta\tau}{m}\right) \tag{6.1.7}$$

Similarly, the probability finding the atoms in $|2+\delta\rangle$ is

$$P_1 = \frac{1}{4}\left|1 + e^{-i\phi_r}e^{-i\frac{2k\delta\tau}{m}}\right|^2 = \sin^2\left(\frac{\phi_r}{2} + \frac{k\delta\tau}{m}\right) \tag{6.1.8}$$

Since $\phi_r = 4\omega_r\tau$, by measuring the period of the P_i vs. τ, we can estimate the value of

ω_r. However, as (6.1.7) and (6.1.8) show, the interference period will also depend on δ.

To implement the interferometer, we used a Bragg wavelength of 780.152 nm and

an intensity parameter of $\beta = 2\omega_r$. Here β was most accurately determined from the

measured $\frac{\pi}{2}-$ pulse duration of $\tau_{split} = 65\mu s$. For each run, between the split pulses

we vary the time τ from
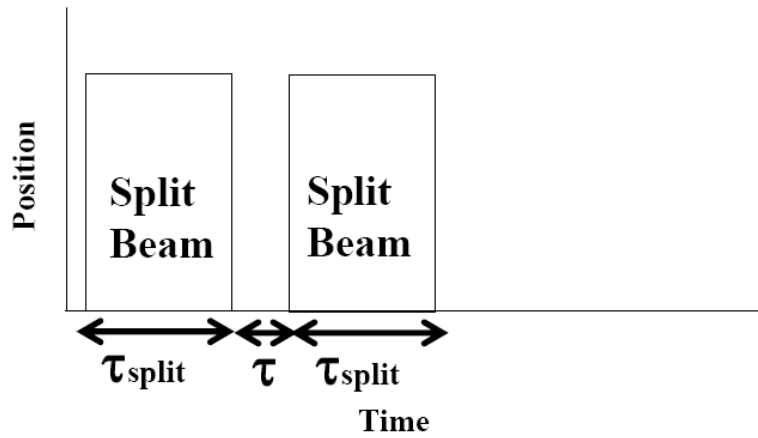
Figure 6.2. Detailed time sequence for Ramsey interferometer. $\tau_{split} = 65\mu s$ while τ varies from 15 μs to 75 μs in 15 μs increments for each run.

15 μs to 75 μs in 15 μs increments. A short diagram of the time sequence is shown in

Fig. 6.2. After the completion of the second split, an absorption image is taken following

a 11ms time-of-flight. We record the population density of the atoms at rest and atoms

moving away by Gaussian fitting the images.

Fig. 6.3 shows the relative number of atoms left in the $|\delta\rangle$ state, and we see that the population oscillates as a function of τ. From equation (6.1.8) we know that the oscillation frequency should be close to $4\omega_r$ which is $67\,\mu s$. Our interference is fitted and shows the period as $67\pm6\mu s$ which matches expectations. As we increase the time between the pulses, the visibility drops significantly as shown in Fig. 6.4. The visibility is measured by fitting the data to a sinusoid,

$$S = A\sin\left(\frac{2\pi\tau}{T} + \phi\right) + y_0 \tag{6.1.9}$$

where $S = \dfrac{N_0}{N}$ and A, T, ϕ and y_0 are fit parameters. The visibility is then,

$$V = \frac{S_{max} - S_{min}}{S_{max} + S_{min}} = \frac{A}{y_0}. \tag{6.1.10}$$

We measured τ up to 3 ms and see that the visibility starts decline around 1 ms. Our best visibility is when τ was $15\,\mu s$ which yielded the visibility of 80%. The figure also shows the underlying contrast, which is defined as $C = \dfrac{S_{max} - S_{min}}{S_{max} + S_{min}}$ with signal values taken directly from the data rather then from the sinusoidal fit. This is therefore a measure of the signal spread. If the noise is entirely due to phase noise $\delta\phi$, then C represents the visibility that would be obtained if the phase noise were eliminated. As can be seen in Fig. 6.4, the visibility declines more quickly than the contrast.
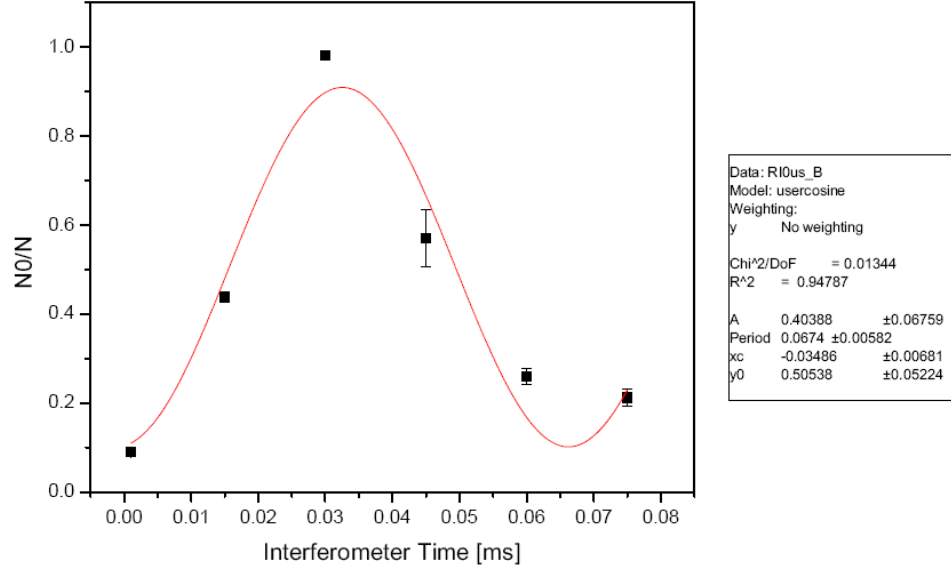
Figure 6.3.   Result of Ramsey Interferometer. From this result we get recoil velocity of 67.4 μs with visibility of 80%. Error bar represents the stand deviation. Not all data points have standard deviation as only one measurement was made for that point.
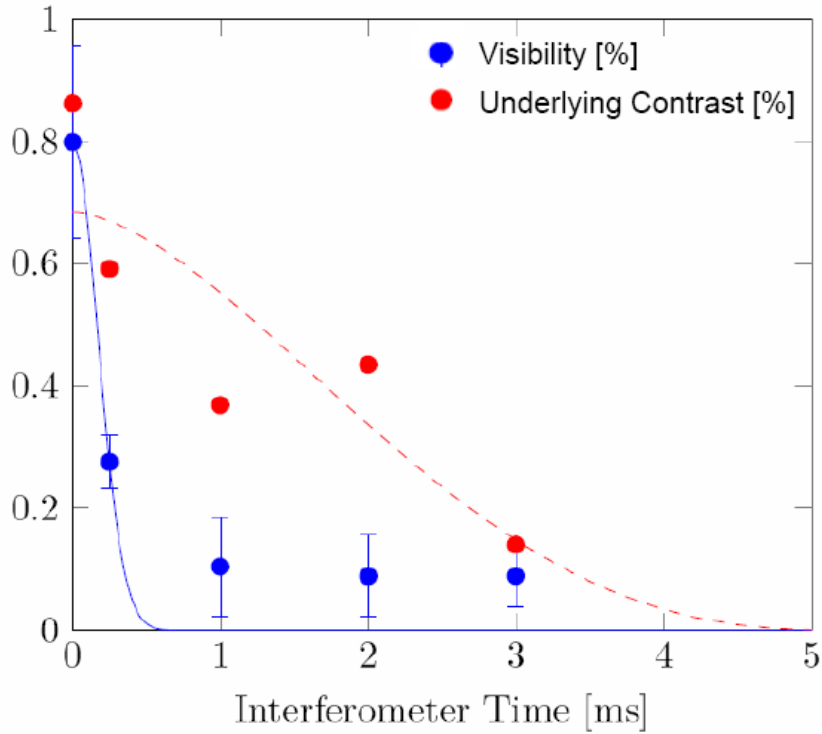

Figure 6.4.   Plot of decreasing visibility (blue) with increased wait times τ . Plot of underlying contrast (red). Two fits are for visibility with and without the initial velocity.

In Fig. 6.4 we see a plot of visibility (blue dots) as a function of total interferometer time. We see the visibility decreases as time increases. This is expected, because the packets are moving further apart, and as they stop overlapping, the interference goes away. Since we know how big the packets are (50 um) and how fast they are moving (12 mm/s), we can theoretically calculate that effect, with the result shown here (red curve). Visibility is fitted with

$$V(t) = Ae^{-(Bt)^2} \tag{6.1.11}$$

where $A = 0.822 \pm 0.099$ and $B = 3.97 \pm 0.70$. As shown in the figure, it does not agree very well. We are instead seeing the effects of noise. We tracked this down and determined it to be noise in the initial velocity of the condensate. Ideally the condensate should start at rest, but in the process of loading the cube trap, we can inadvertently excite its motion. If the condensate initially has velocity δv, then that changes the kinetic energies and the phase evolution of the interferometer packets. The result for the phase is (6.1.7 and 6.1.8). Hence if δv fluctuates, ϕ will fluctuate. From looking at the atoms in the trap, we estimated fluctuation amplitude δv about 10%. If we use that fluctuation and calculate the average visibility given as

$$C(x,y,z,t) = \int_{-\infty}^{\infty} A\sqrt{1 - \left(\frac{x-vt}{L}\right)^2 - \left(\frac{y}{L}\right)^2 - \left(\frac{z}{L\sqrt{\frac{7}{26}}}\right)^2}\, dxdydz \tag{6.1.12}$$

where $A = 0.6266$ and $L = 0.026\ mm$, we get the curve (blue), which agrees pretty well with the data. We can in fact still see the packet separating effect. When the interference

109

is noisy, we can define the interferometer contrast using the magnitude of the fluctuations. If we plot that contrast, we see that it agrees well with what we expect from the packets separating. So we are confident that we understand pretty well the effects of initial velocity.

6.1.1 Initial Velocity

The motion of the atom wave packet in the trap must be addressed if we want to split the packet by transferring the momentum from photon to atom. Our paradigm of asymmetric splitting is based on the fact that we do the pulsed beam operation on the atom packet at rest $p = 0\hbar k$ and transfer to $p = +2\hbar k$ state. However, there is no guarantee that before the split pulse is applied the atoms will be at a complete rest. If there is some initial motion of the atoms before the splitting, then the pulsed beams may not have the proper resonance to transfer all atoms to the higher state. Since the momentum transfer is not perfect to all atoms, we will have an inefficient splitting. For example in extreme cases where atoms have higher initial velocity, the laser beam will not be resonant at all, hence the laser beams will not transfer momentum to atoms as intended. However, for small oscillations, effect will be an inefficient splitting, and small portion of the populations may even get transition to a higher order states i.e. $p = \pm 4\hbar k$, $p = \pm 6\hbar k$, etc..

On debugging our issues of reliability, we check to make sure that the atoms are actually stable and do not have a significant initial velocity. We take an absorption image soon after the atoms are transferred from the TOP trap to the cube trap. Varying the wait time after the transfer and successively taking images, we do find that there is actually a

significant initial velocity present as shown in Fig 6.8. We find the maximum velocity to be $v_{max} = 1.49 \, mm \cdot s^{-1}$. This is about 10% of the atom's velocity. We are certain that this maybe the main culprit contributing to our interferometer uncertainty results. However, we find a work around by adjusting the start time of the interferometer to be at the turning point of the motion where $v_{min} = 0$.
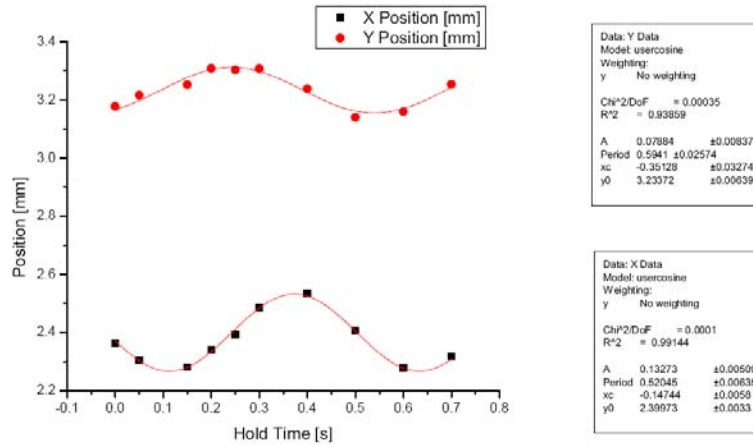
Figure 6.8. We verify that atoms have initial velocity when transferring from strong quadrupole trap to weak spherical trap. Max velocity is ~1.5 mm/s

6.2 Ramsey-Borde Type 1

For the Ramsey-Borde type 1 (RB1) interferometer, we require the full split-reflect-recombine operations. The RB1 uses a triangular path in time by the atom packets, eventually meeting back at the original position when recombined as shown in Fig. 6.5.
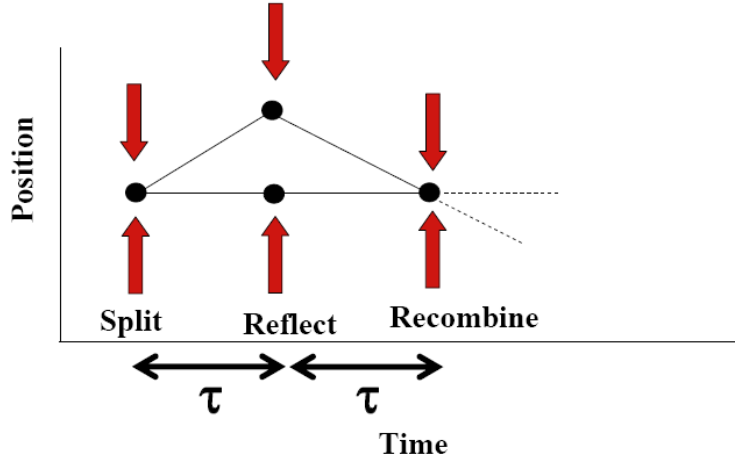
Figure 6.5. Ramsey-Borde type 1 interferometer configuration. After asymmetric split, one atom packet remains at rest while the other gains momentum $+2\hbar k$. At τ time later, a reflect pulse is applied, only reflecting the moving atom wave packet. Again at second τ time later, recombination pulse is applied, showing interference as a result.

To accurately understand the RB1 interferometer, the velocity condition follows that of Ramsey hence after the first asymmetric split, the wavefunction becomes

$$|\psi\rangle \to \frac{1}{\sqrt{2}}\left[|\delta\rangle + i|2+\delta\rangle\right] \tag{6.2.1}$$

where $|2+\delta\rangle$ describes a packet with momentum $(2+\delta)\hbar k$. After free evolution time τ, the atoms in the both states develop phases

$$= \frac{e^{-i\frac{\delta^2\tau}{2m\hbar}}}{\sqrt{2}}\left[|\delta\rangle + ie^{-i\frac{p^2\tau}{2m\hbar}}e^{-i\frac{2p\delta\tau}{2m\hbar}}|2+\delta\rangle\right] \tag{6.2.2}$$

where $p = 2\hbar k$. If we substitute $\omega_r = \frac{\hbar^2 k^2}{2m\hbar}$ and set $\phi_r = 4\omega_r\tau$, and also drop the overall phase, the equation is simplified as

$$\frac{1}{\sqrt{2}}\left[|\delta\rangle + ie^{-i\phi_r}e^{-i\frac{2k\delta\tau}{m}}|2+\delta\rangle\right] \tag{6.2.3}$$

After reflection, the packets undergo the transformation

112

$$|\delta\rangle \rightarrow |\delta\rangle \tag{6.2.4}$$

$$|2+\delta\rangle \rightarrow |-2+\delta\rangle \tag{6.2.5}$$

Hence (6.1.3) becomes,

$$\frac{1}{\sqrt{2}}\left[|\delta\rangle + ie^{-i\phi_r}e^{-i\frac{2k\delta\tau}{m}}|-2+\delta\rangle\right] \tag{6.2.6}$$

After free evolution time τ, the atoms in the both states develop phases

$$\frac{1}{\sqrt{2}}\left[e^{-i\frac{\delta^2\tau}{2m\hbar}}|\delta\rangle + ie^{-i\phi_r}e^{-i\frac{2k\delta\tau}{m}}e^{-i\phi_r}e^{+i\frac{2k\delta\tau}{m}}e^{-i\frac{\delta^2\tau}{2m\hbar}}|-2+\delta\rangle\right] \tag{6.2.7}$$

Again dropping the overall phase term and simplifying

$$\frac{1}{\sqrt{2}}\left[|\delta\rangle + ie^{-i2\phi_r}|-2+\delta\rangle\right] \tag{6.2.8}$$

After recombine, the packets undergo the transformation

$$|\delta\rangle \rightarrow |\delta\rangle + i|-2+\delta\rangle \tag{6.2.9}$$

$$|-2+\delta\rangle \rightarrow |-2+\delta\rangle + i|\delta\rangle \tag{6.2.10}$$

$$\frac{1}{\sqrt{2}}\left[|\delta\rangle + i|-2+\delta\rangle + ie^{-i2\phi_r}\left(|-2+\delta\rangle + i|\delta\rangle\right)\right] \tag{6.2.11}$$

Combining the above equations together, the final product is

$$|\psi\rangle = \frac{1}{2}\left[\left(1-e^{-i2\phi_r}\right)|\delta\rangle + i\left(1+e^{-i2\phi_r}\right)|-2+\delta\rangle\right] \tag{6.2.12}$$

The probability finding the atoms with final momentum δ is

$$P_0 = \frac{1}{4}\left|1-e^{-i2\phi_r}\right|^2 = \cos^2\left(\phi_r\right) \tag{6.2.13}$$

Similarly, the probability finding the atoms in $|-2+\delta\rangle$ is

$$P_1 = \frac{1}{4}\left|1 + e^{-i2\phi_r}\right|^2 = \sin^2(\phi_r) \qquad (6.2.14)$$

The Ramsey-Borde interferometer is a scalable interferometer which uses all three operations of atom manipulation: asymmetric split, reflect, and recombine. Similar to that of the Ramsey interferometer, it posses the capability to measure the recoil frequency, and furthermore builds a foundation for the next generation gravity measurement. Recall that we are in a weak horizontal trap, not a vertical trap against the gravity. The same manipulations, however, will be needed in the future 'vertical' experiment.

As in the Ramsey interferometer, we use a Bragg beam detuning of 780.152 nm, and an intensity parameter $\beta = 2\omega_r$. Our $\frac{\pi}{2}-$ pulse time is $\tau_{split} = 65\mu s$. After a successful split, we wait time τ before applying a reflect pulse with $\tau_{reflect} = 360\mu s$. This drives the transition $|+2\rangle \rightarrow |-2\rangle$, reflecting back the moving atoms. The stationary atoms are not affected by the reflect pulse. We wait another time τ before administrating the final recombination pulse with a beam frequency change from $\omega_0 + \Delta$ to $\omega_0 - \Delta$. The time sequence is shown in Fig. 6.6. A time-of-flight absorption imaging is taken after 100ms to measure the number of atoms in both packets.
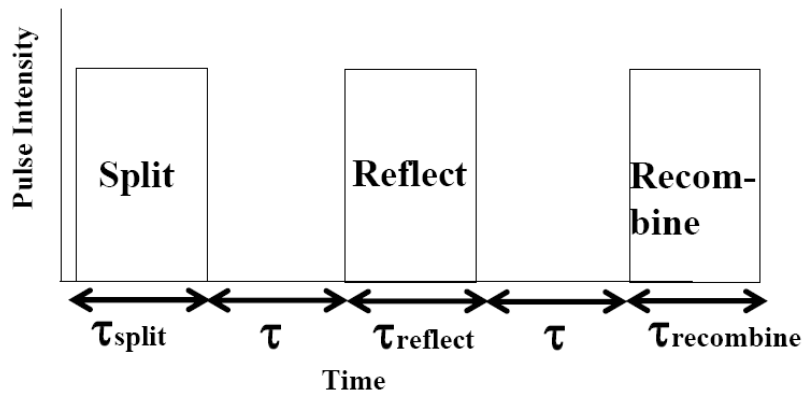
Figure 6.6. Detailed time sequence for Ramsey-Borde type 1 interferometer. $\tau_{split} = 65\,\mu s$ and $\tau_{reflect} = 360\,\mu s$ while τ varies from $10\,\mu s$ to $140\,\mu s$ in $10\,\mu s$ increments for each run.

There were several issues that had to be resolved before successfully running the experiment. Originally, the reflect pulse was to switch the frequency of the laser such that laser beam with $\omega_0 + \Delta$ was suppose to change to ω_0 and the intensity parameter β was suppose to change from $2\omega_r$ to $4.5\omega_r$ allowing the reflect of the moving wave packet. However, to do this, we have to attenuate the beam power to administer the pulse. Turns out, this technique proved to be very difficult as when the laser power is decreased, the phase signal at the Hammamatsu PD also decreased and there was not enough voltage in the error signal for the electronics to lock the phase. Hence the laser locking was not working. Even though the atoms were reflected, we often saw multiple packets and subsequent recombination pulse did not work.

For this reason, to make a successful RB1 interferometer, we needed to keep $\beta_{reflect} \approx \beta_{split}$. We acieve this by switching one of the inputs to the multiplexer from DC to a 15 kHz sinusoidal wave, allowing the second beam to have both $\omega_0 + \Delta$ and $\omega_0 - \Delta$ components. The first beam remains at ω_0. We numerically simulate the reflection process as in section 2.4, this time with an extra term in the potential in equation (2.1.7) with $\left[\cos(2kz + \Delta t + \phi) + \cos(2kz - \Delta t + \phi)\right]$. To find the reflect time, we optimized the pulse duration to give the highest fidelity for a given β using the gradient descent algorithm. We determined β from the asymmetric $\pi-$ pulse time and then set the reflect time accordingly. The results suggestd an optimum reflect pulse time of

$\tau_{reflect} = 360 \mu s$. More details about this reflect pulse can be found in Rob Horne's thesis [24].

Building upon this finding, we perform the timed pulse operation as shown in Fig. 6.6. We obtain the interferometer result shown in Fig. 6.7.

We obtain a period of $68 \pm 6 \mu s$ with visibility of $\sim 45\%$. The period is consistent with the known recoil frequency value $67 \mu s$. Along with a lower visibility, we see a wider spread of the data points and the chi square fit is not as good, giving $R^2 = 0.5$. Here 1 denotes a perfect fit.

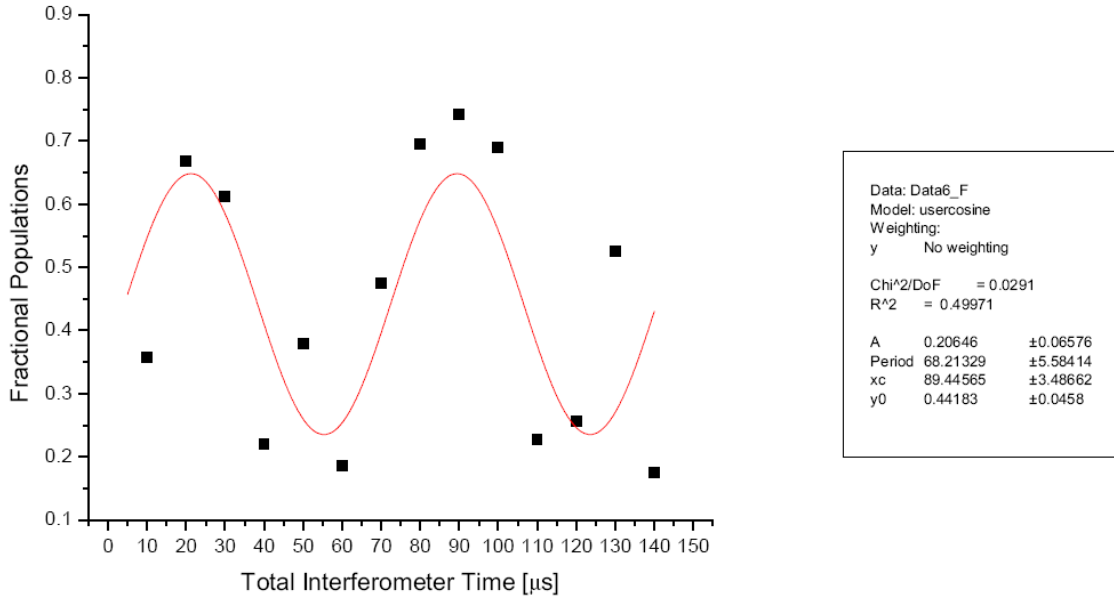Figure 6.7. Result of Ramsey-Borde type 1 interferometer. From this result we get recoil velocity of $68.2 \mu s$ with visibility of 45%. We were not able to make multiple data points so no error bars on data points. Data at 061914

We attribute this relatively poor performance to the velocity sensitivity of the reflection pulse. As noted previously, the initial velocity fluctuation are significant, up to

10% of the recoil velocity. As we will investigate this effect in next section, such an initial velocity of atoms may give rise to an inefficient splitting, reflect, and recombine.

Nevertheless, we demonstrate that we can manipulate the atoms using the asymmetric split, reflect, and recombine. To acquire more stable interferometer result, the initial velocity will need to be resolved for future work.

6.3 Ramsey-Borde Type 2

The RB of the second type resembles the double triangular path as shown in Fig. 6.9. In this configuration, the moving atom packet makes a full cycle back to the original position at the end, recombining with the packet at rest. The RB2 interferometer reflects twice and waits time 2τ before the second reflect pulse is applied. The total recoil it endures is $4\phi_r$ compared to ϕ_r in Ramsey and $2\phi_r$ in RB1. The motivation behind the RB 2 is that the moving packet will experience both sides of the trap. Although the trap is fairly flat, the atoms do not generally start out at the trap center. They therefore experience a potential gradient, which can contribute to the measured interferometer phase. By using a symmetric trajectory like RB2, the effect of the potential gradient cancels out.
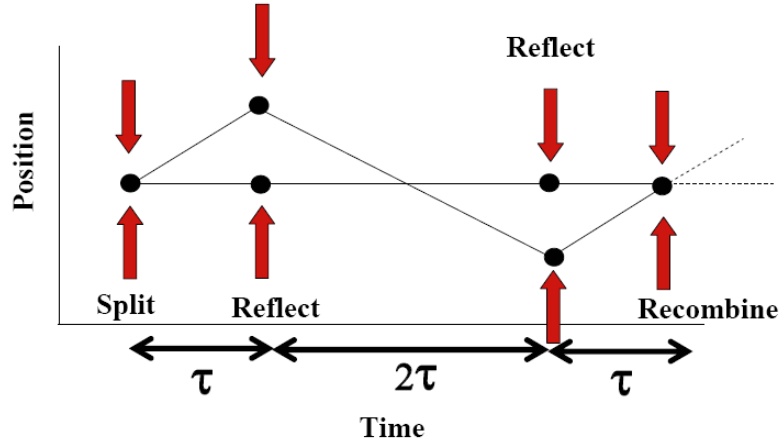
Figure 6.9. Ramsey-Borde type 2 interferometer configuration. After asymmetric split, one atom packet remains at rest while the other gains momentum $+2\hbar k$. At τ time later, a reflect pulse is applied, only reflecting the moving atom wave packet. Wait 2τ time later, second reflect pulse is applied. At τ time later, recombination pulse is applied, showing interference as a result.

The calculation for RB2 follows that of RB1. The only difference is that the cycle is repeated twice. The probability finding atoms at rest is

$$P_0 = \cos^2\left(2\phi_r\right) \tag{6.3.1}$$

The RB type 2 interferometer follows the same initial split and reflect pulse as that of RB type 1. In this interferometer, we wait 2τ before applying the second reflect

Figure 6.10. Detailed time sequence for Ramsey-Borde type 2 interferometer. For 1-2-1 experiment $\tau_{split} = 65\mu s$ and $\tau_{reflect} = 360\mu s$ while τ varies from $1\,ms$ to $1.01\,\mu s$

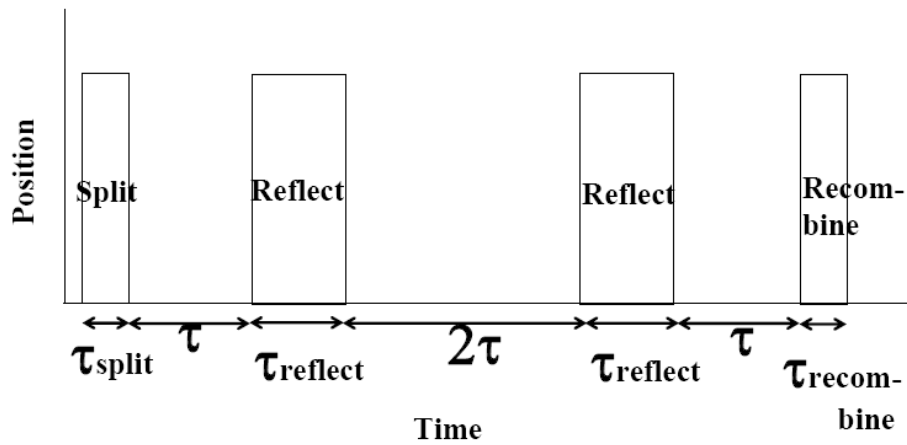in 5 μs increments for each run. For 0-0-0 experiment, τ varies from 10 μs to 25 μs in 5 μs increments for each run.

pulse also with $\tau_{reflect} = 360 \mu s$. The final recombination pulse is applied after waiting τ.

Time sequence diagram is shown in Fig. 6.10. For the RB 2 we ran two experiments with two sets of times: for $\tau = 1$ ms and its variations, we call this a 1-2-1 interferometer, first number representing the time we wait between the asymmetric split pulse and the first reflect pulse, the second number is time we wait between the subsequent reflect pulses, and the last number representing time between the last reflect and recombine pulses, respectively in ms. Hence the number 1-2-1 represents split, then wait 1 ms, reflect, wait 2 ms, reflect, wait 1 ms, and recombine. For $\tau = 10 \mu s$ and its variations, we call this the 0-0-0 interferometer as the atoms really do not move that much spatially. Again, we use absorption imaging to record the population density.

We first discuss the 0-0-0 interferometer. The pulse parameters were the same as in the RB1 experiment. After each measurement, we vary the initial time $\tau = 10$ μs by increasing it by 4 μs. We show the results in Fig. 6.11 giving a period of 69 ± 2 μs with visibility of 49%.

Figure 6.11. Result of Ramsey-Borde type 2, 0-0-0 interferometer. From this result we get recoil velocity of 69 μs with visibility of 49%.

The 1-2-1 interferometer is shown in Fig. 6.12.

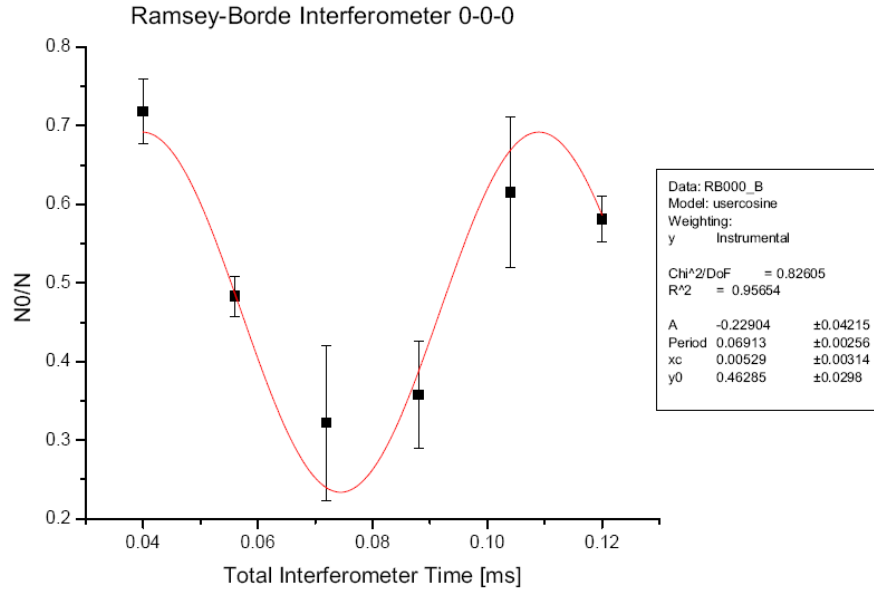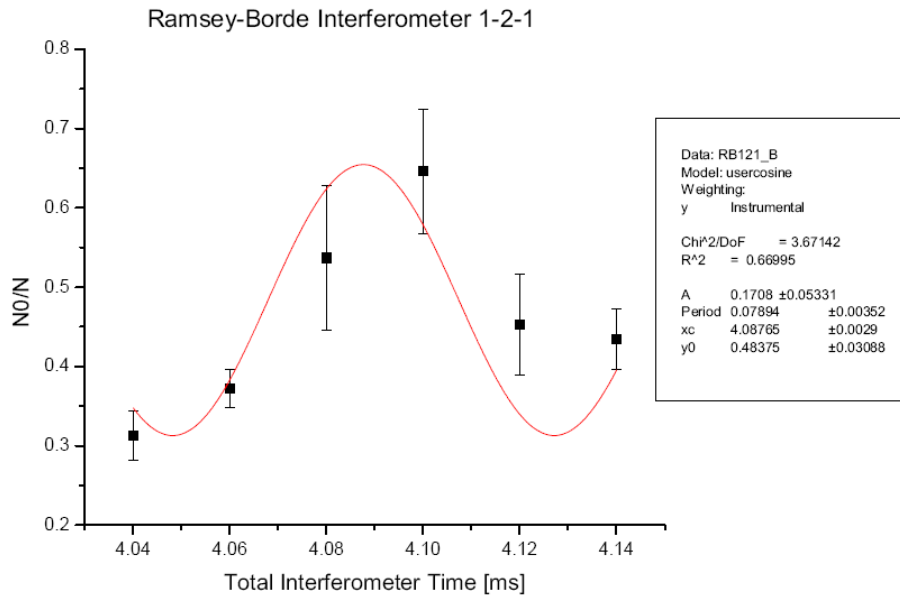Figure 6.10. Result of Ramsey-Borde type 2, 1-2-1 interferometer. From this result we get recoil velocity of 78.9 μs with visibility of 35%. Error bars show standard deviation. 062614

We here obtain a period of $79 \pm 4 \ \mu s$ which is not too far from the recoil of $67 \ \mu s$. We get visibility of about 35% which is less than all of our Ramsey-Borde type interferometers. It is clear that our interferometer need some minor tuning to get a better visibility.

To check the interferometer phase in a more sensitive way, we can compare the results of the 0-0-0 and 1-2-1 experiments. These differ only in the amount of free evolution time, and the phase during the free evolution should evolve as ϕ_r. To observe this, we can compare the times at which an interference maximum occurs in each data set. The 0-0-0 fit gives $t_{max0} = 5 \pm 3 \ \mu s$, while the 1-2-1 interferometer gives $t_{max1} = 4.088 \pm 0.003 \ ms$. If the experiment is working correctly, the time difference $\Delta t = 4.082 \pm 0.006 \ ms$ should correspond to an integer number of periods of ϕ_r. Using the known value of the recoil frequency $\omega_r = 2\pi \times 15 \text{kHz}$, the period of ϕ_r is $T = 66.3 \mu s$. We therefore see $\Delta t / T = 61 \pm 0.006$. The fact that this value is an integer, within error, is validation of the phase stability of the apparatus.

Overall, we performed several interferometer experiments to validate our asymmetric splitting capabilities. First, the Rabi experiment in chapter 5 clearly showed the cyclic oscillation of population density. We followed up with the Ramsey interferometer, and then the Ramsey-Borde to complete the interferometry. We varied, τ, time between pulses, and made repeated measurement on the recoil velocity.

6.4 Recoil Velocity Measurement Summary

We summarize the result obtained for recoil frequency measurement via

interference period in Table 6.1.

Table 6.1

Type	Measured Period(μs)	Theoretical Value	Visibility
Ramsey	67 ± 5	67	80%
Ramsey-Borde 1	68 ± 6	67	45%
0-0-0 Ramsey-Borde2	69 ± 2	67	49%
1-2-1 Ramsey-Borde2	79 ± 4	67	35%

From the result, it is obvious that a longer separation and more pulsed operations reduce the visibility and accuracy. This by all means, is not discouraging, but gives hope that we can make this better once we have a complete control of few little minor issues such as the initial velocity. We did not just make one interferometer, but made 4 different types of measurements. Measuring the recoil frequency measurement was apex of this thesis.

6.5 Summary

We were able to demonstrate an atom interferometer using asymmetric operations and our phase stabilization scheme. We obtained values for the ^{87}Rb recoil frequency that are in good agreement with expectations. We identified the main limiting factor in the performance as the residual velocity fluctuations in the initial atoms, coupled with the velocity sensitivity of the reflection pulse.

One issue that still needs to be resolved is repeatability. Throughout the work, it was challenging to keep the intensity parameter β stable. We identified and fixed several sources of drift, but further study will likely be required.

Overall, we surpassed the goal of this thesis, which was targeting the development of instrumentation for asymmetric splitting. Within short time of accomplishing the

asymmetric splitting, we accelerated our progress and implemented a functional interferometer. We acknowledge the significant contributions to this effort of fellow student Robert Horne.

7.0

Conclusion

Wrapping Up and New Start

We have successfully split BEC wave packets asymmetrically. We were able to split, reflect and recombine successfully. The phase locking circuit and AOM drive circuits worked well and stabilizes phase throughout the interferometer duration times. We obtain interference of the Ramsey with greater than 80% visibility and Ramsey-Borde with visibility of ~50%. We were able to measure, with some accuracy, the recoil

frequency. One can note immediately that asymmetric splitting is required for a recoil frequency measurement.

This initial study is a proof of concept for future work on measuring gravity with much higher sensitivity in small volume than previously done. Already underway is set up for that next generation experiment. We have identified initial velocity fluctuations as an important obstacle.

For gravity measurement, the beam needs to be oriented vertically. Previous experiments (Hughes 2008) have shown that after multiple pulses, the atoms can drift out of the beam center, reducing the fidelity and visibility. We can address these issues with bigger and higher power beams to do optical manipulations.

Measuring gravity will be the a challenge. We have taken the first step in developing the phase locking circuit and the optical pulse manipulations. Hence we have already begun a set of experiment that can be fruitful in future.

7.1 Future Asymmetric Interferometer Concept

So far, we have not addressed the details of the gravity measurement. Recall that our goal was to devise a method to achieve a longer arm separation distance to measure gravity. This is more evident by examining the proposed vertical interferometer where the wave-packets follow the path shown in Fig. 7.1. There are some similarities with optical manipulation as done by Hughes et. al. 2008 such as reflecting the wave-packets using pulsed lasers but we need asymmetric splitting in order to achieve the trajectories proposed in Fig. 7.1.

In Fig. 7.1, the wave-packets are manipulated using the following method: initially at A ($d = 0$), a wavepacket at rest is split using the transition $|0\rangle \rightarrow \frac{1}{\sqrt{2}}(|0\rangle + i|+2\rangle)$. This means the top packet gains momentum $2\hbar k$ while the bottom packet falls from rest. The top packet comes to rest at B after time $t = \frac{2\hbar k}{mg}$, reaching height $d = +h_A = +\frac{1}{2}g\left(\frac{2\hbar k}{gm}\right)^2$. At the same time, the bottom wavepacket falls distance $d = -h_A = -\frac{1}{2}g\left(\frac{2\hbar k}{gm}\right)^2$ and reaches velocity $v_A = -\frac{2\hbar k}{m}$. At this point there
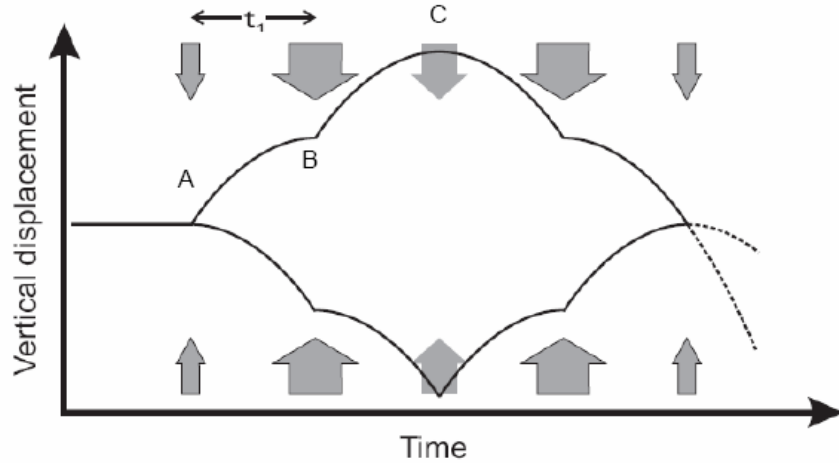
Figure 7.1 Proposed atom packet trajectory to measure gravity with better precision through large distance separation and larger separation times. This configuration would require asymmetric splitting and reflection to make it work.

are two series of operations as shown in Fig. 7.2. First, a reflect pulse of $4\hbar k$ is applied, temporarily sending the bottom wave-packet to $v_{B1} = +\frac{2\hbar k}{m}$ (Fig. 7.2 (a)) while the top packet stays $v = 0$. It is immediately followed by another pulse driving the transition

$|0\rangle \leftrightarrow |+2\rangle$, thus changing the bottom packet momentum to $v = 0$ (Fig. 7.2 (b)) while giving the top wave-packet a $2\hbar k$ kick. So after two sets of pulses, the bottom wavepackets falls again from rest while the top wavepacket is sent upward against gravity and the cycle repeats. At the mid point labeled C in Fig. 7.1 where the top packet reaches distance $d = +h_c = +h_A + \frac{1}{2}g\left(\frac{2\hbar k}{mg}\right)^2$ with $v = 0$, the bottom packet reaches

$d = -h_c = -h_A - \frac{1}{2}g\left(\frac{2\hbar k}{mg}\right)^2$ with velocity, $v_C = -\frac{2\hbar k}{m}$. Both packets are subjected to a

$4\hbar k$ reflection pulse, causing the bottom packet to reverse direction while the top wave-packet continues at $v = 0$.
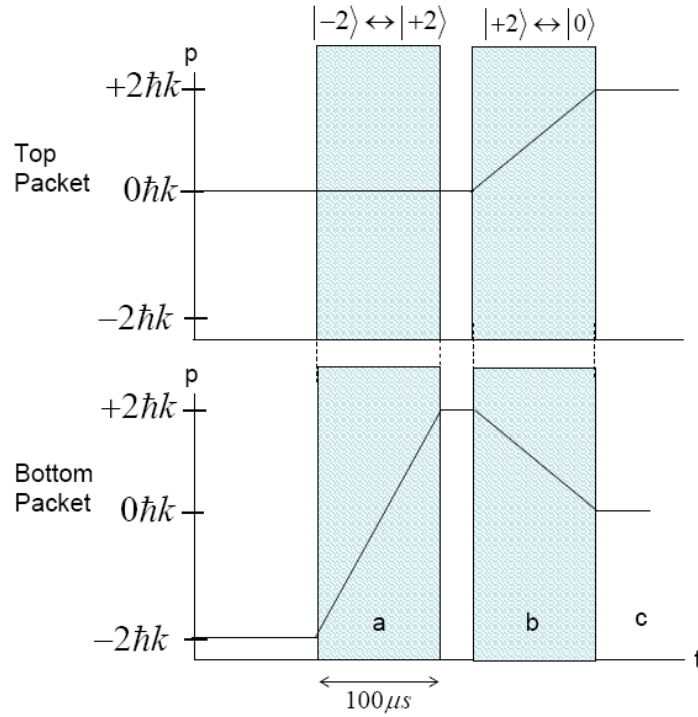

Figure 7.2 Double pulse method to reflect atoms at the bottom. First reflect pulse of $4\hbar k$ followed by another pulsed to change the bottom packet momentum to while giving the top wave-packet a $2\hbar k$ kick. Results the bottom wave-packets falls again from rest while the top wave-packet is sent upward against gravity.

127

As the packets come back together, the applied operations are just the opposite of that described for point B. At the end, the recombination pulse is applied driving the transition $\frac{1}{\sqrt{2}}(|0\rangle + |-2\rangle) \to |0\rangle$. This recombines the packets and provides the output interference signal. More precisely, the recombination causes transitions

$$|0\rangle \to \frac{1}{\sqrt{2}}(|0\rangle + i|-2\rangle) \tag{7.1.1}$$

$$|-2\rangle \to \frac{1}{\sqrt{2}}(|-2\rangle + i|0\rangle) \tag{7.1.2}$$

So, the wave-function evolves as,

$$|\psi\rangle = \frac{1}{\sqrt{2}}(|0\rangle + ie^{-i\phi}|-2\rangle) \to |\varphi\rangle = \frac{1}{2}\left[(1 + ie^{-i\phi})|0\rangle + (i + e^{-i\phi})|-2\rangle\right] \tag{7.1.3}$$

The probability of finding atoms at $|0\rangle$ state is derived to be $\cos^2\left(\frac{\phi}{2} + \frac{\pi}{2}\right)$, whereas the probability at finding atoms at $|-2\rangle$ state is derived to be $\sin^2\left(\frac{\phi}{2} + \frac{\pi}{2}\right)$. The two separate wave-packets experience different heights manifests in a gravitational phase,

$$\phi = \frac{1}{\hbar}\int S(t)dt \tag{7.1.4}$$

where $S(t)$ is action function. Carrying on the integral for the first journey to point B, the top packet gravitational phase is developed as,

$$\phi = \frac{1}{\hbar}\int(\frac{1}{2}mv^2 - mgz)dt \tag{7.1.5}$$

Through classical mechanics of falling body, we find velocity and displacement,

$$v = -gt + v_0 \tag{7.1.6}$$

and

$$z = -\frac{1}{2} g t^2 + \frac{2\hbar k}{m} t. \qquad (7.1.7)$$

With initial velocity of wave packet trusted upward with $v_0 = \frac{2\hbar k}{m}$ with time of flight

$t = \tau = \frac{2\hbar k}{gm}$ reaching height $+h_A$, we find phase for the upper wave packet to be,

$$\phi_{top} = -\frac{1}{\hbar} \frac{4}{3} \frac{\hbar^3 k^3}{gm^2} \qquad (7.1.8)$$

where as for the bottom wave packet reaching height $-h_A$,

$$\phi_{bottom} = \frac{1}{\hbar} \frac{1}{3} \frac{\hbar^3 k^3}{gm^2} \qquad (7.1.9)$$

For our case, at end of each pulse cycle, the atom are separated $14 \mu m$ in $t = 1.19 ms$. Theoretically, a bounces of 1000 pulses will yield about 1 cm separation in 1 second. With a phase measurement accuracy of 0.01 radians, one can achieve sensitivity of about $\delta g = 7 \times 10^{-10} \, \text{m/s}^2$ which is a significant improvement over previous experiments and surpasses the sensitivity of a mechanical sensor. Here this sensitivity can be reached with no significant drop distance, and a vertical space requirement of only the 1 cm needed to accommodate the packet separation. However we also have limitations. As we pulse atoms with laser beams, we will start to lose atoms during every pulse. If we end up losing 1% of the atoms every pulse, by time 1000th pulse is applied, we would not have any atoms left for measurement. Hence, we need to build our instrument that can efficiently manipulate BEC wave packets as well as stable laser beam that does not introduce additional noise unto the phase of the beam.

The splitting and recombining operation described above was not used in earlier experiments done by Hughes et. al 2008, as it requires the asymmetric transitions

$\left| 0 \right\rangle \leftrightarrow \left| 2\hbar k \right\rangle$ and $\left| 0 \right\rangle \leftrightarrow \left| -2\hbar k \right\rangle$. This is the main motivation for this thesis and now see

how asymmetric splitting can accurately measure gravity.

8.0   References

1) Optics and interferometry with atoms and molecules. A. D. Cronin, J. Schmiedmayer, D. Prichard. Review of Modern Physics, V 81, July-September 2009 (1051-1129).
2) Ludwig Zehnder, Z,. Instrumentenkunde 11 (1891)275
3) Ludwig Mach, Z,. Instrumentenkunde 12 (1892)89
4) Integrated mach-Zender interferometer for Bose-Einstein condensate. Berrada, Frank, Schumm, Schaff, and Schmiedmayer. Nature Communications 4, 2077, June 2013
5) Atom interferometer-based gravity gradiometer measurement. Jeffrey B. Fixler. Ph.D. Thesis. Stanford 2003
6) Observation of Gravitationally Induced Quantum Interference. R. Colella, A.W. Overhauser, S.A. Werner. Phys. Rev. Lett. Vol. 34, Num. 23, (1975)
7) Measurement of the Gravitational Acceleration of an Atom with a Light-Pulse Atom Interferometer. M. Kavevich and S. Chu. Appl. Phys. B 54 321-332 (1992)
8) Precision atom interferometry. A. Peters, K. Chung, B. Young, J Hensley, and S. Chu. Phil. Trans, R. Soc. Lond. A 355, 2223-2233 (1997)
9) Measurement of gravitational acceleration by dropping atoms. A. Peters, K. Chung, and S. Chu. Nature Vol 400 849-852 (1999)
10) High-Precision gravity measurements using atom interferometry. A Peters, K. Chung, and S. Chu. Metrologia, 38, 25-61 (2001)
11) Index of Refraction of Various Gases for Sodium Matter Wave. J. Schmiedmayer, M. Chapman, C. Ekstrom, T. Hammond, S. Wehinger, and D. Prichard. Phys. Rev. Lett. Vol 74, Num. 7 (1995)
12) Sensitive absolute-gravity gradiometry using atom interferometry. J. M.McGuirk, G.T. Foster, J.B. Fixler, M.J. Snadden, and M.A. Kasevich. Phys. Rev. A. 65 033608 (2002)
13) Atom interferometer as a selective sensor of rotation or gravity. B. Dubetsky and M. Kasevich. Phys. Rev. A 74 023615 (2006)
14) Bose-Einstein condensate interferometer with macroscopic arm separation. O. Garcia, B. Deissler, K.J. Hughes, J.M. Reeves and C.A. Sackett, Phys. Rev. A 74, 031601(R) (2006)
15) High-fidelity manipulation of a Bose-Einstein condensate using an optical standing wave   K. J. Hughes, B. Deissler, J. H. T. Burke and C. A. Sackett, Phys. Rev. A 76, 035601 (2007)
16) Reif
17) Patheria
18) Kittel
19) Kozuma et. al (1999)
20) Contrast Interferometry using Bose-Einstein Condensates to Measure h/m and α. S. Gupta, K. Dieckmann, Z. Hadzibabic, D. E. Prichard. PRL 89, Number 14, (2002)
21) Horikoshi and Nakagawa 2007
22) PID Controllers: Theory, Design, and Tuning. Hagglund. ISBN 978-1556175169. 1995.
23) http://cdn.intechopen.com/pdfs-wm/29826.pdf

24) Rob Horne Thesis. (In progress)

25) Ofir Garcia. Ph.D. Dissertation. University of Virginia. 2007

26) Ben Diessler. Ph.D. Dissertation. University of Virginia. 2008

27) Jeramy Hughes. Ph.D. Dissertation. University of Virginia. 2008

28) John Burke. Ph.D. Dissertation. University of Virginia. 20010

29) Rob Horne. Ph.D. Dissertation (in progress). University of Virginia. 2014

30) Confinement effects in a guided-wave atom interferometer with millimeter- scale arm separation. J. H. T. Burke, B. Deissler, K. J. Hughes and C. A. Sackett, Phys. Rev. A 78, 023619 (2008)

31) Scalable Bose-Einstein-condensate Sagnac interferometer in a linear trap. J. H. T. Burke and C. A. Sackett, Phys. Rev. A 80, 061603(R) (2009)

32) Suspension of Atoms Using Optical Pulses, and Application to Gravimetry. K. J. Hughes, J. H. T. Burke, and C. A. Sackett, Phys. Rev. Lett. 102, 150403 (2009)

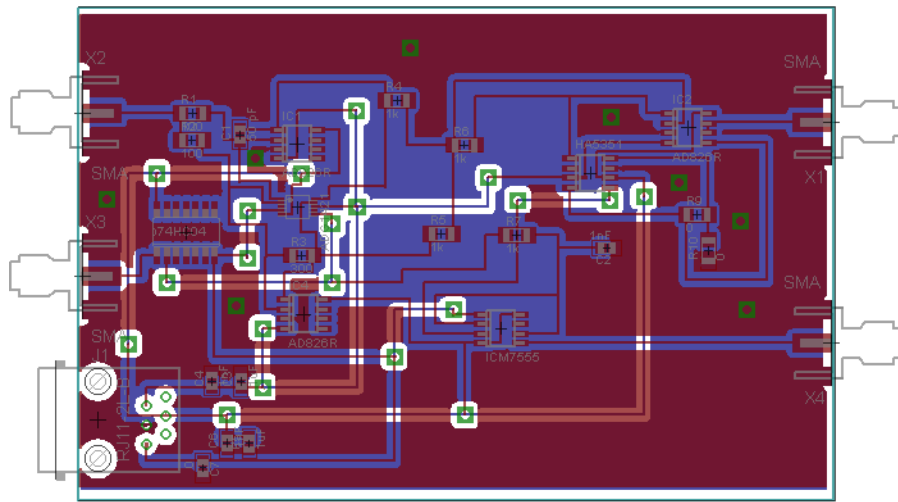## Appendix A - Sample and Hold PCB Design

Figure A. Board layout for S/H. We use Eagle CAD software for two layer design.

Appendix B – Initial Delayer

We delay the laser pulse on signal with the initial delayer shown in Fig. C. This delayer is used to make sure that any delay in shutter and AOM operation do not contribute to locking of phase. Delay is set for 1.8 μs but range of delay is adjustable.
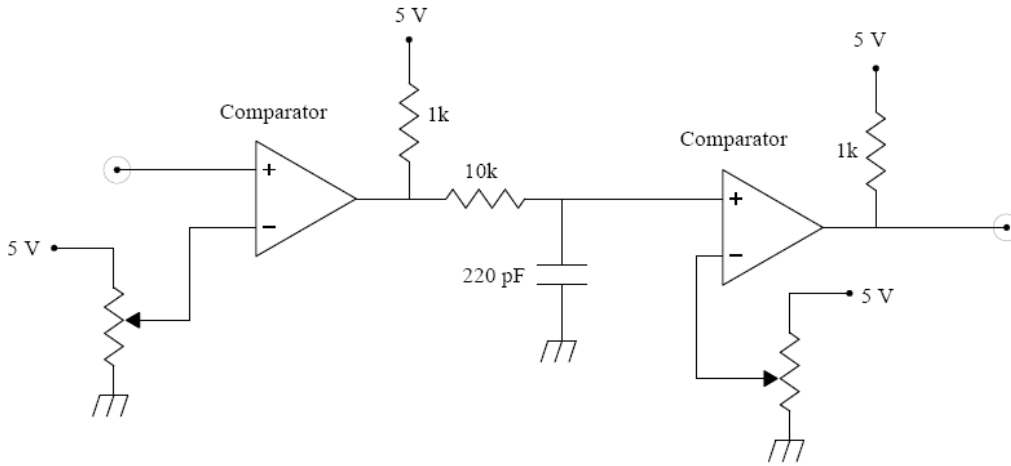

Figure B.   Schematic diagram for delayer which delays turning on the locking signal. This makes sure that laser beam is present in AOMs before S/H lock turns on.

Appendix C – Multiplexer

Fig. C shows detailed circuit diagram for multiplexer. Input 1 is 15 kHz from function generator which is phase shifted 90 degrees and enters the MUX in switched pins (S1 and S2). Input 2 and 3 is optional for future experiments. For this experiment, we connect the 15 kHz to input 2. Output from MUX is pin labeled "D" and its output is controlled using control bits A0 and A1. Outputs are fed into IQ modulator.
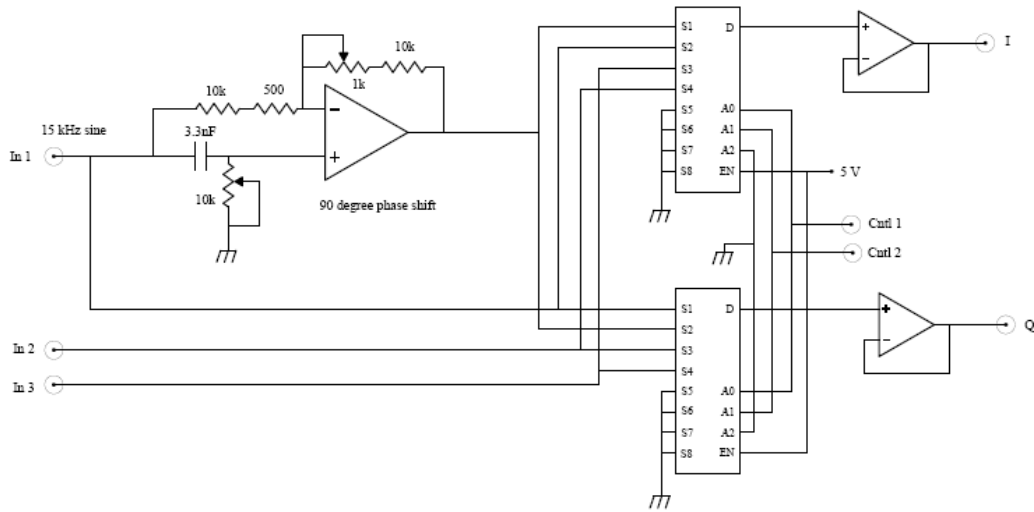
Fig. C. Shows detailed circuit diagram for multiplexer.

Appendix D –program: Bragg_deriv_delta

This program runs the asymmetric Rabi model as described in Chapter 2 equation (2.2.9)

```
function dydt = bragg_deriv_Delta(t,y)
global b d;
dydt = zeros(13,1);
Delta = 4 ;
n = 1;
nn = n-7;
dydt(n) = -1i*((2*nn+d)^2*y(n) + b/2*y(n+1)*exp(-1i*Delta*t));
for n=[2:12]
nn = n-7;
dydt(n)=-1i*((2*nn+d)^2*y(n)+b/2*(y(n-1)*exp(1i*Delta*t)+y(n+1)*exp(-
1i*Delta*t)));
end
n = 13;
nn = n-7;
dydt(n) = -1i*((2*nn+d)^2*y(n) + b/2*y(n-1)*exp(1i*Delta*t));
```

Appendix E –program: b_max

This program is used to calculate max split values for intensity parameter β and give

graph shown in Fig. 2.2

```matlab
global b d
b1=.2;
b2=4;
b_step=0.1;
totalrun=(b2-b1)/b_step+1;
barray=b1+[0:totalrun-1]*b_step;
resultarr=zeros(4,totalrun);
cnt=1;
for cnt=1:totalrun
b = barray(cnt); %our b is between .2 to 4
y = zeros(1,13); %setting up array of 1(column) by 13(row) matrix
yi = y;
yi(7) = 1; % 7th row is 1.  initial state with population in n = 0;
             % d = dp/hk for initial momentum dp
d = 0.0; % for initial state with momentum 0 hk
t1 = 30.0; %max=3*2*Pi/b
n = 6 ; %this is c_-1
[t,y] = ode45(@bragg_deriv_Delta,[0 t1],yi); %calling ODE function that
                                                returns Cn
y1 = y(:,n); %This is the result for C_-1 (n=6)
f_minus1=zeros(length(y1),1); %setting up result matrix that equals
                                dimension of array
for i1=1:length(y1); %Since we cannot simply do "abs^2" need to
                        transpose array.
    temp_y1=y1(i1); %temperorary to store the array
    f_minus1(i1) = abs(temp_y1)^2; %getting the magnitude
end
pks = findpeaks(f_minus1);
first_peak_value=pks(1);
location_1stPeak_f_minus1 = find(f_minus1 == first_peak_value);
t_1stmax=t(location_1stPeak_f_minus1);
resultarr(:,cnt)=[b,1/b,t_1stmax,first_peak_value];
cnt
end
figure(1)
plot(resultarr(2,:),resultarr(4,:));
title('Splittting efficiency')
xlabel('1/b')
ylabel('Max 1st Split values')
figure(2)
plot(resultarr(3,:),resultarr(1,:));
title('b versus t')
xlabel('t')
ylabel('b')
figure(3)
plot(resultarr(3,:),resultarr(4,:));
title('efficiency versus t')
xlabel('t')
ylabel('efficiency')
```

Appendix F –program: dphi

This program is used to calculate the phase accuracy as shown in Fig. 3.2.4 as exlained in Chapter 3.4.

```matlab
dir='C:\Users\Eun\Desktop\PhD\MATLAB\2014_2_21\CSV\';        %
files location
for i = 1:100;
    str_i = int2str(i);
    filename=[dir 'scope_' str_i '.csv'];
    M = csvread(filename);
    if i == 1
        M_1= M(:,1);
        M_3_Array=M(:,3);
    else
        M_3_Array=[M_3_Array M(:,3)];
    end
end
avg=mean(M_3_Array,2);
figure(1)
plot(M_1,avg);
  x_low=419   %min(find(M_1  >  -7.8e-4));  need  to  look
manually for min.
  x_high=1752 %max(find(M_1 < 0.0)); need to look manually
for max
  timevec=M_1(x_low:x_high);
  x=timevec;
  y=avg(x_low:x_high);
  [estimated_params]=sine_fit(x,y,[NaN   NaN   NaN   NaN],[0
0.085 0 15000],1)
   FittingPara=[estimated_params];
   offset=FittingPara(1,1) %offset
   A=FittingPara(1,2) %amplitude
   phaseshift=FittingPara(1,3) %phaseshift
   frequency=FittingPara(1,4) %frequency

   new_M_3_Array=M_3_Array-offset;
   check_m3=new_M_3_Array-M_3_Array;
   newavg=avg-offset;
   checkavg=newavg-avg;
   fit_y=    FittingPara(1,1)    +    FittingPara(1,2)    *
sin( FittingPara(1,3) +
     2*pi*FittingPara(1,4)*timevec );
   for i = 1:100;
       if i == 1
           delta_f=M_3_Array(x_low:x_high,i)-fit_y;
       else
           delta_f=[delta_f  M_3_Array(x_low:x_high,i)-fit_y];
```

```matlab
        end
    end
    x_low;
    x_high;
newavg=y-offset;

    df_over_A=(delta_f)/abs(A);
    dt=5.0000e-007;
    period=x_high-x_low;
    t1=-phaseshift/frequency;
    c0s=cos(2*3.14159*frequency*(x-t1));
    for i=1:100
        U_0=0.5*(c0s(1)*df_over_A(1,1));
        U_f=0.5*(c0s(length(c0s)))*df_over_A(length(c0s),1);
        U(i)=dot(c0s,df_over_A(:,i))-U_0-U_f;
    end
        phi=2/period*(U)*1;
    for i = 1:100;
         phi2=1/100*sum(phi(i)^2);
    end
    delta_phi=sqrt(phi2)

    figure(2)
    plot(newavg)
    hold on
    plot(A*c0s)
```

Appendix G – Rubidium Data

<div align="center">

Fundamental Constants

Name	Symbol	Value
Speed of light	c	2.99792458×10^8 m/s
Standard gravity	g	9.80665 m/s^2
Permeability of vacuum	μ_0	$4\pi \times 10^{-7}$ N/A^2
Permittivity of vacuum	ϵ_0	$8.854187817 \times 10^{-12}$ F/m
Planck's constant	h	$6.62606876 \times 10^{-34}$ Js
	$\hbar = h/2\pi$	$1.054571596 \times 10^{-34}$ Js
Elementary charge	e	$1.602176462 \times 10^{-19}$ C
Bohr magneton	μ_B	$9.27400899 \times 10^{-24}$ J/T
Atomic mass unit	u	$1.66053873 \times 10^{-27}$ kg
Electron mass	m_e	$9.10938188 \times 10^{-31}$ kg
Bohr radius	a_0	$0.5291772083 \times 10^{-10}$ m
Boltzmann's constant	k_B	$1.3806503 \times 10^{-23}$ J/K
Atomic mass	m	$86.909\ 180\ 520$ u
		$1.44316060 \times 10^{-25}$ kg
Nuclear spin	I	$3/2$
Scattering length	a	5.77 nm

$5\,^2S_{1/2} \to 5\,^2P_{3/2}$ **Transition properties**

Name	Symbol	Value
Frequency	ω_o	$2\pi \cdot 384.2304844685$ THz
Wavelength (vacuum)	λ	780.241209686 nm
Lifetime	τ	26.24 ns
Natural linewidth	Γ	$2\pi \cdot 6.065$ MHz
Recoil velocity	v_r	5.8845 mm/s
Recoil temperature	T_r	361.96 nK
Doppler temperature	T_D	$146\ \mu$K
Electron spin g-factor	g_S	2.0023193043737
Electron orbital g-factor	g_L	0.99999369
Fine structure	$g_J(5\,^2S_{1/2})$	2.00233113
Landé g-factor	$g_J(5\,^2P_{1/2})$	0.666
	$g_J(5\,^2P_{3/2})$	1.3362
Nuclear g-factor	g_I	-0.0009951414

</div>